# Spatial Dynamics of the Developing Human Heart

Enikő Lázár[1,2#§], Raphaël Mauron[1#], Žaneta Andrusivová[1#], Julia Foyer[1], Mengxiao He[1], Ludvig Larsson[1], Nick Shakari[3], Sergio Marco Salas[3], Christophe Avenel[4], Sanem Sariyar[5], Jan N. Hansen[5,6], Marco Vicari[1], Paulo Czarnewski[1], Emelie Braun[7], Xiaofei Li[8], Olaf Bergmann[2,9,10], Christer Sylvén[11], Emma Lundberg[5,6,12,13], Sten Linnarsson[7], Mats Nilsson[3], Erik Sundström[8], Igor Adameyko[14,15], and Joakim Lundeberg[1§]

[1]Department of Gene Technology, KTH Royal Institute of Technology, Science for Life Laboratory, 17165 Solna, Sweden

[2]Department of Cell and Molecular Biology, Karolinska Institute, 17165 Solna, Sweden

[3]Department of Biochemistry and Biophysics, Stockholm University, Science for Life Laboratory, 17165 Solna, Sweden

[4]Department of Information Technology, Uppsala University, Science for Life Laboratory, 75237 Uppsala, Sweden

[5]School of Engineering Sciences in Chemistry, Biotechnology and Health, KTH Royal Institute of Technology, Science for Life Laboratory, 17165 Solna, Sweden

[6]Department of Bioengineering, Stanford University, Stanford, CA 94305, USA

[7]Division of Molecular Neurobiology, Department of Medical Biochemistry and Biophysics, Karolinska Institute, 17165 Solna, Sweden

[8]Division of Neurodegeneration, Department of Neurobiology, Care Sciences and Society, Karolinska Institute, 17165 Solna, Sweden

[9]Department of Pharmacology and Toxicology, University Medical Center Goettingen, 37075 Goettingen, Germany

[10]Center for Regenerative Therapies Dresden, TU Dresden, 01307 Dresden, Germany

[11]Department of Medicine, Karolinska Institute, 14157 Huddinge, Sweden

[12]Department of Pathology, Stanford University, Stanford, CA 94305, USA

[13]Chan Zuckerberg Biohub, San Francisco, San Francisco, CA 94158, USA

[14]Department of Physiology and Pharmacology, Karolinska Institute, 17165 Solna, Sweden

[15]Department of Neuroimmunology, Medical University of Vienna, 1090 Vienna, Austria

#EL, RM and ŽA contributed equally to this work.

§Correspondence should be addressed to EL (eniko.lazar@scilifelab.se) and JL (joakim.lundeberg@scilifelab.se).

## ABSTRACT

Heart development relies on a topologically defined interplay between a diverse array of cardiac cells. We finely curated spatial and single-cell measurements with subcellular imaging-based transcriptomics validation to explore spatial dynamics during early human cardiogenesis. Analyzing almost 80,000 individual cells and 70,000 spatially barcoded tissue regions between the 5.5$^{th}$ and 14$^{th}$ postconceptional weeks, we identified 31 coarse- and 72 fine-grained cell states and mapped them to highly resolved cardiac cellular niches. We provide novel insight into the development of the cardiac pacemaker-conduction system, heart valves, and atrial septum, and decipher heterogeneity of the hitherto elusive cardiac fibroblast population. Furthermore, we describe the formation of cardiac autonomic innervation and present the first spatial account of chromaffin cells in the fetal human heart. We support independent exploration of our datasets by an open-access, spatially centric interactive viewer. In summary, our study delineates the cellular and molecular landscape of the developing heart's architecture, offering links to genetic causes of heart disease.

## INTRODUCTION

The heart serves as the central organ of the cardiovascular system by generating a pressure gradient that enables blood circulation throughout the body. The sequential activation of two ventricles and two atria is orchestrated by the cardiac pacemaker-conduction system, while the tandem operation of two sets of cardiac valves blocks retrograde blood flow during the cardiac cycle. Heart rate and contraction force are also tightly regulated by the autonomic nervous system, adjusting cardiac output to the momentary needs of the body.

The heart forms its primary structures already within the 1st trimester of prenatal development[1,2]. Cardiogenic mesoderm emerges during the 3rd postconceptional week, which evolves into a linear heart tube by the end of the 5th week. Through extensive spatial rearrangements and differentiation of diverse cell types, the cardiac tube transforms into the multilayered, four-chambered heart by the 8th week, with maturation and growth continuing throughout fetal and postnatal development. Besides early cardiac precursors, other cells of extracardiac origin, including epicardial and neural crest cells, contribute to heart formation. Overall, early cardiogenesis follows a tightly regulated spatiotemporal progression, where disruptions can lead to congenital heart anomalies, highlighting the importance of understanding its governing molecular mechanisms[3,4].

Anatomical changes throughout various stages of cardiogenesis have been studied in several species, including humans[5–10]. Over the past decade, the widespread adoption of single-cell RNA sequencing techniques yielded fresh insight into cardiac development on the cellular and molecular levels, describing transcriptomic profiles of cells within embryonic and fetal hearts, both in animal models[11–21] and humans[22–29]. However, single-cell studies are inherently limited by their inability to retain the spatial context of isolated cells, which plays a pivotal role during morphogenesis. Recent advancements in spatial transcriptomics technologies allowed the detection of RNA expression within tissue sections, capturing previously inaccessible information on molecular arrangements in two dimensions. Combining these two technologies enables a more nuanced understanding of cell identities and interactions, factoring in their transcriptomic signature and their position within the tissue[30,31]. This approach has been successfully employed in a recent study investigating cardiogenesis in chicken[20], the first published spatiotemporal atlas of human heart development[32], and a recent report assessing cellular communities in the fetal human heart[33].

Here we present a deep spatiotemporal map of the developing human heart during the 1st and early 2nd trimester. We analyzed 38 hearts between the 5.5$^{th}$ and 14$^{th}$ postconceptional weeks and assembled an extensive dataset of 69,114 spatially barcoded tissue spots and 76,801 individual cells, complemented by spatial detection of 150 selected transcripts by *in situ* sequencing (ISS). We discerned 23 spatial compartments with distinct transcriptional profiles within the cardiac tissue, uncovering molecular factors of regionality. Furthermore, we identified 11 primary cell types and 72 fine-grained cell states, which we then mapped to corresponding regions in cardiac tissue sections, enabling their highly refined, spatially-aware annotation. This allowed us to characterize distinct components of the cardiac pacemaker-conduction system, investigate their interactions with the emerging autonomic innervation, and describe a novel resident chromaffin cell population within the fetal heart. We also assessed position-related endothelial and mesenchymal cell heterogeneity in the developing cardiac valves and atrial septum and described an array of spatially defined cell states in the mesenchymal cell-fibroblast compartment. By investigating the co-occurrence of different cardiac cell states, we also delineated the architecture of prominent cardiac niches, enabling their targeted analysis. Furthermore, we provide an interactive viewer (https://hdcaheart.serve.scilifelab.se/web/index.html) to facilitate independent exploration of our datasets and analysis results.

Our work substantially broadens our understanding of early cardiogenesis, and presents a novel approach to cell atlasing, by deciphering cell identities and tissue dynamics with focus on the spatial context.

92 **RESULTS**

93 **Spatial Profiling of the Developing Human Heart**

94 First, to create a comprehensive account on spatial molecular patterns during early cardiogenesis, we
95 performed 10x Genomics Visium spatial transcriptomics analysis on 16 hearts collected between the 6$^{th}$
96 and 12$^{th}$ postconceptional weeks, complemented by *in situ* sequencing of 150 selected transcripts. We
97 compiled a dataset of 69,114 tissue spots from 38 heart sections, covering all major structural components
98 of the developing organ (Fig. 1A). For further analysis of molecular determinants of regionality, we
99 selected 17 sections encompassing at least three cardiac chambers, and performed unsupervised clustering
100 of the corresponding 25,208 tissue spots, resulting in 23 spatial clusters (Fig. 1A-B, Suppl. Fig. 1A, Suppl.
101 Table 1). Two clusters aligned with blood remnants in the atria and ventricles (B_A, B_V), and one with
102 myeloid cell transcriptomic signature (MY) appeared scattered across the myocardium, however, the
103 remaining 20 clusters mapped to distinct cardiac regions (Fig. 1C-D, Suppl. Fig. 1A-B).

104 Cardiac spatial clusters were broadly consistent across developmental stages. Still, we observed gradual
105 disappearance of an early outflow tract-related cluster (OFT) and expansion of clusters representing the
106 tunica media (TM) and adventitia (TA) of the developing large arteries (Suppl. Fig. 1C-D). The early OFT
107 cluster's transcriptomic profile substantially overlapped both with the TM and the valve mesenchyme-
108 related VM clusters, likely due to their spatial proximity at early developmental stages. Notably, the VM-
109 enriched gene *PENK*, a neural crest-derived mesenchymal cell marker described in mouse cardiac
110 valves[34], was not detected in the early OFT cluster, indicating a later contribution of this cell type to valve
111 development (Fig. 1D, Suppl. Fig. 1A). Additional clusters represented the epicardial-subepicardial
112 (A_EP, V_EP) and endocardial-subendocardial (EN) layers, small and large coronary vessels (SCV,
113 LCV), and the developing valve endothelium (VE) (Fig. 1B-Dd, Suppl. Fig. 1A-B, E).

114 Our clustering approach delineated major myocardial compartments in a side-specific manner, facilitating
115 the exploration of their transcriptomic differences (Fig. 1E, Suppl. Fig. 2A, E). Besides several common
116 atrial markers, we observed selective enrichment of *PITX2*, *COL2A1*, and *ADAMTS8* in the left (LA), and
117 *ANGPT1*, *BMP10*, and *DKK3* in the right atrial myocardial clusters (RA). The ventricle-associated spots
118 were further divided into compact (LV_C, RV_C) and trabecular clusters (LV_T, RV_T), marked by the
119 relative enrichment of *HEY2* and *MT3*, versus *MB* and *FHL2*, respectively. Furthermore, we detected side-
120 specific enrichment *NREP* in the left, and *CKM* in the right compact layers, and of *LGALS3* and *IRX3* in

121 the left, and *MASP1* and *PPP1R12B* in the right trabecular compartments. The transcription factor IRX3
122 is associated with ventricular conductive phenotype specification[35], while galectin 3 (encoded by
123 *LGALS3*) is established as a marker for adverse cardiac remodeling, primarily affecting the left ventricle[36].
124 A recent study proposed MASP1 as a candidate gene for ventricular conduction disorders[37], and MYPT2
125 (encoded by *PPP1R12B*) is a known regulator of cardiomyocyte contraction force generation[38]. Side-
126 specific enrichment of these genes might potentially contribute to the distinct electromechanical properties
127 of the two ventricles.

128 Furthermore, we found a spatial cluster characterized by high expression of cardiomyocyte stress- and
129 hypoxia response-related genes (*ACTA1*, *NPPB*, *ENO1*, *LDHA, MIF, FAM162A*)[39,40] positioned around
130 the papillary muscles (PM), reflecting mechanical strain on these structures (Fig. 1F, Suppl. Fig. 1A-B,
131 E). Additionally, tissue spots with conduction system cell signatures localized to the ventricular
132 subendocardium (VCS) and the atrial side of the atrioventricular plane (AVP_A), consistent with the
133 position of bundle branches and atrioventricular nodal tissue, respectively (Fig. 1b-c, Suppl. Fig. 1a-b, e).
134 Notably, we also observed a ventricular cluster of ambiguous identity, localized close to the
135 atrioventricular plane (AVP_V), sharing markers with both AVP_A (*CNN1*, *XPO4*) and PM-MB (*ACTA1*,
136 *MYL2*) clusters (Fig. 1B-C, Suppl. Fig. 1A-B, E).

137 We complemented our investigation with a spatially aware, neighborhood-based region identification
138 approach[41], which provided a good agreement with the spatial clusters representing larger myocardial and
139 vessel compartments, but by design, did not distinguish fine or spatially dispersed structural components.
140 At the same time, this analysis recognized a spatial domain corresponding to components of the
141 intracardiac ganglionated plexi (ICGP), not recognized by our original clustering strategy (Extended
142 Figure 1A-E). Additionally, we also performed non-negative matrix factorization (NMF) on the entire
143 Visium dataset to decipher 20 spatial gene modules covarying in our samples, also included in our
144 interactive viewer for independent assessment.

145 In summary, spatial profiling of the developing heart revealed previously unappreciated transcriptomic
146 signatures in the papillary muscles and the atrioventricular region and provided insight into the molecular
147 composition of other cardiac compartments.

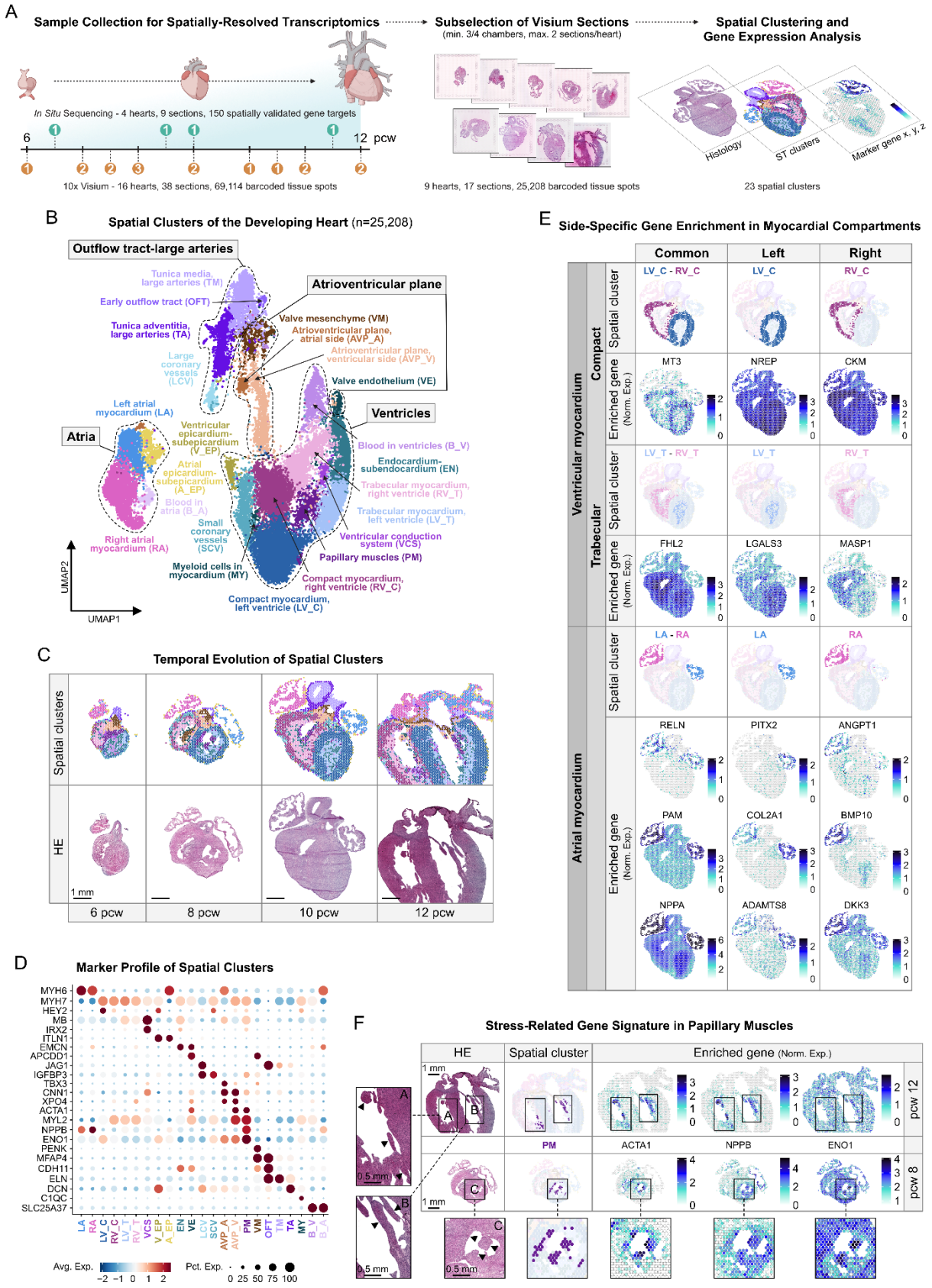
A
Sample Collection for Spatially-Resolved Transcriptomics
Subselection of Visium Sections
(min. 3/4 chambers, max. 2 sections/heart)
Spatial Clustering and Gene Expression Analysis
In Situ Sequencing - 4 hearts, 9 sections, 150 spatially validated gene targets
6
12 pcw
Histology
ST clusters
Marker gene x, y, z
10x Visium - 16 hearts, 38 sections, 69,114 barcoded tissue spots
9 hearts, 17 sections, 25,208 barcoded tissue spots
23 spatial clusters
B
Spatial Clusters of the Developing Heart (n=25,208)
Outflow tract-large arteries
Tunica media, large arteries (TM)
Early outflow tract (OFT)
Tunica adventitia, large arteries (TA)
Large coronary vessels (LCV)
Atrioventricular plane
Valve mesenchyme (VM)
Atrioventricular plane, atrial side (AVP_A)
Atrioventricular plane, ventricular side (AVP_V)
Valve endothelium (VE)
Ventricles
Left atrial myocardium (LA)
Atria
Ventricular epicardium-subepicardium (V_EP)
Atrial epicardium-subepicardium (A_EP)
Blood in atria (B_A)
Small coronary vessels (SCV)
Right atrial myocardium (RA)
Myeloid cells in myocardium (MY)
Blood in ventricles (B_V)
Endocardium-subendocardium (EN)
Trabecular myocardium, right ventricle (RV_T)
Trabecular myocardium, left ventricle (LV_T)
Ventricular conduction system (VCS)
Papillary muscles (PM)
Compact myocardium, right ventricle (RV_C)
Compact myocardium, left ventricle (LV_C)
UMAP2
UMAP1
C
Temporal Evolution of Spatial Clusters
Spatial clusters
HE
1 mm
6 pcw
8 pcw
10 pcw
12 pcw
D
Marker Profile of Spatial Clusters
MYH6
MYH7
HEY2
MB
IRX2
ITLN1
EMCN
APCDD1
JAG1
IGFBP3
TBX3
CNN1
XPO4
ACTA1
MYL2
NPPB
ENO1
PENK
MFAP4
CDH11
ELN
DCN
C1QC
SLC25A37
LA RA LV_C RV_C LV_T RV_T VCS V_EP A_EP EN VE LCV SCV AVP_A AVP_V PM VM OFT TM TA MY B_V B_A
Avg. Exp.
−2 −1 0 1 2
Pct. Exp.
0 25 50 75 100
E
Side-Specific Gene Enrichment in Myocardial Compartments
Common
Left
Right
Ventricular myocardium
Compact
Trabecular
Atrial myocardium
Spatial cluster
Enriched gene (Norm. Exp.)
LV_C - RV_C
LV_C
RV_C
MT3
NREP
CKM
LV_T - RV_T
LV_T
RV_T
FHL2
LGALS3
MASP1
LA - RA
LA
RA
RELN
PITX2
ANGPT1
PAM
COL2A1
BMP10
NPPA
ADAMTS8
DKK3
F
Stress-Related Gene Signature in Papillary Muscles
HE
Spatial cluster
Enriched gene (Norm. Exp.)
pcw 12
pcw 8
PM
ACTA1
NPPB
ENO1
1 mm
0.5 mm

Figure 1

149 **Figure 1. Spatial Profiling of the Developing Human Heart. A.** Overview of spatially-resolved
150 transcriptomic dataset generation, with donor numbers by postconceptional week (pcw) indicated in
151 orange (Visium) and green (*in situ* sequencing) circles. **B.** 23 spatial clusters of the developing heart,
152 corresponding to major cardiac structural components (dashed lines). **C.** Temporal evolution of spatial
153 cluster distribution, presented in 6, 8, 10, and 12 pcw heart sections. Scale bar represents 1mm. **D.** Spatial
154 feature plots displaying side-specific enrichment of selected DEGs of the left (LV_C) and right (RV_C)
155 compact, left (LV_T) and right (RV_T) trabecular, and left (LA) and right (RA) atrial myocardial spatial
156 clusters in a 10 pcw heart section. **E.** Spatial feature plots illustrating stress-related gene signature in
157 papillary muscles (arrowheads in ROI A-C), featuring selected DEGs of the corresponding spatial cluster
158 (PM). Scale bars represent 1 mm in the main, and 0.5 mm in the zoom-in panels. HE–hematoxylin-eosin.

159 **Cellular Landscape of Early Human Cardiogenesis**

160 Next, we explored the cellular composition of the developing cardiac architecture through generating a
161 single-cell RNA sequencing dataset from 15 hearts between the 5.5$^{th}$ and 14$^{th}$ postconceptional weeks,
162 using the 10x Genomics Chromium platform. Unsupervised clustering of the merged 76,801 high-quality
163 cardiac cells defined 31 coarse- and 72 fine-grained cell states with distinct transcriptomic profiles (Suppl.
164 Table 2-6), creating a common framework for cell state identification throughout the analyzed period. We
165 used these clusters to deconvolve the spatial transcriptomics dataset, mapping the predicted spatial
166 distributions of cell states within the developing heart sections, and informing a spatially-aware annotation
167 strategy (Fig. 2A).

168 Among the 31 coarse-grained clusters, expression of canonical cell type markers guided the identification
169 of 11 main cell types, including predominant populations of cardiomyocytes, endothelial cells, and non-
170 mural mesenchymal cells and fibroblast (Fig. 2B-C, Suppl. Table 2). We observed two distinct clusters
171 expressing the smooth muscle cell marker *MYH11*, with one sharing transcriptional characteristics with a
172 separate pericyte population (PC) (Fig. 2C, Suppl. Table 2, Ext. Fig. 2A-F, Ext. Text). Spatial mapping
173 revealed distinct positions of these cell states in the outflow tract and great arteries (OFT_SMC) and large
174 coronary arteries (CA_SMC), respectively (Fig. 2D). Additionally, we annotated epicardial cells (EpC),
175 neuroblasts and neurons (NB-N), and Schwann cell progenitors and glial cells (SCP-GC), based on their
176 marker expression and predicted positions on the epicardial surface, and around the great arteries and
177 atrial walls, respectively (Fig. 2B-D, Suppl. Table 2). We also recognized two smaller populations of

178 myeloid (MyC) and lymphoid cells (LyC), along with two clusters dominated by red blood cell
179 transcriptomic signature, which we excluded from downstream analysis (Fig. 2B-C, Suppl. Table 2, Ext.
180 Fig. 3A-E, Ext. Text). Furthermore, we also observed two clusters (TMSB10$^{high}$_C_1-2) enriched in
181 various thymosin transcripts, previously implicated in coronary vessel development[20,42] (Fig. 2B-C, Suppl.
182 Table 2).

183 The seven coarse-grained cardiomyocyte clusters displayed prominent differences in the expression of
184 maturation, metabolic state, and cell cycle markers (Fig. 2C, E, Suppl. Fig. 2A), based on which we
185 identified mature (Mat_vCM, Mat_aCM) and metabolically active (MetAct_aCM, MetAct_vCM_1-2)
186 atrial and ventricular clusters, besides proliferating cardiomyocytes (Prol_CM). Additionally, we
187 observed a population with lower cardiomyocyte-specific gene expression and a dynamic decrease in
188 proportion (15.18% to 1.63%) over the investigated time frame, outlining immature cardiomyocytes
189 (Immat_CM) (Fig. 2E-F, Suppl. Fig. 2A). Transcriptome-based identities of coarse-grained endothelial
190 cell clusters were in agreement with their predicted localization in the tissue, outlining endocardial
191 (Endoc_EC) and endocardial cushion-related cells (EndocCush_EC), macro- (MacroVasc_EC) and
192 microvascular (MicroVasc_EC) endothelial cells of the coronary vasculature, and lymphatic endothelial
193 cells (LEC) (Fig. 2C, E, Suppl. Fig. 2B). Specific markers for mesenchymal cell- and fibroblast subtypes
194 in the fetal heart are currently lacking, thus positional cues are especially valuable to decipher cell
195 identities. Using a spatially informed annotation strategy, we identified distinct populations of fibroblasts
196 around the outflow tract and developing great arteries (OFT_FB), cardiac valve-related mesenchymal cells
197 (Valve_MC), annulus fibrosus fibroblasts (AnnFibr_FB), interstitial fibroblasts (Int_FB) dispersed across
198 the entire myocardium. We also observed a coarse-grained cluster representing epicardium-derived
199 progenitor cells (EPDC) located in the subepicardial domain, with transcriptomic signatures consistent
200 with an epicardial origin and ongoing epithelial-to-mesenchymal cell transition (EMT) (Fig. 2C, E, Suppl.
201 Fig. 2B, Ext. Fig. 4A-D, Ext. Text). Furthermore, we recognized an additional mesenchymal cell
202 population resembling cardiac pericyte transcriptomic profile (Peric_MC), and a cluster enriched in cell
203 cycle genes (Prol_FB) (Fig. 2C, E, Suppl. Table 2).

204 Our clustering also highlighted an endothelial (PDE4C$^{high}$_EC) and a fibroblast population
205 (PDE4C$^{high}$_FB) with overlapping transcriptomic profiles, enriched in several regulators of primary cilia
206 formation and function (*TTC21A, ARL13B, TULP2*), and the cAMP-signaling-related genes *PDE4C* and
207 *ATF3* (Fig. 2C, E, Suppl. Table 2). Ciliary cAMP signaling is involved in the differentiation of various

208 cell types[43], and a recent study revealed PDE4C regulating ciliary cAMP signaling in murine kidney
209 cells[44]. By performing immunostaining for the broad cilia marker ARL13B, the basal body and
210 centrosome marker PCNT, and PDE4C or ATF3, we observed ciliation, as well as PDE4C and ATF3
211 protein expression across the entire fetal heart (Suppl. Fig. 2C) and found basal bodies as prominent
212 subcellular localization for both ATF3 and PDE4C. Thus, our data indicate a unique ciliated cell
213 population, spread across the fetal heart, where cilium-related cAMP signaling may play an important
214 role.

215 Temporal changes of cell state distributions in our dataset followed the main events of early cardiogenesis,
216 including a shift towards mature cardiomyocyte profiles, pronounced expansion of vascular endothelial
217 and mural cell populations associated with coronary vessel formation, a relative shrinkage of the
218 epicardial, endocardial and cushion-related cellular compartments, and an expansion of the Schwann cell
219 precursor-glial cell population in the developing innervation (Fig. 2F, Suppl. Fig. 2D). Interestingly,
220 TMSB10$^{high}$_C_1 and TMSB10$^{high}$_C_2 clusters, also enriched in *S100A11* and *GNG11*, respectively,
221 showed opposite temporal trends, presumably signaling a shift towards endothelial commitment in these
222 populations (Suppl. Fig. 2D).

223 Differential gene expression analysis across time-resolved subpopulations of spatially annotated, coarse-
224 grained single-cell states revealed relevant temporal transcriptional transitions within the endothelial and
225 non-mural mesenchymal cell-fibroblast populations (Ext. Fig. 5A-C, Ext. Text), and also facilitated the
226 assessment of relevant spatiotemporal patterns, such as presented in the area of the outflow tract and great
227 vessels, and the cardiac valves (Ext. Fig. 6A-C, Ext. Text). Furthermore, enrichment analysis of heart
228 disease-associated gene panels across the identified coarse- and fine-grained cell states broadly validated
229 our cell type annotation, and highlighted the early and widespread expression and complex involvement
230 of the confirmed genetic determinants in various forms of these pathologies (Ext. Fig. 7A-B).

231 Taken together, combined analysis of the single-cell and spatial datasets enabled refined identification of
232 topologically distinct cell states and molecular arrangements, providing novel insight into cellular
233 diversity in the developing heart.

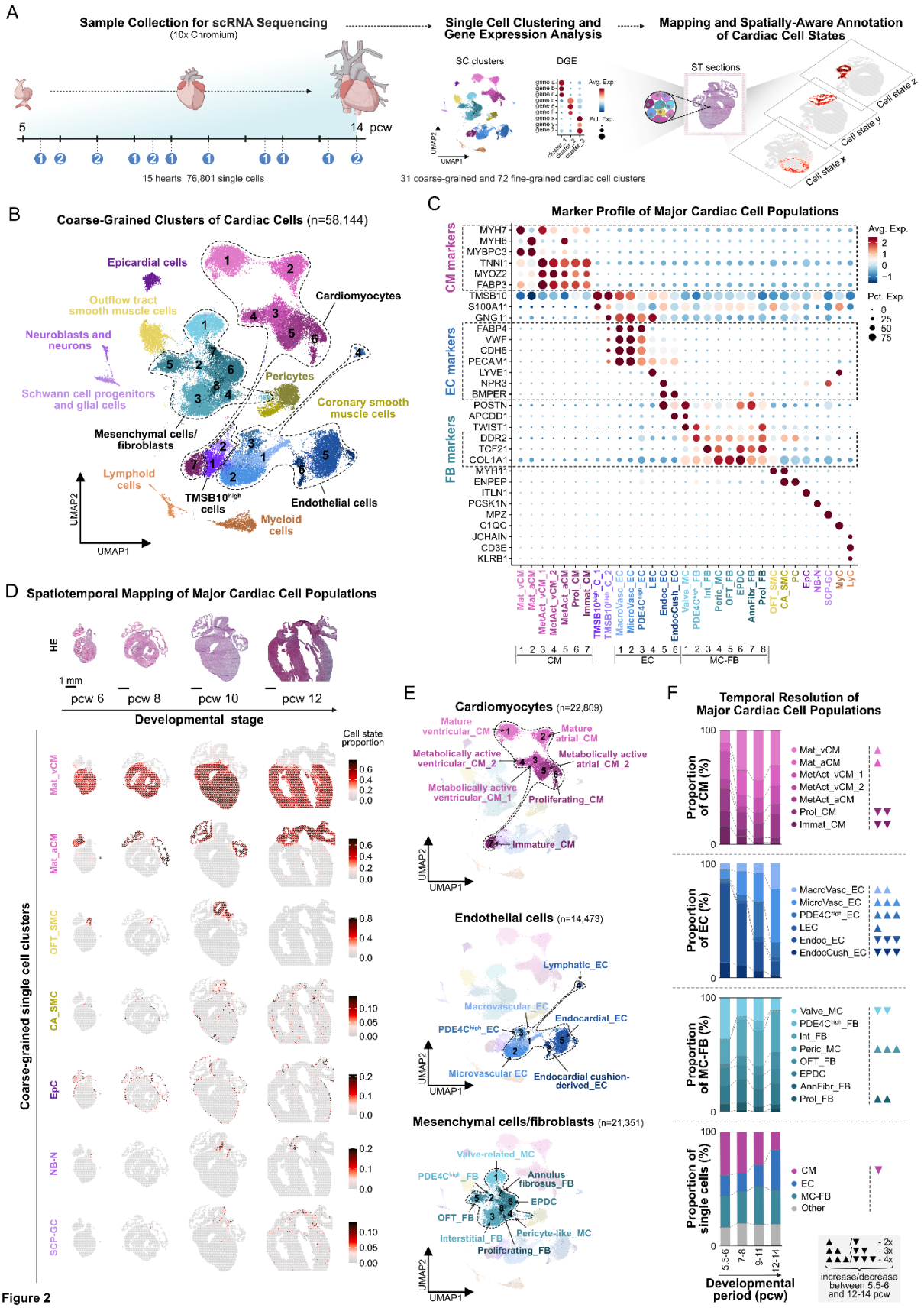
A
Sample Collection for scRNA Sequencing
(10x Chromium)
5
14 pcw
15 hearts, 76,801 single cells
Single Cell Clustering and Gene Expression Analysis
SC clusters
DGE
31 coarse-grained and 72 fine-grained cardiac cell clusters
Mapping and Spatially-Aware Annotation of Cardiac Cell States
ST sections
Cell state x
Cell state y
Cell state z
B
Coarse-Grained Clusters of Cardiac Cells (n=58,144)
Epicardial cells
Outflow tract smooth muscle cells
Neuroblasts and neurons
Schwann cell progenitors and glial cells
Cardiomyocytes
Pericytes
Coronary smooth muscle cells
Mesenchymal cells/ fibroblasts
Lymphoid cells
TMSB10high cells
Endothelial cells
Myeloid cells
UMAP2
UMAP1
C
Marker Profile of Major Cardiac Cell Populations
CM markers
EC markers
FB markers
Avg. Exp.
Pct. Exp.
CM
EC
MC-FB
D
Spatiotemporal Mapping of Major Cardiac Cell Populations
HE
1 mm
pcw 6
pcw 8
pcw 10
pcw 12
Developmental stage
Cell state proportion
Coarse-grained single cell clusters
Mat_vCM
Mat_aCM
OFT_SMC
CA_SMC
EpC
NB-N
SCP-GC
E
Cardiomyocytes (n=22,809)
Mature ventricular_CM
Mature atrial_CM
Metabolically active ventricular_CM_2
Metabolically active atrial_CM_2
Metabolically active ventricular_CM_1
Proliferating_CM
Immature_CM
Endothelial cells (n=14,473)
Lymphatic_EC
Macrovascular_EC
Endocardial_EC
PDE4Chigh_EC
Microvascular EC
Endocardial cushion-derived_EC
Mesenchymal cells/fibroblasts (n=21,351)
Valve-related_MC
PDE4Chigh_FB
Annulus fibrosus_FB
EPDC
OFT_FB
Interstitial_FB
Pericyte-like_MC
Proliferating_FB
F
Temporal Resolution of Major Cardiac Cell Populations
Proportion of CM (%)
Proportion of EC (%)
Proportion of MC-FB (%)
Proportion of single cells (%)
Developmental period (pcw)
increase/decrease between 5.5-6 and 12-14 pcw

Figure 2

235 **Figure 2. Cellular Landscape of Early Human Cardiogenesis. A.** Overview of Chromium single cell
236 dataset generation and spatially-informed annotation of cardiac cell states, with donor numbers by
237 postconceptional week (pcw) shown in blue circles. **B.** UMAP representing 31 coarse-grained cardiac
238 single-cell clusters, corresponding to 11 main cell types. **C.** Enrichment of canonical cell type markers
239 across coarse-grained single-cell clusters. Dashed rectangles highlight consensus markers of
240 cardiomyocytes (CM), endothelial cells (EC) and fibroblasts (FB). **D.** Spatiotemporal mapping of selected
241 coarse-grained clusters in 6, 8, 10, and 12 pcw heart sections. Scale bar represents 1 mm, HE–
242 hematoxylin-eosin. **E.** Spatially-aware annotation of coarse-grained cardiomyocyte, endothelial cell, and
243 mesenchymal cell-fibroblast clusters. **F.** Temporal changes in coarse-grained cluster proportions in the
244 cardiomyocyte, endothelial cell, and fibroblast-mesenchymal cell subsets across four developmental age
245 groups (5.5-6, 7-8, 9-11, and 12-14 pcw). ▲-2x, ▲▲-3x, ▲▲▲-4x increase; ▼-2x, ▼▼-3x, ▼▼▼-
246 4x decrease between the 5.5-6 and 12-14 pcw age groups.

247 **Molecular Map of the Cardiac Pacemaker-Conduction System Development**

248 Contractile cardiomyocytes (CM) are the basic functional units of the myocardium; however, their
249 coordinated activity relies on specialized cardiomyocytes of the cardiac pacemaker-conduction system
250 (CPCS), featuring intrinsic automacy and efficient electrical impulse conduction. During development,
251 these cells gradually acquire distinct electrophysiological properties from the surrounding working
252 myocardium. Molecular characteristics of CPCS cells have been studied in several animal models[45–50] and
253 adult human hearts[51], however, formation of the human CPCS remains uncharted.

254 To bridge this gap, we performed fine-grained clustering of the cardiomyocyte population and identified
255 19 distinct cell states, confirming the recently reported transcriptional diversity of these cells[52]. Besides a
256 range of contractile cardiomyocytes of ventricular (vCM_1-6) and atrial origins (Left_aCM, Right_aCM,
257 and Cond_aCM, representing smooth-walled conduit atrial regions), we also recognized cell states of
258 lower maturation levels (Immat_CM_1-3), and of cell cycle signature (Prol_CM_1-2) (Fig. 3A-B, Suppl.
259 Fig. 3A-B, Suppl. Table 3).

260 Importantly, we observed clusters with robust expression of previously described markers of CPCS
261 components (Fig. 3C, Suppl. Fig. 3A)[45–51]. Spatial mapping traced one such cluster to the upper wall of
262 the right atrium, consistent with the sinoatrial node's position (SAN_CM), while another appeared on the
263 border zone between the atria and ventricles and in the atrial septum, delineating the developing

264 atrioventricular node (AVN_CM). Two ventricular clusters featured markers of the atrioventricular bundle
265 and bundle branches (AVB-BB_CM), and Purkinje fiber cardiomyocytes (PF_CM), and accordingly,
266 were found in the ventricular subendocardium, stretching from the septum towards distal regions of the
267 chambers (Fig. 3C). We observed an additional ventricular cluster with shared transcriptional
268 characteristics and close spatial association to PF_CMs, representing transitional Purkinje fibers (Ts_PF)
269 (Suppl. Fig. 3A, C).

270 CPCS cardiomyocytes displayed substantial overlaps in their transcriptomic profiles. Accordingly,
271 SAN_CMs and AVN_CMs both expressed transcription factors specifically expressed (*SHOX2, TBX18*)
272 or strongly enriched (*PRRX1, ZNF385B*) in pacemaker cardiomyocytes, and axon guidance molecules
273 (*TENM2, TENM3, TENM4, GDF10, SLIT2*), outlining the nodes as essential targets of the developing
274 cardiac innervation (Fig. 3D, Suppl. Fig. 3A). We also found the axon guidance molecule partner
275 *LRRC4C*, previously not discussed in relation to the CPCS, specifically expressed in SAN_CMs (Suppl.
276 Fig. 3A). Highly enriched genes in AVN_CMs reflected the node's position in the atrioventricular plane
277 (*BMP2*, *RSPO3*, *ADAMTS19)*, and neuronal characteristics of these cells (*NRXN3*, *ZNF536*) (Suppl. Fig.
278 3A). Among the ventricular CPCS cell states, PF_CMs showed expression of several characteristic
279 markers (*CSMD1, BRINP3, SGCD, NTN1, SEMA3A*), partly shared with TsPF_CMs (Fig. 3E, Suppl. Fig.
280 3A). While recently described atrioventricular bundle markers *CNTN5* and *CRNDE* displayed broader
281 distribution in our dataset, several genes enriched in AVB-BB_CMs, including *RCAN1* and *HS3ST3A1*,
282 showed characteristic spatial enrichment in the upper edge of the ventricular septum, likely labeling the
283 atrioventricular bundle (Fig. 3E, Suppl. Fig. 3D). Interestingly, the contractile vCM_1 cluster exhibited
284 the highest *CNTN5* expression, beside other differentially expressed genes shared with CPCS (*TBX3,*
285 *HS3ST3A1, BRINP3, TENM3*) and contractile ventricular cardiomyocyte states *(PRDM16, NLGN1,*
286 *SORBS2, MYL2*) (Suppl. Fig. 3A, Suppl. Table 3). The gene enrichment profile (*XPO4*, *MYL2,*
287 *TNFRSF19, SORBS2, ZFP36L1*) and predicted localization of vCM_1 cells also aligned with the elusive
288 AVP_V spatial cluster, supporting a transitional ventricular cardiomyocytes identity of these cells, likely
289 contributing to atrioventricular conductive tissue formation, as previously observed in the mouse heart[47]
290 (Suppl. Fig. 3B, E, Suppl. Table 1, 3).

291 Electrophysiological properties of CPCS components are determined by their ion channel repertoire[53]
292 (Fig. 3F, Suppl. Fig. 3F), which was recently explored in the adult human heart[51]. Similarly to their adult
293 counterparts, developmental SAN_CMs and AVN_CMs featured ion channel profiles consistent with their

294 nodal cell characteristics, including marked enrichment of hyperpolarization-activated cation channels
295 *HCN1* and *HCN4*, and various L- and T-type $Ca^{2+}$ channel genes (*CACNA1C, CACNA1D, CACNA1G,*
296 *CACNA2D2, CACNB2*), responsible for the funny current ($I_f$) and depolarization phase of the nodal action
297 potential ($I_{Ca}$), respectively. As opposed to adult cells, *CACNA1G* showed the highest enrichment in
298 AVN_CMs, while SAN_CMs and ventricular CPCS cell states displayed similar, but somewhat lower
299 expression of this gene. Repolarization in cardiomyocytes is primarily mediated by various potassium
300 currents. Importantly, we found strong enrichment of the G-protein-coupled inwardly rectifying potassium
301 (GIRK) channel subunit *KCNJ3* (but not of *KCNJ5*) in SAN_CMs, but not in PF_CMs, where the
302 expression of this gene was described as a key distinctive feature from contractile ventricular
303 cardiomyocytes in adult hearts[51]. On the other hand, PF_CMs showed high expression of *KCNJ2* and
304 *KCNH7*, contributing to the inwardly rectifying ($I_{K1}$) and fast delayed rectifier potassium currents ($I_{Kr}$),
305 respectively. AVN_CMs also featured strong expression of KCNQ1, previously associated with
306 atrioventricular conduction block[54,55], as well as several ion channels also present in contractile
307 cardiomyocytes (*CACNA1C, KCNQ3, KCNQ5*), reflecting mixed electrophysiological properties of these
308 cells. While *KCND2* (and the functionally related *KCND3*), previously described to be specifically
309 enriched in the adult atrioventricular bundle, showed overall low expression in our dataset, a known
310 interaction partner, *KCNIP4*, was strongly enriched in vCM_1 cells, providing further support to the
311 contribution of this cell state to the developing atrioventricular conductive tissue. Gap junction-encoding
312 gene enrichment showed a similar pattern as in adult hearts, with the low-conductance Cx45 (*GJC1*)
313 marking SAN_CMs and AVN_CMs, and the high-conductance Cx40 (*GJA5*) being enriched in PF_CMs.

314 Beyond several chloride, volume-regulated anion (VRAC), and transient receptor potential (TRP)
315 channels with yet unclear relevance in CPCS function, we also observed enrichment of several ionotropic
316 glutamate receptor genes (*GRID2, GRIK1*) in SAN_CMs, in line with proposed glutamatergic signaling
317 machinery in the adult node[51], as well as of the GABA receptor ion channel *GABRB2* gene in Purkinje
318 fibers, with the latter appearing specific to the developmental phase (Fig. 3F, Suppl. Fig. 3F).

319 To investigate the molecular drivers of pacemaker phenotype specification, we inferred a gene regulatory
320 network of SAN_CMs (Fig. 3G). Key transcription factors (*SHOX2*, *PRDM6*, *THRB*, and *FOXP2*) and
321 ion channel targets (*HCN1*, *CACNA1D*, *KCNT2*, *CACNB2*) exhibited substantial overlap between our
322 results and a recent analysis of adult SAN cardiomyocytes[51]. Among other acknowledged pacemaker
323 regulators enriched in SAN_CMs, such as *TBX18*, *BNC2*, and *TBX3*, the latter showed markedly higher

expression in AVN_CM, AVB-BB_CM and vCM_1. TBX3 is known to suppress the atrial contractile gene program, thus its broader expression in CPCS components aligns with their progressive fate restriction, previously described in mouse[56,57]. Notably, the SAN_CM regulatory network also included transcription factors *BHLHE41* and *RORA*, recognized regulators of the mammalian circadian clock, which has been proposed to underlie time-of-day variation in arrhythmia susceptibility[58,59].

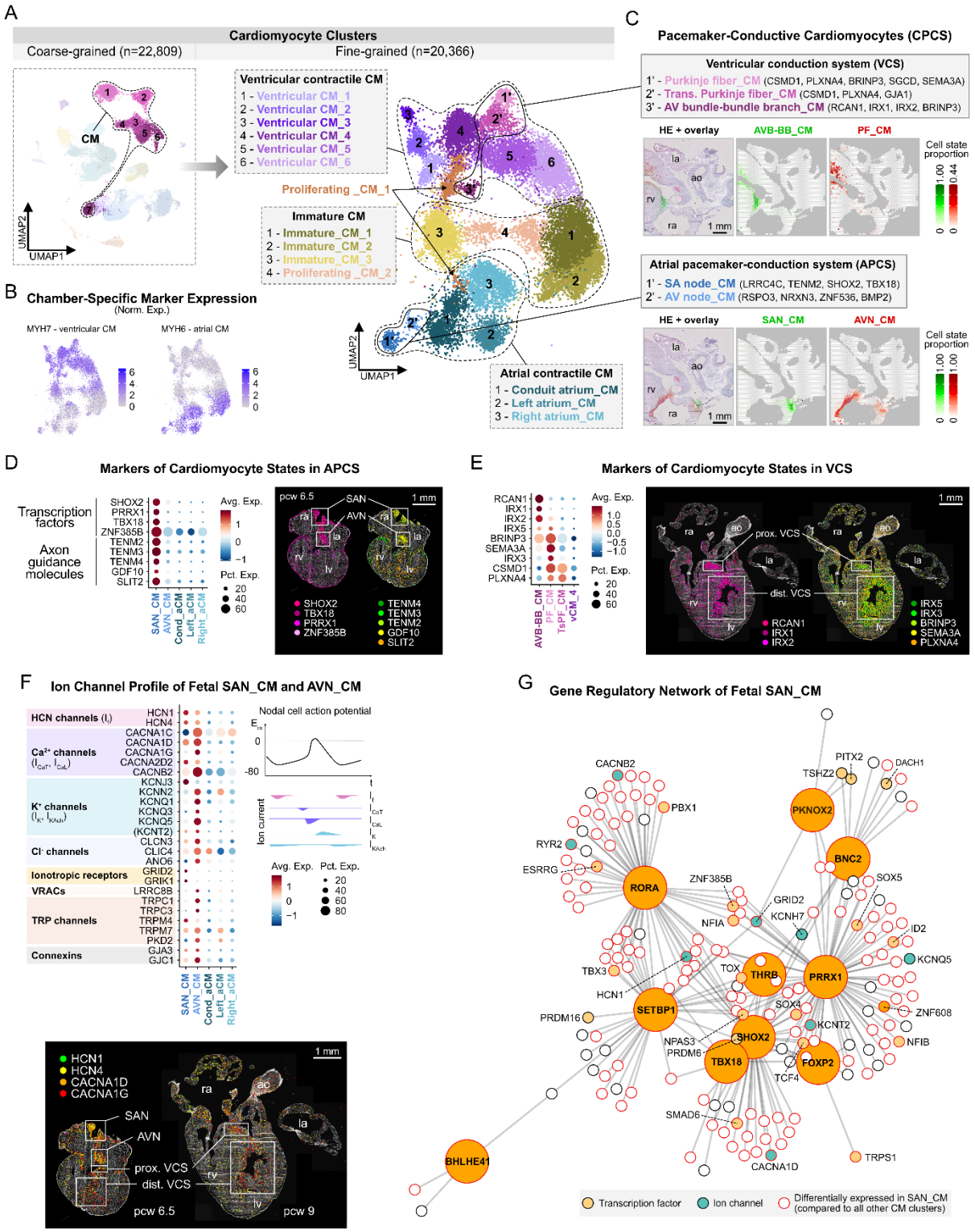
A
Cardiomyocyte Clusters
Coarse-grained (n=22,809)
Fine-grained (n=20,366)
CM
UMAP2
UMAP1
Ventricular contractile CM
1 - Ventricular CM_1
2 - Ventricular CM_2
3 - Ventricular CM_3
4 - Ventricular CM_4
5 - Ventricular CM_5
6 - Ventricular CM_6
Proliferating _CM_1
Immature CM
1 - Immature_CM_1
2 - Immature_CM_2
3 - Immature_CM_3
4 - Proliferating _CM_2
Atrial contractile CM
1 - Conduit atrium_CM
2 - Left atrium_CM
3 - Right atrium_CM
B
Chamber-Specific Marker Expression
(Norm. Exp.)
MYH7 - ventricular CM
MYH6 - atrial CM
C
Pacemaker-Conductive Cardiomyocytes (CPCS)
Ventricular conduction system (VCS)
1' - Purkinje fiber_CM (CSMD1, PLXNA4, BRINP3, SGCD, SEMA3A)
2' - Trans. Purkinje fiber_CM (CSMD1, PLXNA4, GJA1)
3' - AV bundle-bundle branch_CM (RCAN1, IRX1, IRX2, BRINP3)
HE + overlay
AVB-BB_CM
PF_CM
Cell state proportion
Atrial pacemaker-conduction system (APCS)
1' - SA node_CM (LRRC4C, TENM2, SHOX2, TBX18)
2' - AV node_CM (RSPO3, NRXN3, ZNF536, BMP2)
SAN_CM
AVN_CM
D
Markers of Cardiomyocyte States in APCS
Transcription factors
Axon guidance molecules
SHOX2
PRRX1
TBX18
ZNF385B
TENM2
TENM3
TENM4
GDF10
SLIT2
Avg. Exp.
Pct. Exp.
SAN_CM
AVN_CM
Cond_aCM
Left_aCM
Right_aCM
pcw 6.5
SAN
AVN
1 mm
E
Markers of Cardiomyocyte States in VCS
RCAN1
IRX1
IRX2
IRX5
BRINP3
SEMA3A
IRX3
CSMD1
PLXNA4
AVB-BB_CM
PF_CM
TsPF_CM
vCM_4
prox. VCS
dist. VCS
F
Ion Channel Profile of Fetal SAN_CM and AVN_CM
HCN channels
Ca2+ channels
K+ channels
Cl- channels
Ionotropic receptors
VRACs
TRP channels
Connexins
HCN1
HCN4
CACNA1C
CACNA1D
CACNA1G
CACNA2D2
CACNB2
KCNJ3
KCNN2
KCNQ1
KCNQ3
KCNQ5
(KCNT2)
CLCN3
CLIC4
ANO6
GRID2
GRIK1
LRRC8B
TRPC1
TRPC3
TRPM4
TRPM7
PKD2
GJA3
GJC1
Nodal cell action potential
Ion current
pcw 6.5
pcw 9
G
Gene Regulatory Network of Fetal SAN_CM
CACNB2
PBX1
RYR2
ESRRG
RORA
ZNF385B
NFIA
GRID2
KCNH7
TBX3
HCN1
SETBP1
PRDM16
TOX
THRB
SOX4
SHOX2
NPAS3
PRDM6
TBX18
TCF4
FOXP2
PRRX1
PITX2
TSHZ2
DACH1
PKNOX2
BNC2
SOX5
ID2
KCNQ5
ZNF608
KCNT2
NFIB
SMAD6
CACNA1D
TRPS1
BHLHE41
Transcription factor
Ion channel
Differentially expressed in SAN_CM (compared to all other CM clusters)

Figure 3

330 **Figure 3. Molecular Map of Cardiac Pacemaker-Conduction System Development. A.** UMAPs
331 displaying 7 coarse-grained and 19 fine-grained cardiomyocyte clusters, representing ventricular and atrial
332 contractile, immature, and pacemaker-conductive cell states. **B.** Feature plots of MYH7 and MYH6
333 outlining ventricular and atrial identities, respectively. **C.** Cardiomyocyte components of the cardiac
334 pacemaker-conduction system (CPCS) with characteristic markers and predicted localization in an 11 pcw
335 heart section. **D.** Dot plot representing selective enrichment of transcription factors and axon guidance
336 molecules in SAN_CMs and AVN_CMs, compared to mature contractile atrial cardiomyocytes (left).
337 Spatial enrichment of these genes in sinoatrial and atrioventricular nodes presented in a 6.5 pcw heart
338 section by ISS (right). **E.** Dot plot illustrating the relative expression of CPCS marker genes between
339 AVN-BB_CMs, PF_CMs, Ts-PF_CMs, and the contractile ventricular cardiomyocyte state vCM4 (left).
340 Spatial expression patterns of these genes, detected by ISS in a 9 pcw heart section, corroborating their
341 association with the proximal and distal ventricular conduction system (VCS) (right). **F.** Dot plot featuring
342 relative expression of selected ion channels in SAN_CMs and AVN_CMs, compared to contractile atrial
343 cardiomyocyte clusters (upper left). Illustration of ion currents of the nodal cell action (upper right).
344 Spatial pattern of HCN- and T-type $Ca^{2+}$ channel transcripts in 6.5 and 9 pcw heart sections, detected by
345 ISS (lower). **G.** Gene regulatory network of SAN_CMs, including the top 10 DE transcription factors
346 compared to all other cardiomyocyte cell states, and their associated target genes. In C-F panels: la–left
347 atrium, ra–right atrium, rv–right ventricle, ao–aorta, SAN–sinoatrial node, AVN–atrioventricular node,
348 VCS–ventricular conduction system, HE–hematoxylin-eosin; scale bars represent 1 mm.

349 **Early Formation of the Cardiac Autonomic Nervous System and Resident Chromaffin Cells**

350 Heart function is tightly controlled by the autonomic nervous system, relaying sympathetic and
351 parasympathetic signals to the cardiac tissue through the intracardiac ganglionated plexi (ICGP). Cells of
352 the ICGP are derived from the cardiac neural crest, but the precise course of this process in humans is yet
353 unknown[60].

354 To explore the early development of local cardiac innervation, we reclustered the coarse-grained
355 neuroblast-neuron (NB-N) and Schwann cell precursor-glial cell (SCP-GC) populations into ten fine-
356 grained clusters (Fig. 4A, Suppl. Fig. 4A, Suppl. Table 4). Six clusters showed enrichment of Schwann
357 cell precursor and glial cell transcription factors *SOX10* and *FOXD3*, and various levels of myelin-related
358 genes *MPZ*, *PMP22*, and *MBP*, outlining five SCP states gradually obtaining more mature glial

359 characteristics (SCP_1-5), as well as a population of myelinating Schwann cells (My_SC) (Fig. 4A-B,
360 Ext. Fig. 8). Based on their enrichment in neuronal markers *PRPH* and *STMN2,* we also identified two
361 clusters of autonomic neuroblasts and neurons (Aut_Neu_1-2), besides an intermediate bridge cell state
362 from SCPs, characterized by high *ASCL1* expression (Fig. 4A-B, Ext. Fig. 8). Notably, we detected a
363 cluster with strong enrichment of *CHGA*, *CHGB*, *PENK*, highlighting a local neuroendocrine chromaffin
364 cell population (Chrom_C) in the cardiac tissue (Fig. 4A-B, Ext. Fig. 8). This is, to our knowledge, the
365 first *in situ* observation of intracardiac chromaffin cells in the developing heart, which are not present in
366 the mouse model, and thus appear to be human-specific. To elucidate transitions between the annotated
367 cell states, we performed RNA velocity and pseudotime analysis on PCA embedding of the dataset, which
368 confirmed a fork-like transition from early Schwann cell precursor states towards two parallel trajectories,
369 consistent with the neuronal-chromaffin and glial differentiation paths (Fig. 4C-D, Ext. Fig. 8).

370 In agreement with the predominant positions of ICGP, chromaffin cells and autonomic neurons were
371 spatially mapped to the atrial wall and adventitia of the great arteries, where they appeared in closely
372 associated, but not overlapping spatial domains, underscoring their common origin, but diverging
373 functions (Fig. 4E, Suppl. Fig. 4B). Additionally, we observed Aut_Neu_2-dominated tissue segments in
374 close proximity to SAN_CMs, highlighting a neuronal structure likely responsible for direct innervation
375 of the nodal tissue (Fig. 4E). Most SCP cell states appeared more dispersed in the tissue, while the more
376 mature SCP_5 cells and My_SCs concentrated around peripheral nerve structures (Suppl. Fig. 4C).

377 We identified somatostatin (*SST*) as the main neurotransmitter gene expressed in the Aut_Neu_1 and
378 Aut_Neu_2 populations, besides the cholinergic neuron marker *CHAT* present in a smaller proportion of
379 these cells. Meanwhile, the Chrom_Cs were strongly enriched in *TH*, and to a lower extent in *DBH* and
380 *PNMT*, key genes of catecholamine synthesis (Fig. 4B, F). This suggests that neurons of the ICGP mostly
381 function through peptidergic, and to a lesser degree, cholinergic transmission at this developmental stage,
382 while the main source of norepinephrine (and to a lower extent, epinephrine) in the heart tissue is the local
383 chromaffin cell population. Interestingly, we found negligible expression of somatostatin receptors in our
384 datasets, meanwhile, β1 adrenergic receptor (*ADRB1*) was strongly enriched in the atrial, and M2
385 acetylcholine receptor (*CHRM2*) in almost all cardiomyocyte components of the pacemaker-conduction
386 system (Fig. 4F-G). Distinct sources of adrenergic and cholinergic mediation of sinoatrial node function
387 were reaffirmed by calculating a modified ligand-receptor score between the Chrom_C, Aut_Neu_2 and
388 SAN_CM states, considering the coordinated expression levels of key enzymes (*TH* and *CHAT*) and

389 receptors (*ADRB1* and *CHRM2*) between pairs of the analyzed cell states (Suppl. Fig. 4D). Additionally,
390 genes involved in regulating neuronal migration, neurite growth, axon guidance, and synapse formation
391 (such as teneurins, latrophilins, calsyntenins, neurexophilins, nectins, netrins, and components of the
392 SNARE complex) showed specific enrichment in subsets of SAN_CMs and AVN_CMs, as well as in the
393 Aut_Neu_1 and Aut_Neu_2 cell states (Suppl. Fig. 4E-F). Cell-cell communication analysis, based on
394 ligands and receptors specifically enriched in the SAN_CM and Aut_Neu_2 cell states, highlighted the
395 *PTPRS-NTRK3* interaction described in organizing excitatory synapses[61], and the *TENM2-ADGRL1* pair
396 known to induce axonal attraction on growth cones in the central nervous system[62] (Suppl. Fig. 4G). These
397 putative molecular interactions might be relevant for establishing precise connections between developing
398 cardiac innervation and pacemaker cells.

399 An essential function of chromaffin cells is mediating a physiological response to hypoxia through
400 increased catecholamine release. Accordingly, Chrom_Cs showed robust expression of molecular sensors
401 for local oxygen tension, including *EPAS1* (encoding HIF2$\alpha$), *COX4I2*, and *HIGD1C*, a mitochondrial
402 electron transport chain component recently described in the oxygen-sensing machinery of the carotid
403 body[63] (Fig. 4B).

404 Based on this insight, we propose a cellular model of the functional interplay between the developing
405 autonomic innervation, local chromaffin cells, and cardiomyocyte components of the early fetal human
406 heart, where local neurons convey parasympathetic signals, and sympathetic modulation is largely
407 mediated by a resident chromaffin cell population through a paracrine mechanism, in response to local
408 tissue hypoxia. Resulting changes in heart function are likely conveyed through the activation of various
409 ion channels in CPCS cardiomyocytes, adapting heart rate and conduction velocity to the environment of
410 the developing fetus (Fig. 4H). An intracardiac population of chromaffin cells might also explain the origin
411 and development of cardiac pheochromocytoma, a rare human condition when chromaffin cell tumors
412 form in the cardiac region[64].

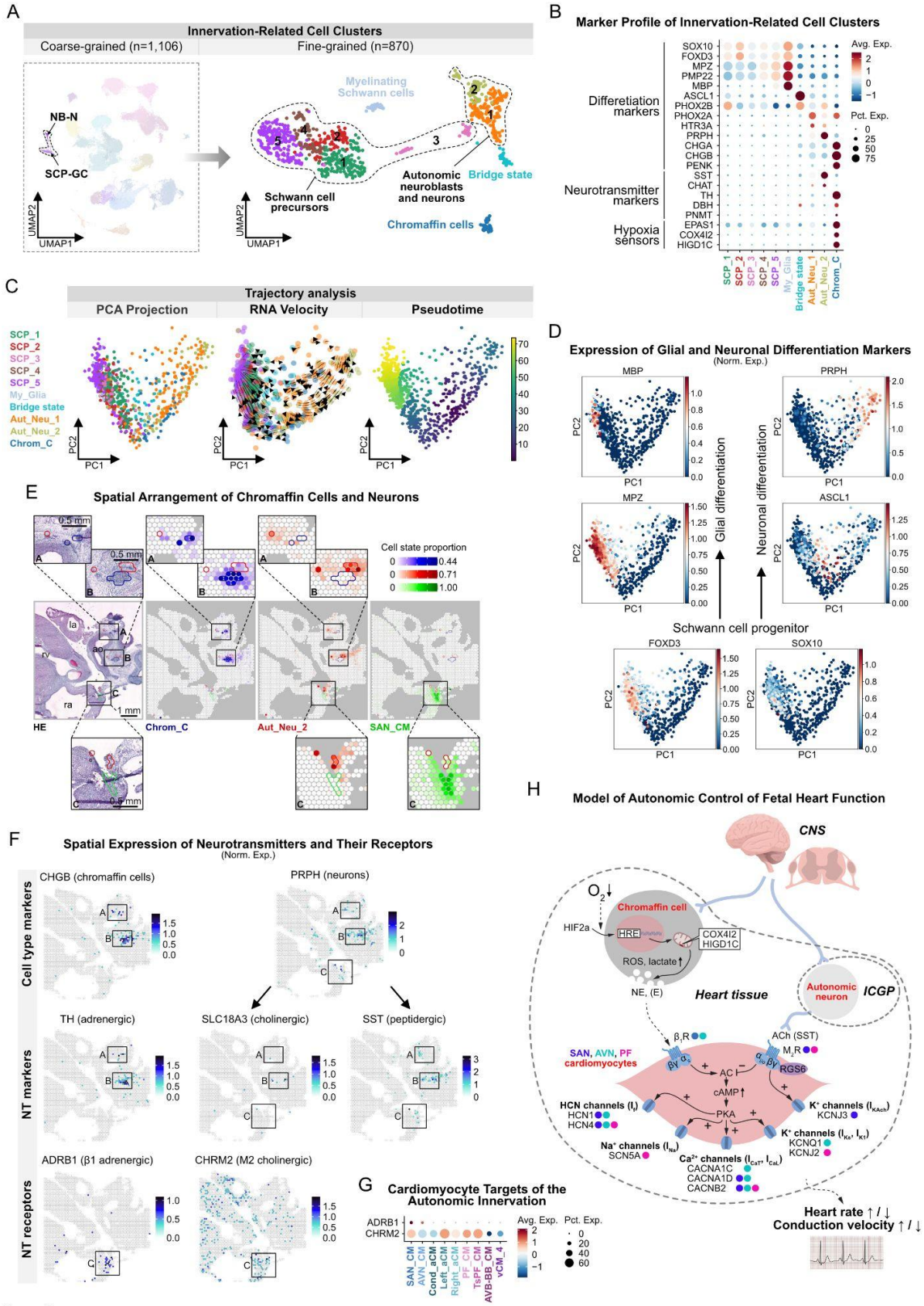
A
Innervation-Related Cell Clusters
Coarse-grained (n=1,106)
Fine-grained (n=870)
NB-N
SCP-GC
UMAP2
UMAP1
Myelinating Schwann cells
Schwann cell precursors
Autonomic neuroblasts and neurons
Bridge state
Chromaffin cells
B
Marker Profile of Innervation-Related Cell Clusters
Differetiation markers
Neurotransmitter markers
Hypoxia sensors
SOX10
FOXD3
MPZ
PMP22
MBP
ASCL1
PHOX2B
PHOX2A
HTR3A
PRPH
CHGA
CHGB
PENK
SST
CHAT
TH
DBH
PNMT
EPAS1
COX4I2
HIGD1C
Avg. Exp.
Pct. Exp.
SCP_1
SCP_2
SCP_3
SCP_4
SCP_5
My_Glia
Bridge state
Aut_Neu_1
Aut_Neu_2
Chrom_C
C
Trajectory analysis
PCA Projection
RNA Velocity
Pseudotime
PC1
PC2
D
Expression of Glial and Neuronal Differentiation Markers
(Norm. Exp.)
MBP
PRPH
MPZ
ASCL1
Glial differentiation
Neuronal differentiation
Schwann cell progenitor
FOXD3
SOX10
E
Spatial Arrangement of Chromaffin Cells and Neurons
Cell state proportion
HE
Chrom_C
Aut_Neu_2
SAN_CM
F
Spatial Expression of Neurotransmitters and Their Receptors
(Norm. Exp.)
Cell type markers
NT markers
NT receptors
CHGB (chromaffin cells)
PRPH (neurons)
TH (adrenergic)
SLC18A3 (cholinergic)
SST (peptidergic)
ADRB1 (β1 adrenergic)
CHRM2 (M2 cholinergic)
G
Cardiomyocyte Targets of the Autonomic Innervation
ADRB1
CHRM2
SAN_CM
AVN_CM
Cond_aCM
Left_aCM
Right_aCM
PF_CM
TsPF_CM
AVB-BB_CM
vCM_4
Avg. Exp.
Pct. Exp.
H
Model of Autonomic Control of Fetal Heart Function
CNS
Chromaffin cell
HIF2a
HRE
COX4I2
HIGD1C
ROS, lactate
NE, (E)
Heart tissue
Autonomic neuron
ICGP
ACh (SST)
SAN, AVN, PF cardiomyocytes
RGS6
AC
cAMP
PKA
HCN channels
HCN1
HCN4
K+ channels
KCNJ3
KCNQ1
KCNJ2
Na+ channels
SCN5A
Ca2+ channels
CACNA1C
CACNA1D
CACNB2
Heart rate ↑ / ↓
Conduction velocity ↑ / ↓

Figure 4

414 **Figure 4. Early Formation of the Autonomic Cardiac Nervous System and Resident Chromaffin**
415 **Cells. A.** UMAPs showing the neuroblast-neuron (NB_N) and Schwann cell progenitor-glial cell (SCP-
416 GC) coarse-grained, and 10 fine-grained clusters related to cardiac autonomic innervation. **B.** Dot plot
417 illustrating the relative expression of glial, neuronal, and chromaffin cell differentiation markers,
418 neurotransmitter-related genes, and components of the acute oxygen-sensing machinery, across all fine-
419 grained innervation-related cell clusters. **C.** RNA velocity and pseudotime analysis revealing two parallel
420 developmental trajectories among innervation-related cell clusters. **D.** Expression of glial and neuronal
421 differentiation markers. **E.** Spatial mapping of Chrom_C (blue), Aut_Neu_2 (red) and SAN_CM (green)
422 cell states in a 11 pcw heart section, outlining their neighboring compartments in the adventitia of the
423 great vessels (ROI A-B), and an Aut_Neu_2 subset in proximity to the sinoatrial node (ROI C). Scale bars
424 represent 1 mm in the main, and 0.5 mm in the zoom-in panels. **F.** Spatial feature plots of neurotransmitter
425 metabolism-related genes and receptors in the same section, with consistent positions of ROI A-C. **G.** Dot
426 plot presenting enrichment of β1 adrenergic and M2 cholinergic receptor transcripts in pacemaker-
427 conduction system cardiomyocytes. **H.** Proposed model of autonomic control of fetal heart function.
428 ICGP–intracardiac ganglionated plexi, SAN–sinoatrial node, AVN–atrioventricular node, PF–Purkinje
429 fibers, CNS–central nervous system, ROS–reactive oxygen species. In panel D: la–left atrium, ra–right
430 atrium, rv–right ventricle, ao–aorta, HE–hematoxylin-eosin.

431 **Position-Dependent Endothelial Cell Diversity in Endocardial Cushion-Derived Structures**

432 Cardiac endothelial cells (EC) can be divided into vascular and endocardial subsets. With the swift growth
433 of coronary vessels during the 1$^{st}$ trimester, the vascular endothelium rapidly expands and diversifies.
434 Meanwhile, the endocardium gives rise to endocardial cushions, contributing to the subsequent formation
435 of cardiac valves, atrial septum and the upper membranous septum of the ventricles. The major cardiac
436 endothelial populations were recently characterized in the fetal human heart[28], however, we still lack a
437 detailed, transcriptome-wide description of the scarce endocardial cushion-related endothelial cells and
438 their various derivatives[23,65].

439 In the merged population of coarse-grained endothelial cells and TMSB10$^{high}$_C_2 clusters featuring
440 endothelial transcriptional characteristics, we defined 18 fine-grained cell states, representing the
441 endocardium (EndocEC_1-4), endothelium of large arteries and veins (Atr_EC_1 and Ven_EC), and
442 consecutive segments of the coronary vasculature, including arterial (Art_EC_2), arteriolar (Arteriol_EC),

443 capillary (Cap_EC_1-2) and venular (Venul_EC) endothelial cells. We also recognized separate
444 populations of proliferating (Prol_EC) and lymphatic endothelial cells (LEC$^{fg}$), as well as distinct
445 populations of thymosin- (TMSB10$^{high}$_C_2$^{fg}$) and PDE4C-enriched cells (PDE4C$^{high}$_EC) (Fig. 5A,
446 Suppl. Fig. 5A-C, Suppl. Table 5).

447 Three additional clusters appeared closely related to endocardial cell states but were also enriched in key
448 regulators of endothelial-to-mesenchymal transition (EndMT) (*NFATC1*, *APCDD1*, *TWIST1)*, central in
449 endocardial cushion formation (Suppl. Fig. 5B, Suppl. Table 5). Accordingly, spatial mapping traced two
450 of these cell states to opposite sides of the developing heart valves, outlining inflow (IF_VEC) and outflow
451 (OF_VEC) valve endothelial cell populations, consistently in the atrioventricular and semilunar valves
452 (Fig. 5B). This pattern was already apparent in primitive endocardial cushions from as early on as 6
453 postconceptional weeks, suggesting early specification of these populations (Suppl. Fig. 5D). Meanwhile,
454 the third cluster showed highly distinct localization in the atrial septum (AtrSept_EC), illuminating a yet
455 undescribed cardiac endothelial cell state (Fig. 5B, Suppl. Fig. 5E). Beyond several common markers,
456 these three populations featured largely distinct transcriptional profiles (Suppl. Fig. 5A, F-G). Highly
457 enriched genes of IF_VECs included several components of the WNT signaling axis (*WNT2*, *WNT4*,
458 *WNT9B*, *DKK2*, *PTHLH*), with many of them displaying spatial enrichment in the coaptation zone of the
459 valves (Fig. 5C). OF_VECs, on the other hand, displayed high expression of BMP ligands (*BMP4*, *BMP6*),
460 WNT signaling modulators (*LGR5*), as well as the endocannabinoid receptor-encoding *CNR1*, showing
461 spatial enrichment on the fibrosa side of the valves (Fig. 5C). AtrSept_ECs shared some highly enriched
462 genes (*LRRC4C*, *LSAMP*, *OPCML)* with the Endoc_EC_4 cell state, outlining the smooth-walled atrium,
463 besides more specific markers (*NEGR1*, *ALCAM*, *SEMA3A*, *CCDC80, MSX1*) (Suppl. Fig. 5A, E, Suppl.
464 Table 5).

465 Gene regulatory network and regulon enrichment analysis gave further insight into the molecular
466 differences between the three endocardial cushion-related cell states (Fig. 5D-E). We identified *MSX1* and
467 *LEF1*, known mediators of EndMT during endocardial cushion formation, as the most highly enriched
468 transcription factors in AtrSept_ECs. Besides the cardiac valve mesenchyme, *LEF1* is also expressed in
469 the mesenchymal cap of the developing atrial septum in mice[66], and a recent report described atrial septal
470 defect in a patient carrying a heterozygous missense variant of this gene[67]. *MSX1* was also detected in the
471 atrial septum of the mouse heart[68], and several recent animal and human studies proposed a potential
472 association between atrial septal defects and genetic variants of the *MSX1* locus[68–70]. In OF_VECs, we

473 found enrichment of *PROX1* and *FOXC2* transcription factors, known to act in concert in response to
474 oscillatory shear stress, maintaining extracellular matrix structure and preventing myxomatous
475 degeneration of cardiac valves[71]. Several transcription factors enriched in IF_VECs have an established
476 role in the modulation of WNT signaling, including *KLF4* and *SMAD6*, which are known transducers of
477 laminar shear stress in endothelial cells[72,73]. Importantly, we observed pronounced differences in the
478 regulon enrichment of these transcription factors between IF_VECs and OF_VECs from as early on as
479 5.5-6 postconceptional weeks, suggesting that hemodynamic forces, already in the embryonic period, are
480 core factors in valve endothelial cell diversification.

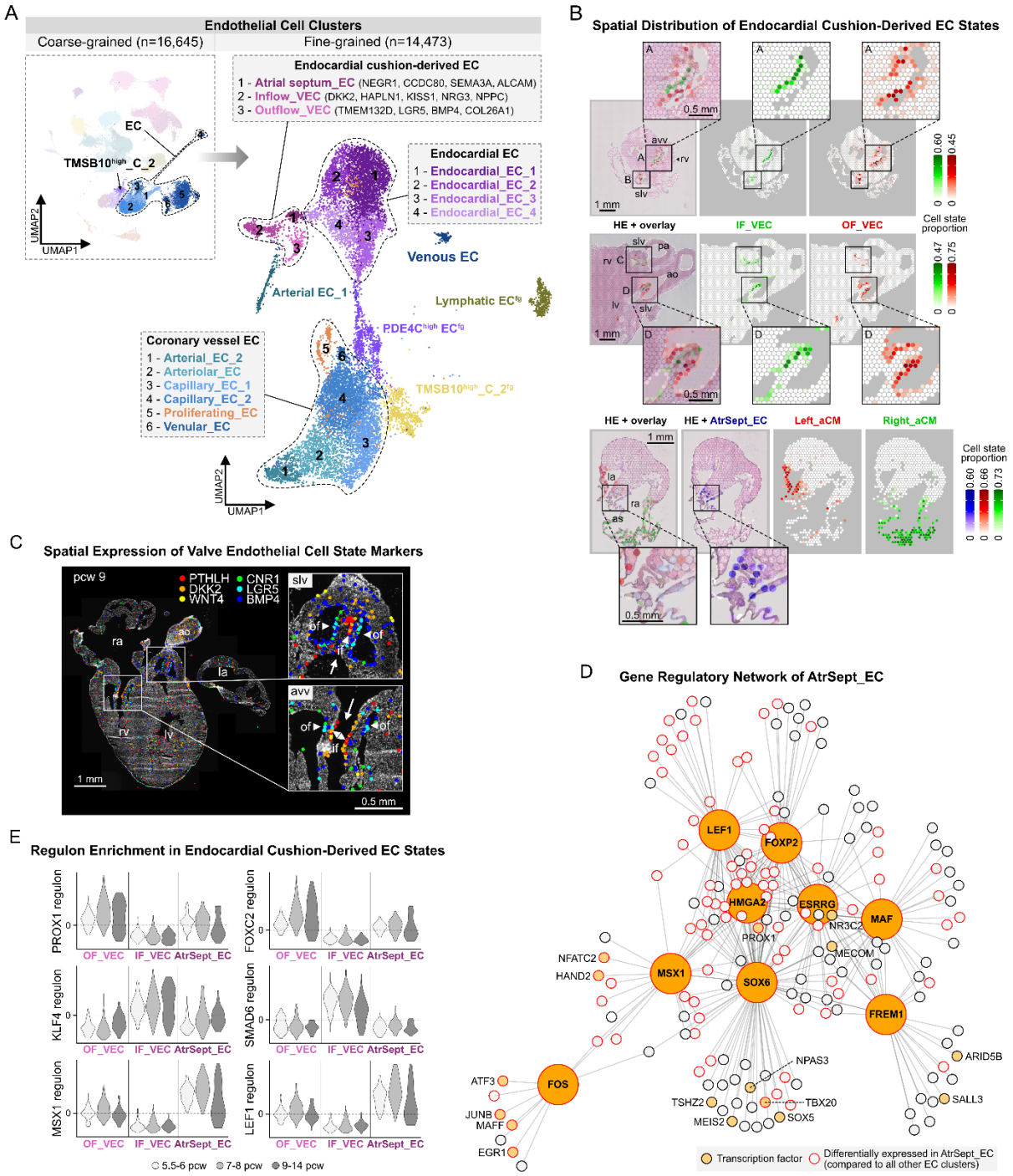
A
Endothelial Cell Clusters
Coarse-grained (n=16,645)
Fine-grained (n=14,473)
EC
TMSB10high_C_2
UMAP2
UMAP1
Endocardial cushion-derived EC
1 - Atrial septum_EC (NEGR1, CCDC80, SEMA3A, ALCAM)
2 - Inflow_VEC (DKK2, HAPLN1, KISS1, NRG3, NPPC)
3 - Outflow_VEC (TMEM132D, LGR5, BMP4, COL26A1)
Endocardial EC
1 - Endocardial_EC_1
2 - Endocardial_EC_2
3 - Endocardial_EC_3
4 - Endocardial_EC_4
Venous EC
Arterial EC_1
Lymphatic ECfg
PDE4Chigh ECfg
TMSB10high_C_2fg
Coronary vessel EC
1 - Arterial_EC_2
2 - Arteriolar_EC
3 - Capillary_EC_1
4 - Capillary_EC_2
5 - Proliferating_EC
6 - Venular_EC
B
Spatial Distribution of Endocardial Cushion-Derived EC States
HE + overlay
IF_VEC
OF_VEC
Cell state proportion
HE + AtrSept_EC
Left_aCM
Right_aCM
C
Spatial Expression of Valve Endothelial Cell State Markers
pcw 9
PTHLH
DKK2
WNT4
CNR1
LGR5
BMP4
ra
ao
la
rv
lv
slv
avv
of
if
1 mm
0.5 mm
D
Gene Regulatory Network of AtrSept_EC
LEF1
FOXP2
HMGA2
ESRRG
MAF
NR3C2
PROX1
MECOM
NFATC2
HAND2
MSX1
SOX6
FREM1
ARID5B
NPAS3
ATF3
FOS
JUNB
MAFF
EGR1
TSHZ2
TBX20
MEIS2
SOX5
SALL3
Transcription factor
Differentially expressed in AtrSept_EC (compared to all other EC clusters)
E
Regulon Enrichment in Endocardial Cushion-Derived EC States
PROX1 regulon
FOXC2 regulon
KLF4 regulon
SMAD6 regulon
MSX1 regulon
LEF1 regulon
OF_VEC
IF_VEC
AtrSept_EC
5.5-6 pcw
7-8 pcw
9-14 pcw

Figure 5

482 **Figure 5. Position-Dependent Endothelial Cell Diversity in Endocardial Cushion-Derived**
483 **Structures. A.** UMAPs displaying 6 coarse-grained endothelial cell (EC)- and the TMSB10$^{high}$_C_2
484 clusters, divided into 18 fine-grained cell states, representing endocardial, endocardial cushion-derived,
485 and coronary vessel endothelial cells, along with additional minor populations. **B.** Spatial mapping tracing
486 IF_VECs (green) and OF_VECs (red) to opposite sides of the atrioventricular (ROI A) and semilunar
487 valves (ROI B-D) in 8 (upper) and 12 pcw (middle) heart sections, and AtrSept_ECs (blue) to the atrial
488 septum between Right_aCM- (green) and Left_aCM (red)-dominated areas, in 8 pcw heart section (lower).
489 Scale bars represent 1 mm in the main, and 0.5 mm in the zoom-in panels. **C.** Side-specific spatial
490 enrichment of selected IF_VEC and OF_VEC markers in atrioventricular and semilunar valves in a 9 pcw
491 heart section, detected by ISS. White arrows mark the direction of blood flow. Scale bar represents 1 mm.
492 **D.** Gene regulatory network of AtrSept_EC, including enriched transcription factors compared to
493 IF_VECs and OF_VECs, and their associated target genes. **E.** Violin plots illustrating regulon enrichment
494 of selected transcription factors in AtrSept_ECs, IF_VECs, and OF_VECs across three age groups (5.5-
495 6, 7-8, 9-14 pcw). In panels B-C: slv–semilunar valve, avv–atrioventricular valve, rv–right ventricle, lv–
496 left ventricle, ao–aorta, pa–pulmonary artery, as–atrial septum, if–inflow side of valve, of–outflow side of
497 valve, HE–hematoxylin-eosin.

498 **Spatial Decomposition of Fibroblast and Mesenchymal Cell Heterogeneity in the Developing Heart**

499 Fibroblasts (FB) and mesenchymal cells (MC) constitute an ambiguous subset of cardiac cells during
500 development, largely due to their pronounced transcriptional heterogeneity and a lack of well-established
501 molecular markers. Spatial factors, reflecting the positions of their progenitors and niche-related
502 environmental signals, play a central role in defining cellular identities in this population[74].

503 To explore this topological diversity, we spatially mapped 18 fine-grained fibroblast and mesenchymal
504 cell clusters distinguished in our dataset (Fig. 6A, Suppl. Fig. 6A-B, Suppl. Table 6), tracing most to
505 characteristic tissue locations. Accordingly, we recognized two adventitial fibroblast states (Adv_FB_1-
506 2), with Adv_FB_1 outlining the wall of the outflow tract and great arteries, and Adv_FB_2 also appearing
507 around large coronary arteries (Fig. 6B). An additional mesenchymal cell population, resembling the
508 pericyte transcriptional signature (Peric_MC$^{fg}$), was traced to the innermost layer of the ventricular
509 myocardium, as well as to the atrial walls, to positions complementary to the genuine pericyte population

510 (Fig. 6B, Suppl. Fig. 6A-B). This localization is suggestive of a potential endocardial origin, which has
511 recently been proposed for a pericyte-like cardiac mesenchymal cell state in mice[75].

512 Furthermore, we identified two populations representing early forms of epicardium-derived progenitor
513 cells (EDPC), based on their predicted positions in the subepicardium at the atrioventricular groove
514 (EPDC_1) and the heart surface (EPDC_2), and combined enrichment of the epicardial marker *WT1* and
515 EPDC marker *TCF21* (Fig. 6C, Suppl. Fig. 6B). A third *WT1*-enriched cell state, also expressing high
516 levels of *CACNA2D3* and *BRINP3*, appeared in a distinct layer between the atria and ventricles, outlining
517 the fibrous cardiac skeleton (AnnFibr_FB), beside a fourth population marked by inflammatory gene
518 expression (Inf_FB) (Fig. 6C, Suppl. Fig. 6A). We also found various cell states consistent with an
519 interstitial fibroblast phenotype, characterized by high *CD34* expression and gradual temporal expansion
520 from the epicardium to the outer (Int_FB_1) and inner (Int_FB_2) layers of the ventricular wall, or located
521 in the subendocardium and the atrioventricular region (Int_FB_3) (Fig. 6D, Suppl. Fig. 6B). Int_FB_1 and
522 Int_FB_2 exhibited the highest *TCF21* expression in our dataset, indicating advanced transition from an
523 epicardial progenitor state towards fibroblast identity (Suppl. Fig. 6B). Notably, we also recognized a
524 distinct cell state with robust *CD34* expression, dynamic temporal expansion, and a transcriptomic profile
525 resembling fibro-adipogenic progenitors (FAP; *CLEC3B, ROBO2, SEMA3C, ADAMTSL1, CCN3, SOX9,*
526 *DLK1*) (Suppl. Fig. 6A-C). Many of these markers appeared closely associated in a gene regulatory
527 network defined by three transcription factors enriched in this population: while *ZBTB16* promotes white
528 and brown adipogenesis[76], *KLF2* and *GLIS3* block further adipogenic differentiation of preadipocytes[77,78],
529 consistent with the progenitor characteristics of this cell state (Suppl. Fig. 6D). Spatial mapping located
530 this population near EPDC_1 cells in the atrioventricular groove, reflecting the predominant localization
531 of the primordial epicardial adipose tissue (EAT), as well as a presumed epicardial origin of these cells
532 (Fig. 6C). FAPs have been proposed as potential sources of fatty-fibrous tissue deposits, a histological
533 hallmark in arrhythmogenic right ventricular cardiomyopathy (ARVC)[79]. Importantly, we found two
534 ARVC-associated desmosome-encoding genes (*PKP4*, *DSC2*) enriched in the FAP cell state, drawing a
535 potential connection towards the pathogenesis of the disease[80] (Suppl. Table 6).

536 Our clustering also identified three distinct mesenchymal cell states in the developing endocardial
537 cushions and cardiac valves (Fig. 6E, Suppl. Fig. 6E-F). Valve interstitial cells (VIC; *APCDD1*, *LEF1*,
538 *TMEM132C, ADAMTS19*) localized to the free segments of the valves, while the other two populations
539 (Valve_MC_1-2) stretched from the intervalvular fibrous region towards the valve roots, with

540 Valve_MC_1 (*FGF14*, *HDAC9*, *PLCXD3*) being spatially enriched around the semilunar valves.
541 Importantly, Valve_MC_2 featured a specific and robust expression of *PENK*, a previously described
542 marker of mesenchymal neural crest derivatives in mouse hearts[34] (Suppl. Fig. 6A-B, E) . Importantly, we
543 observed strong spatial *PENK* signal in and around the developing semilunar and atrioventricular valves,
544 supporting the long-debated contribution of neural crest cells to both valve structures in humans. In fact,
545 we observed *PENK* expression in the septal leaflets of atrioventricular valves already in the 6.5$^{th}$
546 postconceptional week, which appeared more spread out towards the free wall leaflets by the 9$^{th}$ week,
547 along with semilunar valve-related *PENK* signal present in both sampled aortic valve cusps (Fig. 6F).
548 Taken together, our results imply a more substantial contribution of neural crest-derived mesenchyme to
549 human cardiac valves than previously assumed. Based on these results, we assembled a spatial model of
550 mesenchymal and fibroblast-like cell states contributing to the fibrous skeleton and embedded valve
551 structures in the fetal heart, representing epicardial, endocardial and neural crest derivatives (Fig. 6G).

552 Beyond clusters with characteristic spatial distributions, we also identified a cell cycle marker- (Prol_FB)
553 and a PDE4C-enriched cell state (PDE4C$^{high}$_FB$^{fg}$), beside a fibroblast population (CALN1$^{high}$_FB)
554 featuring high expression of characteristic nodal cell genes (*CALN1*, *SHOX2*, *CNTN5*), as well as the
555 angiotensinogen-encoding *AGT*, a central component of local renin-angiotensin circuits in nodal tissue
556 (Suppl. Fig. 6A, Suppl. Table 6). The latter observation highlights this population as potential
557 developmental equivalents of sinoatrial and atrioventricular node-resident fibroblasts.

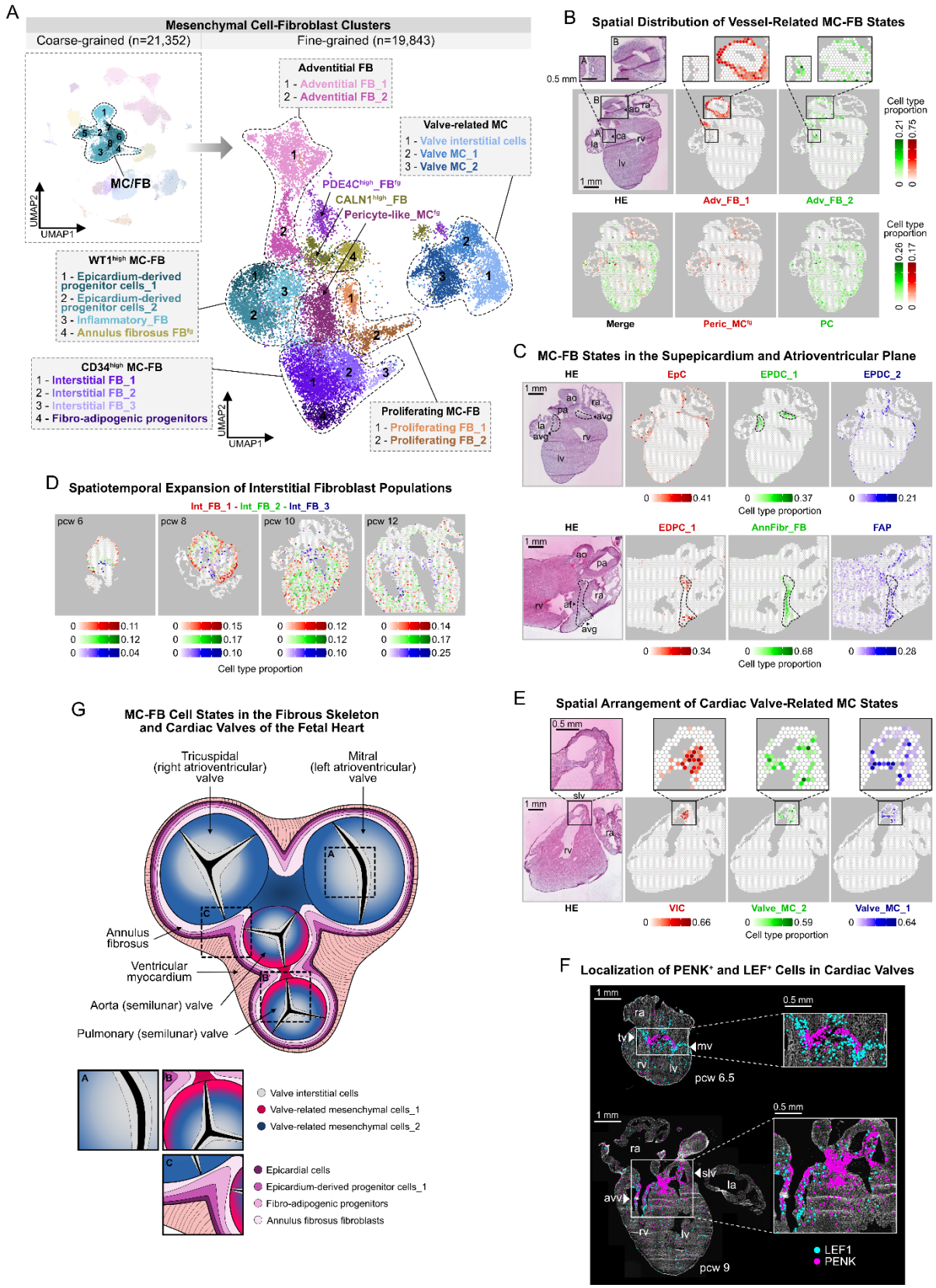
A
Mesenchymal Cell-Fibroblast Clusters
Coarse-grained (n=21,352)
Fine-grained (n=19,843)
MC/FB
UMAP2
UMAP1
Adventitial FB
1 - Adventitial FB_1
2 - Adventitial FB_2
Valve-related MC
1 - Valve interstitial cells
2 - Valve MC_1
3 - Valve MC_2
PDE4C^high_FB^fg
CALN1^high_FB
Pericyte-like_MC^fg
WT1^high MC-FB
1 - Epicardium-derived progenitor cells_1
2 - Epicardium-derived progenitor cells_2
3 - Inflammatory_FB
4 - Annulus fibrosus FB^fg
CD34^high MC-FB
1 - Interstitial FB_1
2 - Interstitial FB_2
3 - Interstitial FB_3
4 - Fibro-adipogenic progenitors
Proliferating MC-FB
1 - Proliferating FB_1
2 - Proliferating FB_2
B
Spatial Distribution of Vessel-Related MC-FB States
0.5 mm
1 mm
Cell type proportion
HE
Adv_FB_1
Adv_FB_2
Merge
Peric_MC^fg
PC
C
MC-FB States in the Supepicardium and Atrioventricular Plane
HE
EpC
EPDC_1
EPDC_2
EDPC_1
AnnFibr_FB
FAP
Cell type proportion
D
Spatiotemporal Expansion of Interstitial Fibroblast Populations
Int_FB_1 - Int_FB_2 - Int_FB_3
pcw 6
pcw 8
pcw 10
pcw 12
Cell type proportion
E
Spatial Arrangement of Cardiac Valve-Related MC States
HE
VIC
Valve_MC_2
Valve_MC_1
Cell type proportion
F
Localization of PENK+ and LEF+ Cells in Cardiac Valves
pcw 6.5
pcw 9
LEF1
PENK
G
MC-FB Cell States in the Fibrous Skeleton and Cardiac Valves of the Fetal Heart
Tricuspidal (right atrioventricular) valve
Mitral (left atrioventricular) valve
Annulus fibrosus
Ventricular myocardium
Aorta (semilunar) valve
Pulmonary (semilunar) valve
Valve interstitial cells
Valve-related mesenchymal cells_1
Valve-related mesenchymal cells_2
Epicardial cells
Epicardium-derived progenitor cells_1
Fibro-adipogenic progenitors
Annulus fibrosus fibroblasts

Figure 6

559 **Figure 6. Spatial Decomposition of Fibroblast and Mesenchymal Cell Heterogeneity in the**
560 **Developing Heart. A.** UMAPs displaying 8 coarse-grained and 18 fine-grained fibroblast (FB) and
561 mesenchymal cells (MC) clusters, representing WT1- and CD34-enriched, adventitial, valve-related and
562 proliferating subsets, along with additional minor populations. **B.** Spatial mapping, tracing Adv_FB_1
563 (red) and Adv_FB_2 (green) cells to the great arteries (ROI B) and coronary arteries (ROI A), respectively
564 (upper), and Peric_MC$^{fg}$ (red) and PC (green) cells to complementary positions in the atrial and ventricular
565 myocardium, in a 10 pcw heart section. **C.** Spatial mapping, tracing EpC (red), EPCD_1 (green), and
566 EPCD_2 (blue) cells to the heart surface in a 10 pcw (upper), and EPCD_1 (red), AnnFibr_FB (green)
567 and FAP (blue) cells to the atrioventricular plane and groove (dashed lines) in an 11 pcw heart section. **D.**
568 Spatial mapping of Int_FB_1 (red), Int_FB_2 (green) and Int_FB_3 (blue) cells, illustrating their gradual
569 spatial expansion and layer-specific positions in 6, 8, 10, and 12 pcw heart sections. **E.** Spatial mapping
570 of VIC (red), Valve_MC_2 (green) and Valve_MC_1 (blue) cells in an 11 pcw heart section, displaying
571 their enrichment in and around the semilunar valve cusps. **F.** ISS detection of *PENK* and *LEF1* in cardiac
572 valves in 6.5 and 9 pcw heart sections. **G.** Spatial model of fibroblast and mesenchymal cell state
573 arrangements in the fetal heart's fibrous skeleton and cardiac valves. In panel B-C, E-F: rv–right ventricle,
574 lv–left ventricle, ra–right atrium, la–left atrium, ao–aorta, ca–coronary artery, pa–pulmonary artery, avg–
575 atrioventricular groove, af–annulus fibrosus, mv–mitral valve, tv–tricuspid valve, HE–hematoxylin-eosin;
576 scale bars represent 1 mm in the main, and 0.5 mm in the zoom-in panels.

577 **Spatially Informed Analysis of Developmental Cardiac Niches**

578 During cardiogenesis, rapid formation and rearrangements of cellular microcompartments play
579 fundamental roles in conveying external signals and cues to cardiac cells, regulating their behavior in the
580 evolving organ. Hence, our objective was to utilize our in-depth spatial analysis to outline the dominant
581 cell types in major structural compartments and more refined niches in the developing heart, expecting
582 that their focused interrogation would aid in understanding the cellular and molecular mechanisms that
583 govern both normal and pathological heart formation. Accordingly, we assessed the overlap of predicted
584 spatial distributions between the 72 fine-grained single-cell states in our dataset and used in-pair
585 correlation-based co-detection scores to visualize their topological relations (Fig. 7A, Suppl. Table 7).
586 With this strategy, we were able to decipher the cellular composition of larger and smaller tissue
587 compartments consistently across three developmental age groups, confirming the robustness of our
588 approach (Suppl. Fig. 7A).

589 Our analysis provided additional insight into the cellular composition and molecular interaction within
590 the cardiac pacemaker-conduction system (CPCS). We found substantial overlap between predicted
591 positions of CALN1$^{high}$_FBs, SAN_CMs and AVN_CMs, providing further support to our assumption
592 that CALN1$^{high}$_FBs, in fact, represent a mesenchymal component of the developing nodal tissue. Of note,
593 AVN_CMs showed the highest spatial co-detection scores with the AtrSept_EC state, implying the
594 presence of conductive cardiomyocytes in the atrial septum of the fetal heart (Fig. 7B). We also identified
595 several potential ligand-receptor pairs between SAN_CMs and their cellular surroundings (Figure 7C)
596 using a recently published neural-GPCR module of CellPhoneDB[51]. These include multiple putative
597 interactions directed from the pacemaker cells towards closely localized venous endothelial cells
598 (Ven_EC), as well as molecular pairs likely involved in contact formation with autonomic neurons
599 (Aut_Neu_2). Notably, CALN1$^{high}$_FBs displayed a significant overlap in their interaction profile with
600 SAN-CMs to a glial cell state recently discovered in the adult heart[51], which suggests a potential hybrid
601 function for this cell state in the developing heart. The ventricular CPCS components showed closest
602 association with each other, and two ventricle-enriched endocardial cell states (Endoc_EC_1-2). We
603 observed a temporal shift in the codetection of PF_CMs from Endoc_EC_1 towards Endo_EC_2, as well
604 as differences in ligand-receptor interactions related to trabeculae formation and Purkinje fiber
605 specification, highlighting functionally relevant molecular heterogeneity in the ventricular endocardium
606 (Suppl. Fig. 7B).

607 Our analysis also demonstrated compositional differences between the great arteries (Art_EC_1,
608 OFT_SMC, Adv_FB_1-2) and coronary arteries (Art_EC_2, CA_SMC, Adv_FB_2), consistent with
609 differences in their developmental origins and functions, and a close spatial association between lymphatic
610 endothelial (LEC$^{fg}$) and myeloid cells (My_C), essential for *de novo* lymphangiogenesis (Suppl. Fig.
611 7C)[81]. In parallel, we observed a temporal decrease of co-detection scores between endothelial cell states
612 in consecutive segments of the coronary vasculature (Art_EC_1-2, Arteriol_EC, Cap_EC_1-2), reflecting
613 their gradual spatial separation (Suppl. Fig. 7D).

614 By identifying five, spatially distinct valvular endothelial and mesenchymal cell states, our study
615 delineates the developing human cardiac valve architecture with unprecedented spatial and cellular
616 resolution (Fig. 7D)[65,82]. Hence, we used this insight to map the distribution of WNT, BMP and TGFβ
617 signaling network components, known to orchestrate valvulogenesis in a nuanced spatiotemporal manner,
618 and also to be involved in the development of congenital and acquired valve disease (Fig. 7E)[83]. Notably,

619 the endothelial populations showed the most distinct pattern of these transcripts, with IF_VECs displaying
620 pronounced enrichment of WNT ligands (*WNT2*, *WNT2B*, *WNT4*, *WNT9B*, *WNT11*), antagonists and
621 signaling inhibitors (*ZNRF3*, *DKK2*, *DKK3*), while OF_VECs showing higher expression of WNT
622 receptors (*FZD10*, *ROR1*, *ROR2*) and signal enhancers (*LGR5*), besides certain BMP ligands (*BMP4,*
623 *BMP6*) and antagonists (*SOST*, *FST*, *FSTL4*). Fluid forces, acting through the laminar flow-induced KLF2
624 (and KLF4) transcription factors, have been identified as major regulators of the activation of WNT-, and
625 suppression of BMP-mediated signaling[72,84]. Accordingly, side-specific enrichment of WNT and BMP
626 ligands in cardiac valves has been observed in several animal models, however, our study is the first to
627 present consistent compartmentalization of various components of these signaling networks in developing
628 human hearts. Regarding the TGFβ axis, cell state-related differences appeared less pronounced, with
629 IF_VECs expressing higher levels of ligands (*TGFB1*, *TGFB2*), and OF_VECs of signaling modulators
630 (*LTBP1*, *BAMBI*, *THBS1*). The valvular mesenchymal cell populations exhibited a more homogenous
631 expression profile of these genes, including common enrichment of *WNT5B* and *RORA*, mediators of non-
632 canonical WNT signaling, which has shown a positive correlation with the amount of calcification and
633 fibrosis in diseased adult aortic valves[85]. Notably, Valve_MC_1 cells showed strong enrichment of
634 *RSPO2*, implicated in the development of bicuspid aortic valve disease[86,87], and Valve_MC_2 cells of
635 *FMOD*, which has been proposed as a key molecule in the formation of a fibrous anchor area between
636 cardiac valves and adjacent tissue segments[86], consistent with the predominant localization of these
637 clusters.

638 Cardiac valves are often affected in congenital and acquired heart diseases, however, the cellular culprits
639 in these pathologies are often unclear. Thus, we explored the expression pattern of genes implicated in
640 syndromic and non-syndromic forms of two major cardiac valve anomalies, bicuspid aortic valve disease
641 (BAV) and mitral valve prolapse (MVP)[88–90], across the valvular cell states (Fig. 7F). While most MVP-
642 related genes, even in the non-syndromic form of the disease, appeared to have a broad distribution, many
643 genes causing non-syndromic forms of BAV showed strong enrichment in IF_VECs and VICs, outlining
644 these cell states as most susceptible to alterations of the analyzed genes. Our results showcase how future
645 genetic studies on cardiac malformations could benefit from the spatially informed cell state
646 decomposition of our dataset, providing support to potential gene-disease associations by presenting
647 enrichment of pathological gene candidates in relevant developmental cell states.

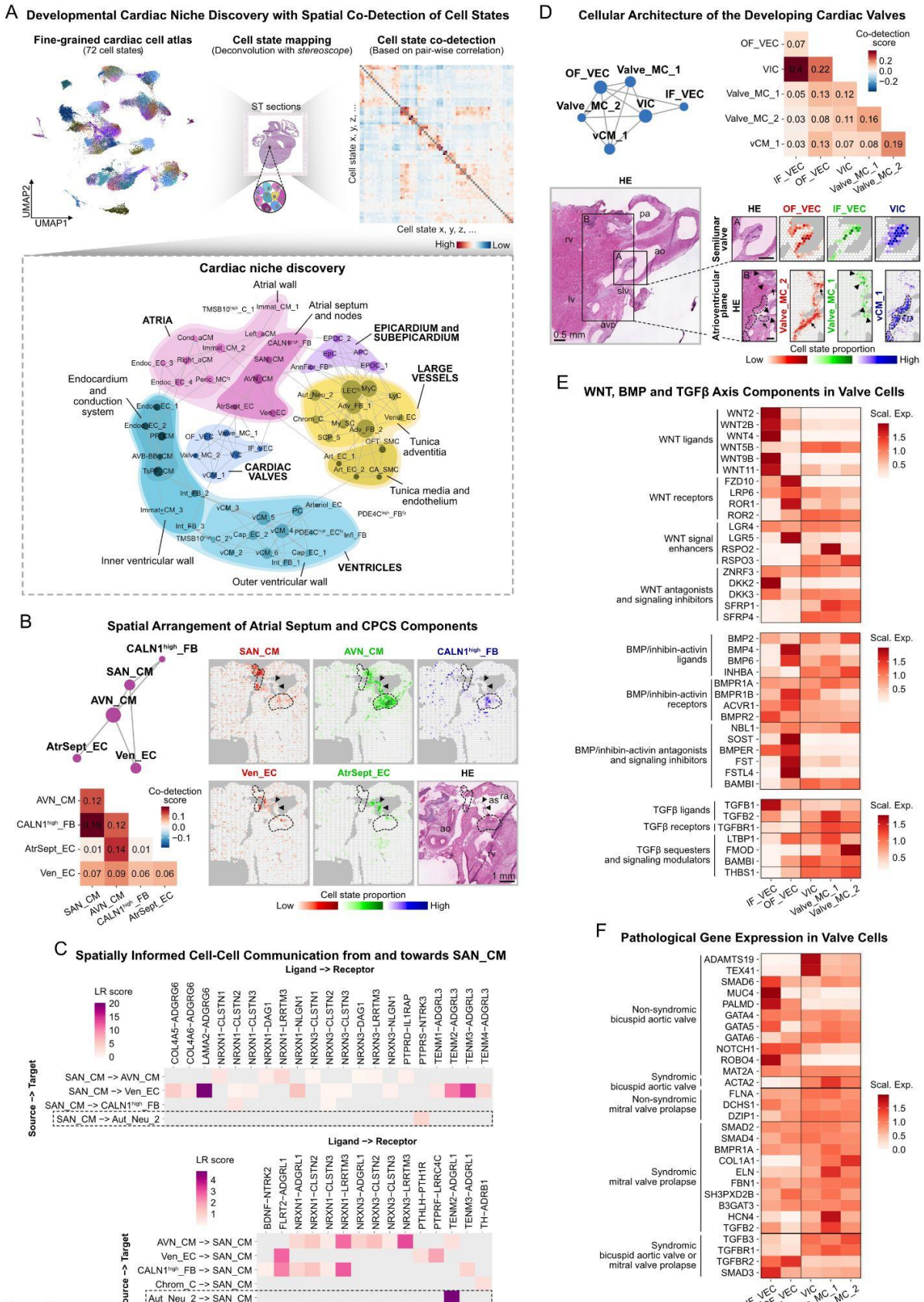
A
Developmental Cardiac Niche Discovery with Spatial Co-Detection of Cell States
Fine-grained cardiac cell atlas
(72 cell states)
Cell state mapping
(Deconvolution with stereoscope)
Cell state co-detection
(Based on pair-wise correlation)
ST sections
UMAP2
UMAP1
Cell state x, y, z, ...
High
Low
Cardiac niche discovery
Atrial wall
Atrial septum and nodes
ATRIA
EPICARDIUM and SUBEPICARDIUM
LARGE VESSELS
Endocardium and conduction system
Tunica adventitia
CARDIAC VALVES
Tunica media and endothelium
Inner ventricular wall
VENTRICLES
Outer ventricular wall
B
Spatial Arrangement of Atrial Septum and CPCS Components
CALN1high_FB
SAN_CM
AVN_CM
AtrSept_EC
Ven_EC
HE
Co-detection score
Cell state proportion
Low
High
1 mm
C
Spatially Informed Cell-Cell Communication from and towards SAN_CM
Ligand -> Receptor
LR score
Source -> Target
SAN_CM -> AVN_CM
SAN_CM -> Ven_EC
SAN_CM -> CALN1high_FB
SAN_CM -> Aut_Neu_2
AVN_CM -> SAN_CM
Ven_EC -> SAN_CM
CALN1high_FB -> SAN_CM
Chrom_C -> SAN_CM
Aut_Neu_2 -> SAN_CM
D
Cellular Architecture of the Developing Cardiac Valves
OF_VEC
Valve_MC_1
IF_VEC
Valve_MC_2
VIC
vCM_1
Co-detection score
HE
Semilunar valve
Atrioventricular plane
Cell state proportion
Low
High
0.5 mm
E
WNT, BMP and TGFβ Axis Components in Valve Cells
WNT ligands
WNT receptors
WNT signal enhancers
WNT antagonists and signaling inhibitors
BMP/inhibin-activin ligands
BMP/inhibin-activin receptors
BMP/inhibin-activin antagonists and signaling inhibitors
TGFβ ligands
TGFβ receptors
TGFβ sequesters and signaling modulators
Scal. Exp.
F
Pathological Gene Expression in Valve Cells
Non-syndromic bicuspid aortic valve
Syndromic bicuspid aortic valve
Non-syndromic mitral valve prolapse
Syndromic mitral valve prolapse
Syndromic bicuspid aortic valve or mitral valve prolapse
Scal. Exp.

Figure 7

**Fig. 7. Spatially Informed Analysis of Developmental Cardiac Niches. A.** Schematic representation of niche discovery strategy, using spatial mapping results of 72 fine-grained cell states for co-detection analysis (upper). Network graph of cardiac niches generated based on positive co-detection scores, with grey lines representing spatial association, and circle size reflecting the number of co-detected cell states (lower). **B.** Atrial septum and CPCS niche network graph and corresponding co-detection scores (left). Spatial mapping of SAN_CMs (red), AVN_CMs (green), CALN1$^{high}$_FBs (blue) (upper right), Ven_ECs (red) and AtrSept_ECs (green) (lower right), outlining the atrial septum (arrowheads) and nodal tissue (dashed lines) in a 11 pcw heart section. Scale bar represents 1 mm. **C.** Spatially informed cell-cell communication analysis between SAN_CMs, its cellular neighborhood and Chrom_Cs, highlighting ligand-receptor interactions included in a recently published neural-GPCR module of CellPhoneDB[51], differentially expressed in the analyzed cell states within their respective subsets. **D.** Cardiac valve niche network graph and corresponding co-detection scores (left). Spatial mapping of OF_VECs (red), IF_VECs (green), VICs (blue) (right, ROI A), and Valve_MC_2 (red), Valve_MC_1 (green) and vCM_1 (blue) (right, ROI B) cells, highlighting dominant cellular components of semilunar valves (ROI A) and neighboring atrioventricular plane regions (ROI B), respectively, in a 12 pcw section. Scale bars represent 0.5 mm. **E.** Heatmap representing per-gene scaled expression of WNT, BMP and TGFβ signaling molecules in valvular endothelial and mesenchymal cell states. **F.** Heatmap displaying per-gene scaled expression of bicuspid aortic valve disease- and mitral valve prolapse-related genes in valvular endothelial and mesenchymal cell states. In panel B-C: rv–right ventricle, lv–left ventricle, ra–right atrium, ao–aorta, pa–pulmonary artery, avp–atrioventricular plane, slv–semilunar valve, as–atrial septum, HE–hematoxylin-eosin.

670 **DISCUSSION**

671 The majority of congenital, as well as several acquired heart diseases trace their origins to early
672 development, highlighting the importance of this period in defining a healthy cardiac architecture.
673 Exploring concurrent spatiotemporal cellular and molecular patterns can provide cues for the
674 pathomechanisms, and thus potential therapeutic targets, in these conditions. Several human cardiac
675 single-cell atlases were published in recent years, characterizing the cellular composition of developing,
676 healthy and diseased adult hearts[23,91,92]. While representing invaluable resources about the cellular
677 complexity of cardiogenesis, biological interpretation of the developmental datasets is often challenging
678 due to their limited size or preselection of cell types of interest. Importantly, many of these approaches
679 overlook the spatial context of the investigated cells, which holds key information during organ
680 development. The possibility of combining single-cell analysis with unbiased, transcriptome-wide spatial
681 gene expression information opened new horizons in understanding cardiac architecture[51].

682 Our current work, built on the integrated analysis of single-cell and spatial transcriptomic datasets,
683 presents the first comprehensive spatiotemporal atlas of heart development in the 1$^{st}$ trimester. We
684 demonstrate that, beyond independent exploration of regional expressional patterns, this approach also
685 provides a basis for highly refined dissection of cell state heterogeneity, even in the heart's minor structural
686 or functional components. Accordingly, we performed detailed molecular characterization of specialized
687 cardiomyocytes in the developing cardiac pacemaker-conduction system, highlighting their distinct
688 electrophysiological properties and close spatial and functional association with specialized fibroblast cell
689 states in the nodes, endocardial cells in the ventricular conduction system, and neurons in the developing
690 autonomic innervation. Importantly, we present a resident neuroendocrine chromaffin cell population in
691 the fetal human heart, with implications on organ-level cardiac response to hypoxia, and highlighting them
692 as the potential cellular origin of the rare cases of cardiac pheochromocytoma. By resolving cellular
693 complexity in cardiac valves, we identified several mesenchymal and endothelial populations in this
694 location, including ectomesenchymal derivatives of the neural crest, and distinct endothelial cell states on
695 opposite sides of the valves from as early on as the 6$^{th}$ postconceptional week. We also explored the
696 expression patterns of major signaling network components involved in valvulogenesis, reflecting flow-
697 related transcriptomic differences, and highlighting endothelial cells on the ventricular side and valve
698 interstitial cells as main cellular targets in non-syndromic bicuspid aortic valve disease. Furthermore, we
699 identified a separate endocardial cushion-related population in the atrial septum with strong enrichment

700 of the transcription factor *LEF1* and *MSX1*, lending support for a potential causative role of these gene in
701 the development of atrial septal defects. The strong and temporally increasing enrichment of genes
702 involved in endothelial-to-mesenchymal transition in this cell state is especially intriguing, considering
703 the limited extension of the mesenchymal cap on the developing atrial septum, and the lack of persisting
704 mesenchymal components in this structure, unlike in the cardiac valves. In lack of characteristic marker
705 genes, we also leveraged spatial predictions on cell state distributions to untangle the diversity of non-
706 mural cardiac fibroblast and mesenchymal cells in the developing heart, identifying a range of cell states
707 associated with the annulus fibrosus, vessel adventitia, subepicardium, and myocardial interstitium.
708 Moreover, we identified a fetal cardiac cell state resembling fibro-adipogenic progenitor (FAP)
709 characteristics, which may constitute the developmental origin of cells responsible for fibro-fatty tissue
710 transformation in arrhythmogenic right ventricular cardiomyopathy. Finally, we delineated the cellular
711 composition of fine-grained cardiac niches in the developing heart, allowing for more nuanced and
712 spatially informed interrogation of cell-cell communication and developmental trajectories, before
713 bioinformatic tools, directly grounded in spatial transcriptomics data analysis, become established.

714 While this work captures the developing human cardiac architecture with unprecedented cellular and
715 spatiotemporal resolution, it is intrinsically limited by the analyzed timeframe and size of the collected
716 datasets. In fact, many genes implicated in the development of congenital heart diseases are active already
717 during the first two weeks of cardiogenesis, which are not covered by our analysis. A larger sample size
718 would allow for more robust interrogation of temporal gene expression changes even in less abundant cell
719 states and could provide means to corroborate or even further refine cell state annotations presented in our
720 work. Furthermore, balanced sampling of structural cardiac components for spatial transcriptomics
721 analysis, especially in the case of morphologically not discernible structures like the nodal tissue, is
722 challenging, which, however, can be mitigated by increasing the number of sections included in the
723 analysis. Finally, the presented cellulo-architectural framework based on transcriptomics analysis could
724 be enriched by a multiomics approach, mapping the proteomic, metabolomic, and chromatin accessibility
725 landscape of the developing heart.

726 Further analysis of the presented dataset has the potential to furnish novel insight into other relevant
727 questions of early cardiogenesis, not covered by our current study. The dataset can also be utilized as a
728 spatiotemporal reference to assess expression patterns of CHD candidate genes in the 1$^{st}$ trimester, and for
729 iPSC-derived cardiac cell and tissue therapies, often resembling embryonic phenotypes. In conclusion,

730 our work underscores the vast and yet underexploited possibilities of spatially targeted molecular analysis
731 within cardiac research.

732 **METHODS**

733 **Collection of Human Developmental Heart Tissue Samples**

734 All heart specimens included in this study were collected from elective medical abortions at the
735 Department of Obstetrics and Gynecology at Danderyd Hospital and Karolinska Huddinge Hospital in
736 Stockholm, Sweden. All patients were over 18 years old and donated tissue with written informed consent,
737 after receiving both oral and written information about the research project, and the possibility of retracting
738 their consent at any time, including later destruction of the donated tissue. Following collection, the
739 specimens were transferred from the clinic to the dissection laboratory. Heart tissue samples were then
740 swiftly dissected under sterile conditions within 2 hours post-abortion. In total, 36 human developmental
741 hearts between the age of 5.5 and 14 postconceptional weeks (pcw) were included in this study. The
742 embryonal/fetal age was determined using clinical data (ultrasound and last menstrual period), anatomical
743 landmarks and actual crown-rump-length. Both sexes were present in the full dataset, specifically 17 hearts
744 were from female and 14 from male donors, while information on sex for the 5 hearts used for *in situ*
745 sequencing and immunofluorescence experiments was not obtained. The study was performed with
746 approval of the Swedish Ethical Review Authority and the National Board of Health and Welfare, under
747 the ethical permit number 2018/769-31.

748 **Sample Preparation for Spatial Methods**

749 In total, 21 collected heart samples were embedded in Tissue-Tek O.C.T., snap-frozen, and stored at -80
750 °C. Samples were cryosectioned at 10 µm thickness. Sections from 16 hearts were placed on Visium Gene
751 Expression glass slides, while sections from 5 other hearts were placed on Superfrost glass slides for *in*
752 *situ* sequencing and immunohistochemistry.

753 **Visium Spatial Gene Expression Library Preparation and Sequencing**

754 Spatial gene expression libraries were generated using the 10x Genomics Visium Gene Expression kit,
755 according to the manufacturer's protocol[93]. A minimum of two consecutive tissue sections were included
756 in the analysis as technical replicates for all but one heart sample, where replicates had to be excluded

757 from downstream analysis due to experimental deficiencies. Tissue images were taken at 20x
758 magnification using the Metafer Slide Scanning platform (Microscope: AxioImager.Z2 with ScopeLED
759 Illumination, Zeiss; Camera: CoolCube 4m, MetaSystems; Objective: Plan-Apochromat 20X/0.80 M27,
760 Zeiss; Software: Metafer5). The permeabilization time was adjusted to 20 minutes. Raw images were
761 stitched with VSlide software (MetaSystems). In total, 38 Visium libraries were prepared from 16 hearts.
762 Libraries were sequenced by using Nextseq2000 (Illumina), where length of read 1 was 28 bp and read 2
763 was 120 bp long.

764 **Processing and Analysis of Visium Spatial Gene Expression Data**

765 Sequenced libraries were processed using Space Ranger (v.1.2.1; 10x Genomics). Reads were aligned to
766 built-in human reference genome (GRCh38 v.2020-A, Ensembl 98). Further processing and data analysis
767 of the spatial data was performed in R Statistical Software (v.4.0.5)[94] using STUtility (v.0.1.0)[95] and Seurat
768 (v.4.1.1)[96] packages. The created count matrix was filtered for MALAT1, ribosomal, mitochondrial, and
769 hemoglobin genes. Spots with fewer than 200 genes were removed from downstream analysis. The
770 processed data was described with a median of nFeature_Spatial and nCount_Spatial of 2,191.5 and 4,179,
771 respectively. Each tissue section was normalized separately using SCTransform function from the Seurat
772 package. Sections with at least 3 heart chambers present were selected for clustering. In the following
773 steps, principal component analysis (PCA) and sample integration using Harmony (v.1.0)[97] was
774 performed. Unsupervised clustering of spots was performed using the shared nearest neighbor (SNN)
775 algorithm from the Seurat package. Uniform manifold approximation and projection (UMAP) was used
776 for cluster visualization. Temporal evolution of spatial clusters was analyzed by embedding the original
777 UMAP with three age groups (age 1: 6-7 pcw; age 2: 8-9 pcw; age 3: 10-12 pcw). Downsampling in age
778 groups 2 and 3 was performed to equalize the spot numbers across embeddings (n = 2,649).
779 FindAllMarkers() function from Seurat package (logfc.threshold = 0.5, only.pos = TRUE, min.pct. = 0.01)
780 was applied to identify differentially expressed genes (DEGs) between clusters. Subsequently, all clusters
781 were manually annotated. Spatial feature plots were generated with the STUtility package.

782 In addition to standard clustering, region segmentation was performed on the same subset of sections using
783 the R tool Banksy (v.1.0.0)[41]. This spatially-aware clustering enables deciphering neighborhoods using
784 both the transcription information of a spot and its neighbors. The hyperparameter k was set to 6 to select
785 the first layer of direct surrounding Visium spots. The second hyperparameter, lambda, was set to 0.8 to

786 focus the algorithm to focus on region segmentation, as it weighs the importance of the spatial component
787 for the clustering. Banksy neighborhood-augmented feature space's clustering was performed with the
788 default Leiden algorithm at a resolution of 0.9. Resulting regions were transferred to the existing object
789 for exploration and visualization.

790 Non-negative matrix factorisation (NMF) was performed jointly using the singlet package (v.0.99.36)[98]
791 in R implemented in the semla toolkit on the entire Visium dataset. The parameter k was manually fixed
792 to 20, resulting in 20 shared factors across the dataset. This widely used method in the single-cell and
793 spatial omics field decomposes data variability into gene modules that covariate in a latent space. Each
794 factor consists of all the initial variable features ranked by order of influence in the factor-forming feature
795 loadings.

796 Hematoxylin-eosin micrographs of the analyzed tissue sections were included in the figures after linear
797 adjustments of intensity and contrast, performed in Affinity Designer. In composite figures with
798 micrographs of more than one tissue section, orientation of the images was adjusted according to the
799 anatomical position (left-right, superior-inferior) of the sampled cardiac structural components.

800 The original micrographs, quality metrics, sex and age distribution of the heart sections included in the
801 Visium dataset are displayed in Extended Figure 8A-D. Batch effects in the data were visually assessed
802 in the section selection used for clustering analysis, by embedding the UMAP with the individual samples,
803 either in an integrated or in an age-resolved manner (3 age groups) (Ext. Fig. 10A-B). Furthermore, cluster
804 and region distributions were computed per section and represented as barcharts enabling an evaluation
805 of consistency between technical replicates (Ext. Fig. 11A-B). Similarly, coarse-grained cell type
806 proportions were computed per section for the entire dataset and visualized in barcharts (Ext. Fig. 11C).

807 ***In Situ* Sequencing**

808 To generate the *in situ* sequencing (ISS) datasets presented in the manuscript, a panel of 150 gene targets
809 was created, including known regulators of cardiogenesis, consensus markers of major cardiac cell types,
810 and highly enriched genes of clusters of interest (Ext. Tab. 1). For these genes, a total of 5 padlock probes
811 per gene were designed, following a pipeline described by Lee et al.[99]. Next, a direct RNA *in situ*
812 sequencing protocol[99] was applied to 9 tissue sections, corresponding to 6.5 (section_1-3), 8.5 (section_4),
813 9 (section_5-6) and 11.5 pcw (section_7-9) (Ext. Fig. 1e).

814 For ISS sequencing library preparation, the sections were thawed at RT for 5 minutes, washed with PBS,
815 and fixed in 3% paraformaldehyde for 5 minutes. The sections were then washed 3x in PBS, permeabilized
816 with a 0.1M HCl solution for 5 minutes, and washed 3x in PBS. Next, the sections were sequentially
817 dehydrated in a 70% and 100% ethanol bath for 2 minutes each. Secure-seal chambers (-SA50, 1-13mm
818 Diameter X 0.8mm Depth, 22mm X 25mm OD, 1.5mm Diameter Ports) were laid over each sample,
819 which were then rehydrated with 0.5% Tween-PBS, followed by a PBS wash. A padlock probe solution
820 (2x SSC, 10% formamide, 10 nM of each padlock probe) was added to the chambers for overnight
821 incubation in a humidified chamber at 37 °C. The sections were then washed 2x with a washing solution
822 (2x SSC, 10% formamide), and then 2x with 2x SSC. The sections were then incubated in a ligation mix
823 (1x T4 Rnl2 reaction buffer (NEB, B0239SVIAL), 0.05 µM RCA primer, 1 U/µl RiboProtect (BLIRT,
824 RT35), 1.0 U/µl T4 Rnl2 (NEB, M0239)) in a humidified chamber at 37 °C for 2 hours. The sections
825 where then washed 2x with PBS, and then incubated in a rolling circle amplification mix (1x phi29 buffer
826 (50mM Tris-HCL pH 8.3, 10mM MgCl2, 10mM (NH4)SO4), 5% glycerol, 0.25 mM dNTPs (BLIRT,
827 RP65), 0.2 µg/ml BSA and 1U/µl Φ29 polymerase (Monserate Biotech, 4002)) at 30 °C in a humidified
828 chamber overnight.

829 After washing the sections 3x with PBS and 2x with 2x SSC, fluorescent probes were hybridized to the
830 samples with incubation in a bridge probe mix (20% formamide, 2x SSC, 0.1 µM of each bridge probe)
831 for 30 minutes in a humidified chamber at RT. The sections were washed 2x with PBS and 2x with 2x
832 SSC, followed by hybridizing a detection oligo mix (20% formamide, 2x SSC, 0.5µM of each detection
833 oligo (conjugated with Atto425, AlexaFluor488, Cy3, Cy5, AlexaFluor750), 0.25 µM DAPI (Biotium,
834 S36936)) for 30 minutes in a humidified chamber at RT. Sections were washed 2x with PBS, then mounted
835 with SlowFade Gold Antifade Mountant (Thermo Scientific, S36936).

836 Cyclical imaging of the sections[99] was performed by stripping bridge probes and detection oligos after
837 each cycle with 3x washes in 100% formamide for 5 minutes each, followed by 5x washes in 2x SSC. A
838 new set of bridge probes were then hybridized in the same manner, and the process was repeated until all
839 5 cycles were imaged. Image acquisition was performed using a Leica epifluorescence microscope
840 (Microscope: DMi6000, Lumencor® SPECTRA X Light Engine, LMT200-HS automatic multi-slide
841 stage; Camera: sCMOS, 2048x2048 resolution, 16 bit; Objective: HC Plan-Apochromat 20X/0.80 air, and
842 Plan-Apochromat 40X/1.10 W CORR oil objectives; Filters: filter cubes 38HE, Chroma 89402 – ET –
843 391-32/479-33/554-24/638-31 Multi LED set, Chroma 89403 – ET – 436-28/506-21/578-24/730-40 Multi

844 LED set, and an external filter wheel DFT51011). Each region of interest (ROI) was marked and saved in
845 the Leica LASX software for repeated imaging. Each ROI was automatically subdivided into tiles, and a
846 z-stack with an interval of 0.5 µm was acquired for each tile in all the channels, with a 10% overlap
847 between each tile. The ROIs were saved as TIFF files with associated metadata.

848 To create the *in situ* sequencing maps[99] featured in this manuscript, the images obtained for each dataset
849 across cycles were orthogonally projected using maximum intensity projection with the aim of collapsing
850 the different z-planes into a single image per tile. Next, tiles from individual cycles were stitched, and
851 images from different cycles were aligned using ashlar, obtaining 5 large, aligned TIFF files for each
852 dataset, corresponding to the different imaging rounds. Due to computational considerations, images were
853 then retiled into smaller aligned images. A pre-trained CARE model was then applied to each of the retiled
854 images, resulting in a reduction of the point spread function and increasing signal to noise ratio. The output
855 was then converted to the SpaceTx format and spots were identified using the PerRoundMaxChannel
856 decoder, included in starfish. Every spot was given a quality score for each of the cycles, by normalizing
857 for the most intense channel. Using the quality scores from all rounds, two quality metrics were composed
858 for each spot: the mean quality score, defined as the mean of the qualities across cycles, and the minimum
859 quality score, which corresponds to the score of the round where the quality was the lowest. Using these
860 metrics, spots were filtered, retaining only the ones presenting a minimum quality score over 0.4 for
861 further analysis. Finally, using the identity and position of all the high-quality score spots decoded,
862 expression maps were assembled for each of the datasets.

863 For ISS panels included in the figures, visualization of selected target genes over the DAPI image of the
864 tissue section was performed using TissUUmaps[100], with high resolution capture of the image viewport
865 (zoom factor=8). Orientation of the images was adjusted according to the anatomical position (left-right,
866 superior-inferior) of the sampled cardiac structural components.

867 Consistency between technical replicates in the ISS dataset was evaluated based on agreement between
868 detected transcript numbers of individual targets, by calculating Pearson correlation coefficient between
869 paired sections (Ext. Fig. 11D).

870 **Indirect Immunofluorescence and Imaging**

871 After fixation with 4% paraformaldehyde (Thermo Scientific, 043368.9M) for 15 minutes, the heart
872 sections were washed 3x in PBS for 15 minutes. Then, the samples were incubated overnight at 4°C with
873 the following antibodies: anti-ARL13B (RRID:AB_3073658, ab136648, Abcam, 1:400), anti-PCNT
874 (RRID:AB_2160664, ab28144, Abcam, 1:800) and anti-PDE4C (RRID:AB_3094595, HPA054218, Atlas
875 Antibodies, 1:100). The sections were then blocked for 30 minutes in 1xTBS (Medicago, 097500100)
876 with 0.5% TSA blocking reagent (Perkin Elmer, FP1020) and Hoechst (Invitrogen, H3570, 2µg/mL).
877 Next, the samples were incubated for 90 minutes at RT with anti-mouse-IgG2a-Alexa647
878 (RRID:AB_2535810, A21241, Invitrogen, 1:800), anti-mouse-IgG1-Alexa555 (RRID:AB_2535769,
879 A21127, Invitrogen, 1:800) and anti-rabbit-A488 (RRID:AB_2576217, A11034, Invitrogen, 1:800)
880 secondary antibodies, diluted in the blocking buffer. After incubation, the slides were washed 3x with
881 TBS-Tween for 15 minutes. Coverslips (VWR, 631-0147) were mounted on the slides using Fluoroshield
882 mounting medium (Invitrogen, 00495802). Imaging was performed with a PhenoImager Fusion 2.0
883 scanner, using a 20x objective and a phenocycler fresh frozen filter set. Exposure times were 5 ms for
884 Hoechst (DAPI channel), 300 ms for Alexa488 (FITC channel), 250 ms for Alexa555 (ATTO550
885 channel), and 400 ms for Alexa647 (Cy5 channel). PhenoImager automated algorithm was used for the
886 selection of focal points.

887 The captured tiles were automatically stitched together by the software operating PhenoImager, which
888 outputs a whole-slide image in the QPTIFF format. The QPTIFF files were opened in QuPath[101]. A
889 rectangular ROI was selected that circumscribed the whole imaged tissue. The content of the ROI was
890 sent to an ImageJ distribution in QuPath (without changing scale or intensity values) and the image was
891 saved as a TIFF file. Next the TIFF file was opened in FIJI. Linear adjustments of intensity and contrast
892 were performed separately for each detection channel on the collected images. Individual zoom-in ROIs
893 were selected and the regions in the ROIs were duplicated and saved as png files for implementing them
894 into the figure. To show the whole section in the figure, the whole image was downscaled in FIJI to 25%
895 of the original size and exported as a png file for embedding into the figure.

896 **Sample Preparation for Single-Cell RNA Sequencing**

897 In total, 15 heart samples were analyzed by single-cell RNA sequencing. The specimens were cut into
898 smaller pieces and minced using a blade. The tissue was transferred into a 15 ml Falcon tube containing
899 an enzymatic solution of Collagenase II (200 U/ml, Worthington Biochemical, LS004174), DNase I (1

900 mg/ml, Worthington Biochemical, LK003170) in Earle's balanced salt solution (EBSS, Worthington
901 Biochemical, LK003188) which had been pre-oxygenated with 95% O2:5% CO2 on ice for 5-10 minutes.
902 Tubes were put in a water bath and the samples were digested at 37 °C with an incubation time ranging
903 from approximately 45 minutes to over 2.5 hours, depending on the age of the tissue (tissues from later
904 developmental stages required longer dissociation times). During the incubation, the cell suspension was
905 triturated and dissociated around every 25 minutes, using glass fire-polished Pasteur pipettes, with
906 gradually decreasing tip diameter for each round to enhance dissociation. The cell suspension was
907 manually inspected under the microscope to assess the level of digestion, followed by a filtering step using
908 a prewet 30 µm cell strainer (CellTrics, Sysmex) to remove debris, fibers and smaller undissociated
909 remains. A small volume of EBSS was added to the filtered suspension to dilute and inactivate the enzyme,
910 then cells were pelleted through centrifugation at 200 g for 5 minutes. If needed, gradient centrifugation
911 was performed to remove blood cells. For this step, the cell pellet was resuspended in a solution containing
912 900 µl EBSS, 100 µl albumin inhibitor solution (Ovomucoid protease inhibitor and bovine serum albumin,
913 OI-BSA, LK003182) reconstituted in EBSS, and 50 µl of DNase I (larger volumes with the same reagent
914 concentrations were used in case of higher cell numbers). The resuspended solution was carefully layered
915 on top of 3 ml albumin inhibitor solution in a 15 ml Falcon tube and gradient centrifugation was performed
916 at 70 g for 4 to 6 minutes. Then the supernatant was removed, and the cells were resuspended in a
917 minimum amount of EBSS, starting from 100 µl (or more in case of higher cell numbers). The cell
918 suspension was transferred to a 1.5 ml Eppendorf tube, pre-coated with 30 % BSA (A9576, Sigma-
919 Aldrich). If a few cellular clumps had formed, a small volume of BSA was added to the suspension
920 (starting with 0.3 % BSA of the total volume). Cells were counted on a hemocytometer (Bürker/Neubauer
921 chamber) and cell viability was assessed with Trypan blue (Gibco, 15250061). Cell concentrations were
922 adjusted to values optimal for the 10x Genomics Chromium analysis.

923 **Single-Cell RNA Sequencing of Human Embryonic and Fetal Heart Cells**

924 Single cells were captured using the droplet-based platform Chromium (10x Genomics), and the
925 Chromium Single Cell 3′ Reagent Kit v2 and v3. Due to a change in the chemistry suppliance of the kits,
926 5 out of 21 libraries were sampled with v2. Cell concentrations were adjusted to between 800-1200 cells/µl
927 where possible, for a target recovery of 5000 cells per library. Cells were loaded on the Chromium
928 controller and downstream procedures such as cDNA synthesis, library preparation and sequencing were
929 done according to the manufacturer's instructions (10x Genomics). Libraries were sequenced between

930 approximately 100,000 to 250,000 reads/cell on the Illumina NovaSeq platform, reaching a saturation
931 between 60 to 90%. All libraries were demultiplexed using Cell Ranger (cellranger mkfastq v.4.0.0; 10x
932 Genomics) and filtered through the index-hopping-filter tool (v.1.1.0) by 10x Genomics. STARSolo
933 (v.2.7.10a) was used to determine Unique Molecular Identifier (UMI) counts, with the following
934 parameters used:

935 --soloFeatures Gene Velocyto
936 --soloBarcodeReadLength 0
937 --soloType CB_UMI_Simple
938 --soloCellFilter EmptyDrops_CR %s 0.99 10 45000 90000 500 0.01 20000 0.01 10000
939 --soloCBmatchWLtype 1MM_multi_Nbase_pseudocounts
940 --soloUMIfiltering MultiGeneUMI_CR
941 --soloUMIdedup 1MM_CR
942 --clipAdapterType CellRanger4
943 --outFilterScoreMin 30

944 Reads were aligned using the GRCh38.p13 gencode V35 primary sequence assembly. To minimize the
945 loss of reads that occur when they map to more than one gene, we applied a read-filtering step with certain
946 criteria, which is described in detail, along with the retrieval of count matrices and read alignments, in
947 Braun et al.[102].

948 **Processing and Filtering of the Single-Cell RNA Sequencing Data**

949 Further processing and analysis of the scRNA-seq data was performed in R (v.4.3.1)[94], using the Seurat
950 toolkit (v.4.3.0.1)[96]. The data was jointly handled as one Seurat object, and an initial filtering step was
951 applied, removing cells with more than 30% mitochondrial transcript counts. Cells with less than 250
952 unique genes or less than 3% ribosomal protein-coding transcript content were also removed unless they
953 also had more than 10% hemoglobin gene expression. The latter step was included to keep red blood cells
954 for the subsequent doublet detection step. From the 107,673 initial cells imported, 101,104 cells remained
955 after the first filtering round.

956 Doublet detection was performed separately for each sequencing dataset using the DoubletFinder R
957 package (v.2.0.3)[103], with expected multiple rates defined according to 10x Genomics guidelines. The data
958 was then merged again, and a second filtering step was applied, removing expected doublets (4,568

959 doublets), as well as cells with more than 10% hemoglobin gene expression (19,742 red blood cells),
960 identifying 76,991 high-quality cells. Data was then scaled using the Seurat function ScaleData() based
961 on the top 4,000 most highly variable genes, regressing out the number of reads, number of unique genes,
962 percentage of ribosomal genes, percentage of mitochondrial genes, percentage of hemoglobin genes,
963 percentage of heat shock protein-related genes, as well as S and G2M scores. Dataset integration was
964 performed using the R package Harmony (v.0.1.1)[97], leveraging the top 50 principal components. The
965 processed data was described with a median of nFeature_RNA and nCount_RNA of 2,417 and 4,838,
966 respectively.

967 Quality metrics, sex and age distribution of the heart samples included in the single-cell RNA sequencing
968 dataset are displayed in Extended Figure 12A-B.

969 **Age Categorization for Single Cell Data Analysis**

970 To facilitate a temporal analysis of the single-cell RNA sequencing dataset, samples were classified into
971 four age groups: age 1 (5.5-6 pcw), age 2 (7-8 pcw), age 3 (9-11 pcw), and age 4 (12-14 pcw). This
972 categorization enabled a comprehensive examination of temporal trends within the data, providing insights
973 into developmental patterns across different developmental stages.

974 **Coarse-Grained Clustering and Analysis of the Single-Cell RNA Sequencing Data**

975 Coarse-grained clusters (referred to as HL, as in 'high level', in the code) were obtained using the Louvain
976 community detection algorithm on an SNN graph built from the harmony embedding (nearest neighbors
977 set to 20) with the resolution parameter set to 1.8. The UMAP embedding was computed from the harmony
978 embedding (top 50 components), with 10 neighbors and 100 epochs. To identify differentially expressed
979 genes and facilitate the computation, the clusters were downsampled to have a maximum of 150 cells, and
980 pair-wise comparison of each cluster against all other clusters was performed using the FindAllMarkers()
981 function from Seurat (max.cells.per.ident = 300, logfc.threshold = 0.1, min.pct. = 0.05). To maintain the
982 highest heterogeneity within each cluster, the x=150 cells per group were randomly picked with the R
983 function sample(colnames(data)[data$clusters_louvain_oi == x], size = sample_size[x]), without using
984 any QC condition. Further subclustering of the mixed coarse-grained cluster 18 was performed with the
985 same settings and principal components, except for using the 10 nearest neighbors and a resolution of
986 0.25, resulting in two distinct subclusters. The small coarse-grained cluster 35 was merged with the highly
987 similar cluster 4 for further analysis.

988 For temporal analysis of the coarse-grained cluster distribution, UMAP embedding was performed across
989 the four predetermined age groups. Downsampling in age groups 1, 2 and 4 was performed to equalize
990 the cell numbers across embeddings (n = 8,742).

991 The original coarse-grained clusters and related quality metrics are displayed in Ext. Fig. 12C-E. Coarse
992 grained cluster 6 and 34 marking red blood cells, and 19 and 27 featuring low quality cells were excluded
993 from downstream analysis (Ext. Fig. 12F). Batch effects in our data were visually assessed by embedding
994 the coarse-grained UMAP with individual samples, either in an integrated or in an age-resolved manner
995 (4 age groups) (Ext. Fig. 10A, C).

996 **Fine-Grained Clustering and Analysis of the Single-Cell RNA Sequencing Data**

997 To create fine-grained clusters (occasionally referred to as DL, as in 'deep level', in the code),
998 cardiomyocyte (referred to as CM in the code), endothelial (referred to as EN in the code), mesenchymal
999 cell-fibroblast (referred to as FB in the code), and innervation-related cell (referred to as IN in the code)
1000 subsets were all processed similarly. The subsetted data was again scaled, this time based on the top 3,000
1001 highly variable genes, and the same variables were regressed out as for the complete dataset. Again, the
1002 data was integrated using Harmony, based on the top 50 principal components for the specific subset.
1003 Clustering was based on the 30 nearest neighbors and calculated using Louvain community detection with
1004 a resolution of 1.35 for cardiomyocytes, 1.25 for endothelial cells, 1.5 for fibroblasts, and 1 for
1005 innervation-related cells. UMAPs were calculated based on the top 50 integrated principal components
1006 and 30 neighbors, using 100 epochs. Marker genes were identified using the FindAllMarkers() from
1007 Seurat, using the same settings as for the coarse-grained clusters. The pacemaker-conduction system-
1008 related cardiomyocyte clusters 4, 8, and 19 were further subclustered to increase granularity. For this
1009 purpose, Louvain community detection was applied to each of these clusters, calculated from the top 30
1010 nearest neighbors with a resolution of 0.5.

1011 Fine-grained cardiomyocyte clusters 11, 13, 15, 16, 20, 21, and 22, fine-grained endothelial clusters 4, 8,
1012 9, and 22, fine-grained mesenchymal cell-fibroblast clusters 10, 16, 21 and 22, and fine-grained
1013 innervation-related cluster 2, 5, 6, 9, 10, 14, 15, 16 and 18 were excluded from downstream analysis, on
1014 the basis of low quality metrics, potential doublet contamination, or lack of consensus marker expression
1015 of the relevant cell types. The original UMAPs of these cell subsets, consensus marker expression profile

1016 of original fine-grained clusters, and parameters used as basis for cluster exclusion are presented in
1017 Extended Figure 13A-E.

1018 **Spatial Mapping Using Cell State Deconvolution**

1019 The spatial mapping of single-cell transcriptomics data onto tissue sections included in the Visium dataset
1020 was achieved through probabilistic inference using *stereoscope* (v.0.3.1)[104], effectively addressing spatial
1021 heterogeneity. By assuming a negative binomial distribution, this model estimates the proportions of
1022 single-cell states at every spatial spot. This guided decomposition process was executed separately for
1023 coarse- and fine-grained annotations. In the coarse-grained iteration, with 31 clusters remaining after
1024 excluding poor-quality clusters and red blood cells, the dataset was downsampled to the 500 cells
1025 containing the highest number of features in each population. Then, the top 5,000 most variable genes
1026 from this subset were utilized. Similarly, low-quality clusters were excluded in the fine-grained iteration
1027 and the dataset was downsampled to the top 250 cells with the highest number of features for each of the
1028 72 remaining cell states. The top 5,000 most variable genes from this subset were employed for the
1029 analysis. The *stereoscope* analysis ran with a batch size of 2,048 and 50,000 epochs for parameter
1030 estimation and proportion inference steps in both the coarse- and fine-grained iteration. A complementary,
1031 strictly age-matched cell type mapping was performed using ST and coarse-grained sc-RNA-seq data of
1032 the same age window. After excluding single-cell data from hearts not matching the age range of the ST
1033 sections, deconvolution with *stereoscope* was executed for the 3 previously determined age groups (age
1034 1: 6-7.5 pcw; age 2: 8-9 pcw; age 3: 10-12 pcw) with 500 cells per population, the top 5,000 most variable
1035 genes, and unchanged *stereoscope* parameters.

1036 Spatial cell state prediction maps were generated using MapFeatures() from the semla package (v.1.1.6)[105].
1037 A max_cutoff parameter of 0.99 was applied to mitigate potential biases from outliers in coarse-grained
1038 clusters, while no max_cutoff was used for fine-grained clusters. In the figures, these maps were visualized
1039 alongside the corresponding intensity- and contrast-adjusted hematoxylin-eosin micrograph of the
1040 relevant tissue section.

1041 **Annotation of Spatial and Single-Cell Clusters**

1042 Annotation of the spatial clusters was performed manually, based on the relative enrichment of consensus
1043 markers of cell states with characteristic spatial distributions, and the relation between known anatomical
1044 landmarks and the observed localization of spatial clusters within the analyzed heart sections. For the

1045 coarse- and fine-grained single-cell clusters, a spatially-aware annotation strategy was utilized. Cell state
1046 identification was based on the hierarchy of three features: first, the relative enrichment of consensus cell
1047 type/state markers was considered, discerning major cell populations and minor cell states with known
1048 transcriptomic profiles. For further refinement, the deconvolution results of the integrated single-cell and
1049 spatial transcriptomics datasets were utilized, factoring in the predicted localization of the analyzed cell
1050 states. Finally, enrichment of gene signatures consistent with different biological states in relation to
1051 maturation, metabolism, or proliferation were considered, in case the previous two features alone did not
1052 sufficiently explain the distinct characteristics of the cluster. Where possible, cluster names were selected
1053 to match the conventional cell state nomenclature, while in other cases, they were formulated to reflect
1054 the distinguishing spatial or transcriptomic feature of the population in question. Fine-grained cell states
1055 with annotations identical to coarse-grained clusters are distinguished by fg (as in 'fine-grained')
1056 superscript.

1057 Dominant marker genes of single cell clusters were identified by sequential filtering of the top 40 DEGs
1058 by lowest p-values (p_val), top 20 DEGs with the highest percentage difference (pct.1-pct.2), and top 5 or
1059 10 DEGs with the highest average log2 fold change (avg. log2FC), which were then visualized by dot
1060 plots across the compared clusters.

1061 **Assessment of Ion Channel Profiles of Cardiac Pacemaker-Conduction System-Related Cell States**

1062 After differential gene expression analysis across all fine-grained cardiomyocyte clusters, a
1063 comprehensive list of ion channel-encoding DEGs ($p < 0.05$, avg. log2FC > 0), enriched in any of the
1064 fine-grained cardiomyocyte clusters, was extracted. Next, this list was filtered in parallel for genes
1065 expressed in more than 10% of cells (pct. exp. > 0.1) of the SAN_CM or AVN_CM clusters, or of the
1066 AVB-BB_CM, PF_CM or TsPF_CM clusters, respectively. In Fig. 3F, genes with higher average
1067 expression (avg. exp.) observed in SAN_CMs or AVN_CMs compared to the contractile atrial clusters
1068 Right_aCM, Left_aCM and Cond_aCM were included. In Suppl. Fig. 3F, genes with higher average
1069 expression (avg. exp.) observed in AVB-BB_CMs, PF_CMs or TsPF_CMs compared to the contractile
1070 ventricular cluster vCM_4 were included. The compiled gene lists were then assessed for biological
1071 relevance in the specification of the pacemaker-conductive phenotype.

1072 **Analysis of Cell State Co-Detection and Identification of Spatial Compartments and Cellular Niches**

1073 Spatial compartments and cellular niches were identified based on co-detection scores, obtained by
1074 calculating the commonly used Pearson correlation coefficients between the distribution of each fine-
1075 grained cell state pair, based on the spatial cell proportion predictions of the stereoscope analysis. The
1076 matrix of these in-pair calculated correlation scores, referred to as co-detection scores, served as a proxy
1077 for appreciating the level of spatial overlap between the fine-grained cell states despite the sparsity of the
1078 data, outlining groups of cell states with close spatial association. Co-detection scores in our dataset ranged
1079 between -0.25 and 0.55 (95th percentile = 0.10) in the age-resolved, and between -0.2 and 0.42 (95th
1080 percentile = 0.09) in the merged dataset. The co-detection matrices were further visualized on heatmaps
1081 using geom_tile() from ggplot2 (v.3.4.4)[106]. Spatially co-localised cell types were described with positive
1082 co-detection scores, while non-co-localised cell types were described with negative ones. Since 72 cell
1083 types were used for the deconvolution, inherently many proportions were close to zero, hence, the co-
1084 detection heatmap resulted in many scores around zero. Those indicate neither co-detection, nor non-co-
1085 detection. To capture niches clearly, a co-detection graph network was built, where co-detection scores
1086 above a manually selected arbitrary threshold of 0.07 were kept. All the other scores were set to 0 since
1087 we considered building graphs with negative values not meaningful. From the remaining co-detection
1088 matrix, we used graph_from_adjacency_matrix() function from the igraph (v.1.5.1)[107] package in R
1089 (weighted=TRUE, mode="undirected", diag=FALSE) which represents high co-detection scores by
1090 shorter edges between nodes (nodes appear closer in the graph) and degree() function from the igraph
1091 package in R to calculate the degree for each node influencing the size of the nodes (the more connections,
1092 the bigger the node). The graph was plotted using the plot() function from igraph package
1093 (vertex.size=deg*1.1) and other parameters left to default. In our case (less than 1000 vertices, and no
1094 other attributes), the network layout has been selected by default by the tool, resulting in the Fruchterman-
1095 Reingold algorithm. The resulting network (Figure 7A, lower panel) is useful for readability, where niches
1096 and compartments were manually annotated based on the cell states' spatial relation to known cardiac
1097 structural components. These steps were performed on the merged Visium dataset, as well as in an age-
1098 resolved manner (age 1: 6-7.5 pcw; age 2: 8-9 pcw; age 3: 10-12 pcw) to describe cellular spatial relations
1099 in a temporal context.

1100 Spatial association of manually selected niches was presented with a new in-house function CellCol.R, an
1101 adaptation of the MapFeatures() function built upon the package semla (v.1.1.6)[105], enabling simultaneous
1102 visualization of per-spot predicted cell type proportion of two or three cell states, overlaid onto the section

1103 of interest in the Visium dataset. Overlap of co-detected cell states was presented through a scaled color
1104 blending using blend_colors() function from colorjam (v.0.0.26.900)[108].

1105 **Cell-Cell Communication Analysis**

1106 Single-cell clusters in spatial proximity were selected for cell-cell communication (CCC) analysis.
1107 Intercellular communication between ligands (L) and receptors (R) was inferred using CellPhoneDB
1108 (v.2)[109] implementation through the tool provider Liana (v.0.1.13)[110] in R (v.4.3.1). A mean of the gene
1109 expression for known ligand and receptor pairs (LR) from the curated CellPhoneDB was calculated by
1110 randomly permuting (100 epochs) cell labels in the subset, generating a null distribution for each LR event
1111 between each cluster in the subset. The p-value of 0.05 was used as threshold for selecting significantly
1112 enriched LR between cell states having a mean expression of LR equal or higher than the mean of that
1113 specific LR event calculated with the null distribution. The default mode *magnitude* within the function
1114 rank_method() was used to order LR events based on expression level. A selected subset of the identified
1115 ligand-receptor interactions was finally visualized as a dot plot across the analyzed cell state pairs.

1116 Additionally, a subset of co-localised cell types selected from the niche network (SAN_CM and its direct
1117 neighbors and Chrom_C) accounted for the presence of the LR interaction described in a recently
1118 published, custom neural-GPCR module of CellPhoneDB (41586_2023_6311_MOESM5_ESM)[51]. After
1119 selecting the pairs of protein_name_a (ligands) and protein_name_b (receptors) present in the module,
1120 separate lists of ligands and receptors were generated for every cluster of interest from their differentially
1121 expressed genes. The cell-cell interactions were evaluated bi-directionally, SAN_CM (donor) to its
1122 neighbors (receivers) and from neighbors (donors) to SAN_CM (receiver), using the gene lists
1123 accordingly. The interactions were scored for each present LR pair by multiplying the average expression
1124 of the ligand and the receptor from their respective cell types with the AverageExpression(group.by =
1125 c("annot_dl")) function from the Seurat package. The results are represented as a heatmap where LR pairs
1126 present are colored according to their score, while a gray square is presented for LR pairs where the ligand
1127 or receptor was not enriched in the assessed cell states within their respective cellular subsets.

1128 Spatial LR interactions were visually presented in tissue sections for a selection of known LR pairs by
1129 calculating their geometric means per spot. The spatial LR interaction scores were plotted using an in-
1130 house adaptation of the MapFeatures() function from the semla package.

1131 **RNA Velocity and Pseudotime Analysis**

1132 RNA velocity for innervation-related fine-grained clusters was performed on the top 5,000 variable
1133 features calculated with filter_genes_dispersion() from scVelo (v.0.3.0)[111] in Python (v.3.8.17). PCA was
1134 performed with Scanpy (v.1.9.5)[112], followed by recomputing the neighboring graph
1135 (scanpy.pp.neighbors(), n_neighbors = 25). Velocity was plotted on the PCA embeddings after running
1136 scv.tl.velocity() and scv.tl.velocity_graph(). Pseudotime was calculated separately on the top 5,000
1137 variable features (highly_variable_genes()) with scFates (v.1.0.6)[113] in Python (v.3.11.6). PCA and
1138 clustering were performed similarly as for the RNA velocity analysis, resulting in the same embedding.
1139 Curves of the PCA were calculated using the ElPiGraph algorithm implemented in scFates
1140 (scFates.tl.curve()). Subsequently, pseudotime was calculated with scFates.tl.pseudotime() (n_jobs = 20,
1141 n_map=100), and both pseudotime and expression of markers were visualized on the PCA embedding
1142 (scanpy.pl.pca()).

1143 **Transcription Factor Inference Using Gene Regulatory Networks**

1144 Inference of transcription factor (TF) activity was performed using the Scenic pipeline (v.1.3.1)[114] in R
1145 (v.4.3.1). Gene regulatory networks (GRN) were generated based on co-expression across the single-cell
1146 RNA sequencing data with GENIE3 (v.1.22.0)[115], based on the overlap between the most variable features
1147 calculated during clustering of the dataset and the provided databases (hg19-500bp-upstream-
1148 10species.mc9nr.feather and hg19-tss-centered-10kb-7species.mc9nr.feather). Co-expression of the
1149 remaining TFs in the network were converted into regulons using
1150 runSCENIC_1_coexNetwork2modules(). The implemented AUCell from Scenic was used to score every
1151 regulon in each individual cell. Then, known TF-binding motifs were used to prune interactions from the
1152 GRN (regulatory modules or regulons). Relevant regulons were retrieved if their specific TF was
1153 differentially expressed (FindMarkers(), test.use = "wilcox", avg_log2FC > 0 and p_val < 5e-7) in the
1154 cluster of interest, compared to the other clusters of the specific group. Regulated genes in the dataset
1155 were similarly selected (FindMarkers(), test.use = "wilcox", top 1,000 based on p-value). The resulting
1156 network of regulatory TFs and their associated target genes was constructed as a network graph using the
1157 igraph package[107].

1158 The entire list of inferred transcription factors and target gene pairs, as well as differentially expressed
1159 transcription factors in the investigated cell states are presented in Extended Table 2-9.

1160 Regulon enrichment analysis in selected endothelial cell states was performed for each cell using
1161 AddModuleScore() from Seurat, scoring the average expression of the target genes of a TF compared to
1162 control sets of genes. The enrichments were visualized on violin plots for the three selected clusters in an
1163 age-resolved manner, where age groups 3 and 4 were merged (creating an age group representing 9-14
1164 pcw) in order to decrease the difference in cell numbers between the compared populations.

1165 **Pathological gene sets enrichment analysis**

1166 Known sets of gene markers associated with cardiovascular pathologies with high level of evidence (green
1167 marking) were retrieved from the PanelApp from Genomics England database
1168 (https://panelapp.genomicsengland.co.uk/) for gene sets enrichment analysis (GSEA) (panels:
1169 Arrhythmogenic right ventricular cardiomyopathy (Version 3.11), Brugada syndrome and cardiac sodium
1170 channel disease (Version 3.10), Cardiac arrhythmias (Version 13.37), Catecholaminergic polymorphic VT
1171 (Version 4.6), Dilated and arrhythmogenic cardiomyopathy (Version 2.31), Dilated Cardiomyopathy and
1172 conduction defects (Version 1.94), Familial non syndromic congenital heart disease (Version 1.86),
1173 Hypertrophic cardiomyopathy (Version 4.13), Idiopathic ventricular fibrillation (Version 1.2), Left
1174 Ventricular Noncompaction Cardiomyopathy (Version 1.4), Long QT syndrome (Version 3.8), Paediatric
1175 or syndromic cardiomyopathy (Version 4.10), Primary lymphoedema (Version 3.11), Progressive cardiac
1176 conduction disease (Version 2.8), RASopathies (Version 1.81), Sudden death in young people (Version
1177 1.15), Thoracic aortic aneurysm or dissection (GMS) (Version 3.16)). Each set of genes was used to
1178 compute its respective enrichment in each cell of the dataset using AddModuleScore() from Seurat,
1179 scoring the average expression of the gene set compared to control sets of genes. The mean of the
1180 enrichment scores was computed per cluster for the coarse- and fine-grained annotation layers. The
1181 resulting mean values were visualized on heatmaps representing the gene set of interest across every
1182 cluster using geom_tile() from the ggplot2 package.

1183 **Calculation of Single Cell Cluster Proportions**

1184 The relative sizes of coarse-grained clusters, as well as the fine-grained cluster representing FAPs, were
1185 assessed based on the ratio of cells in the cluster of interest, compared to the total number of cells in the
1186 relevant subset, and visualized with bar graphs in Microsoft Excel. The total number of cells in coarse-
1187 and fine-grained single cell clusters is displayed in Extended Table 10-11.

1188 **Data Availability**

All the data required to replicate the analysis, including cellranger output, spaceranger output, metadata, processed ISS data, extended figures and tables, as well as main RDS objects will be available on the Mendeley DATA repositories part 1 and part 2 upon publication. The processed data of Visium, scRNA-seq and ISS will be available for browsing gene expression, clusterings, and other analysis results on a viewer. The sensitive raw sequencing files for single-cell and spatial transcriptomics will be made available in the Federated European Genome-Phenome Archive upon publication and shared upon request. Due to the file size limitation, the corresponding author can provide access to the raw *in situ* sequencing dataset upon reasonable request. A list of abbreviations used in the manuscript, along with their expansions, is provided in Extended Table 12.

**Code Availability**

The code used in this study, together with the material and information required to reproduce the Docker and Conda environments, will be shared through GitHub upon publication. A permanent version of the code will be uploaded to Zenodo upon publication.

**Acknowledgements**

We acknowledge the services of the Developmental Tissue Bank of Karolinska Institute for providing prenatal tissue for this investigation. We thank Mariia Minaeva for her support with several bioinformatics tools used in this study, Quan H. Nguyen, Prakrithi Pavithra and Onkar Mulay for scientific discussions, Mattias Karlén for his help with illustrations, and Kim Thrane, Sami Sarenpää and Áron Kerényi for their useful suggestions on improving the text and figures of the manuscript. Finally, we thank the donors of tissue specimens whose invaluable contributions made this study possible.

**Funding**

This work was supported by grants from the Erling-Persson Foundation (HDCA to S.L., E.S., M.N., E.L., and J.L.), the Knut and Alice Wallenberg Foundation (2018.0220 to S.L., E.S., M.N., E.L., and J.L.), and the Science for Life Laboratory. I.A. was supported by ERC Synergy grant KILL-OR-DIFFERENTIATE 856529, Knut and Alice Wallenberg Foundation, Swedish Research Council, Bertil Hallsten Foundation, Paradifference Foundation, Cancerfonden, Hjarnfonden, and Austrian Science Fund (project grants and SFB consortia). O.B. was supported by the Center for Regenerative Therapies Dresden, the Swedish

Research Council, and the LeDucq foundation. J.N.H. was supported by an EMBO Postdoctoral Fellowship (ALTF 556-2022).

**Author Contributions**

Conceptualization: E.L., R.M., Ž.A., I.A., J. L.
Methodology: Ž.A., E.B., S.M.S., N.S., S.S., J.N.H.
Software: R.M., J.F., L.L., P.C.
Validation: S.M.S., N.S., S.S., J.N.H.
Formal analysis: E.L., R.M., Ž. A., J.F., L.L., M.V., P.C.
Investigation: Ž.A., E.B., S.M.S., N.S., S.S., J.N.H.
Resources: X.L., E.Lu., S.L., M.N., E.S., J.L.
Data curation: E.L., R.M., Ž.A., J.F., L.L., S.M.S., N.S., M.V., E.B.
Writing - original draft: E.L., R.M., Ž.A., J.F., S.M.S., N.S., S.S., J.N.H., E.B.
Writing - review and editing: E.L., R.M., Ž.A., J.L.
Visualization: E.L., R.M., Ž.A.
Supervision: E.L., O.B., C.S., E.Lu., S.L., M.N., E.S., I.A., J.L.
Project administration: E.L., R.M., Ž.A., J.L.
Funding acquisition: E.Lu., S.L., M.N., E.S., J.L.

**Declaration of Interests**

R.M. and J.L. are scientific consultants for 10x Genomics. S.L. is a paid scientific advisor to Moleculent, Combigene, and the Oslo University Center of Excellence in Immunotherapy. All other authors declare that they have no competing interests.

1237 **REFERENCES**


1238 1. Buijtendijk, M. F. J., Barnett, P. & van den Hoff, M. J. B. Development of the human heart. *Am. J.*
1239 *Med. Genet. C Semin. Med. Genet.* **184**, 7–22 (2020).
1240 2. Sylva, M., van den Hoff, M. J. B. & Moorman, A. F. M. Development of the human heart. *Am. J.*
1241 *Med. Genet. A* **164A**, 1347–1371 (2014).
1242 3. Houyel, L. & Meilhac, S. M. Heart Development and Congenital Structural Heart Defects. *Annu.*
1243 *Rev. Genomics Hum. Genet.* **22**, 257–284 (2021).
1244 4. Morton, S. U., Quiat, D., Seidman, J. G. & Seidman, C. E. Genomic frontiers in congenital heart
1245 disease. *Nat. Rev. Cardiol.* **19**, 26–42 (2022).
1246 5. Hikspoors, J. P. J. M. *et al.* A pictorial account of the human embryonic heart between 3.5 and 8
1247 weeks of development. *Commun Biol* **5**, 226 (2022).
1248 6. Esteban, I. *et al.* Pseudodynamic analysis of heart tube formation in the mouse reveals strong
1249 regional variability and early left–right asymmetry. *Nature Cardiovascular Research* **1**, 504–517
1250 (2022).
1251 7. Krishnan, A. *et al.* A detailed comparison of mouse and human cardiac development. *Pediatr. Res.*
1252 **76**, 500–507 (2014).
1253 8. Wittig, J. G. & Münsterberg, A. The Chicken as a Model Organism to Study Heart Development.
1254 *Cold Spring Harb. Perspect. Biol.* **12**, (2020).
1255 9. Martinsen, B. J. Reference guide to the stages of chick heart embryology. *Dev. Dyn.* **233**, 1217–
1256 1237 (2005).
1257 10. Xia, J. *et al.* Heart Development and Regeneration in Non-mammalian Model Organisms. *Front*
1258 *Cell Dev Biol* **8**, 595488 (2020).
1259 11. DeLaughter, D. M. *et al.* Single-Cell Resolution of Temporal Gene Expression during Heart

1260 Development. *Dev. Cell* **39**, 480–490 (2016).
1261 12. Li, G. *et al.* Transcriptomic Profiling Maps Anatomically Patterned Subpopulations among Single
1262 Embryonic Cardiac Cells. *Dev. Cell* **39**, 491–507 (2016).
1263 13. Lescroart, F. *et al.* Defining the earliest step of cardiovascular lineage segregation by single-cell
1264 RNA-seq. *Science* **359**, 1177–1181 (2018).
1265 14. Jia, G. *et al.* Single cell RNA-seq and ATAC-seq analysis of cardiac progenitor cell transition states
1266 and lineage settlement. *Nat. Commun.* **9**, 4877 (2018).
1267 15. Li, G. *et al.* Single cell expression analysis reveals anatomical and cell cycle-dependent
1268 transcriptional shifts during heart development. *Development* **146**, (2019).
1269 16. de Soysa, T. Y. *et al.* Single-cell analysis of cardiogenesis reveals basis for organ-level
1270 developmental defects. *Nature* **572**, 120–124 (2019).
1271 17. Tyser, R. C. V. *et al.* Characterization of a common progenitor pool of the epicardium and
1272 myocardium. *Science* **371**, (2021).
1273 18. Feng, W. *et al.* Single-cell transcriptomic analysis identifies murine heart molecular features at
1274 embryonic and neonatal stages. *Nat. Commun.* **13**, 7960 (2022).
1275 19. Huang, X. *et al.* Single-cell profiling of the developing embryonic heart in Drosophila.
1276 *Development* **150**, (2023).
1277 20. Mantri, M. *et al.* Spatiotemporal single-cell RNA sequencing of developing chicken hearts
1278 identifies interplay between cellular differentiation and morphogenesis. *Nat. Commun.* **12**, 1771
1279 (2021).
1280 21. Abu Nahia, K. *et al.* scRNA-seq reveals the diversity of the developing cardiac cell lineage and
1281 molecular players in heart rhythm regulation. *iScience* **27**, 110083 (2024).
1282 22. Paik, D. T., Cho, S., Tian, L., Chang, H. Y. & Wu, J. C. Single-cell RNA sequencing in

1283 cardiovascular development, disease and medicine. *Nat. Rev. Cardiol.* **17**, 457–473 (2020).
1284 23. Cui, Y. *et al.* Single-Cell Transcriptome Analysis Maps the Developmental Track of the Human
1285 Heart. *Cell Rep.* **26**, 1934–1950.e5 (2019).
1286 24. Suryawanshi, H. *et al.* Cell atlas of the foetal human heart and implications for autoimmune-
1287 mediated congenital heart block. *Cardiovasc. Res.* **116**, 1446–1457 (2020).
1288 25. Ameen, M. *et al.* Integrative single-cell analysis of cardiogenesis identifies developmental
1289 trajectories and non-coding mutations in congenital heart disease. *Cell* **185**, 4937–4953.e23 (2022).
1290 26. Knight-Schrijver, V. R. *et al.* A single-cell comparison of adult and fetal human epicardium defines
1291 the age-associated changes in epicardial activity. *Nat Cardiovasc Res* **1**, 1215–1229 (2022).
1292 27. Streef, T. J. *et al.* Single-cell analysis of human fetal epicardium reveals its cellular composition
1293 and identifies CRIP1 as a modulator of EMT. *Stem Cell Reports* **18**, 1421–1435 (2023).
1294 28. McCracken, I. R. *et al.* Mapping the developing human cardiac endothelium at single-cell
1295 resolution identifies MECOM as a regulator of arteriovenous gene expression. *Cardiovasc. Res.*
1296 **118**, 2960–2972 (2022).
1297 29. Sahara, M. *et al.* Population and Single-Cell Analysis of Human Cardiogenesis Reveals Unique
1298 LGR5 Ventricular Progenitors in Embryonic Outflow Tract. *Dev. Cell* **48**, 475–490.e7 (2019).
1299 30. Haniffa, M. *et al.* A roadmap for the Human Developmental Cell Atlas. *Nature* **597**, 196–205
1300 (2021).
1301 31. Long, X., Yuan, X. & Du, J. Single-cell and spatial transcriptomics: Advances in heart
1302 development and disease applications. *Comput. Struct. Biotechnol. J.* **21**, 2717–2731 (2023).
1303 32. Asp, M. *et al.* A Spatiotemporal Organ-Wide Gene Expression and Cell Atlas of the Developing
1304 Human Heart. *Cell* **179**, 1647–1660.e19 (2019).
1305 33. Farah, E. N. *et al.* Spatially organized cellular communities form the developing human heart.

1306 *Nature* (2024) doi:10.1038/s41586-024-07171-z.

1307 34. Chen, W. *et al.* Single-cell transcriptomic landscape of cardiac neural crest cell derivatives during
1308 development. *EMBO Rep.* **22**, e52389 (2021).

1309 35. Zhang, S.-S. *et al.* Iroquois homeobox gene 3 establishes fast conduction in the cardiac His-
1310 Purkinje network. *Proc. Natl. Acad. Sci. U. S. A.* **108**, 13576–13581 (2011).

1311 36. Seropian, I. M., Cassaglia, P., Miksztowicz, V. & González, G. E. Unraveling the role of galectin-3
1312 in cardiac pathology and physiology. *Front. Physiol.* **14**, 1304735 (2023).

1313 37. Spielmann, N. *et al.* Extensive identification of genes involved in congenital and structural heart
1314 disorders and cardiomyopathy. *Nature Cardiovascular Research* **1**, 157–173 (2022).

1315 38. Mizutani, H. *et al.* Overexpression of myosin phosphatase reduces Ca(2+) sensitivity of contraction
1316 and impairs cardiac function. *Circ. J.* **74**, 120–128 (2010).

1317 39. Nicin, L. *et al.* A human cell atlas of the pressure-induced hypertrophic heart. *Nature*
1318 *Cardiovascular Research* **1**, 174–185 (2022).

1319 40. Zhao, Y. *et al.* Hypoxia-induced signaling in the cardiovascular system: pathogenesis and
1320 therapeutic targets. *Signal Transduct Target Ther* **8**, 431 (2023).

1321 41. Singhal, V. *et al.* BANKSY unifies cell typing and tissue domain segmentation for scalable spatial
1322 omics data analysis. *Nat. Genet.* **56**, 431–441 (2024).

1323 42. Saunders, V., Dewing, J. M., Sanchez-Elsner, T. & Wilson, D. I. Expression and localisation of
1324 thymosin beta-4 in the developing human early fetal heart. *PLoS One* **13**, e0207248 (2018).

1325 43. Mill, P., Christensen, S. T. & Pedersen, L. B. Primary cilia as dynamic and diverse signalling hubs
1326 in development and disease. *Nat. Rev. Genet.* **24**, 421–441 (2023).

1327 44. Hansen, J. N. *et al.* A cAMP signalosome in primary cilia drives gene expression and kidney cyst
1328 formation. *EMBO Rep.* **23**, e54315 (2022).

1329 45. Ren, H. *et al.* Single-cell RNA sequencing of murine hearts for studying the development of the
1330 cardiac conduction system. *Sci Data* **10**, 577 (2023).
1331 46. Liang, D. *et al.* Cellular and molecular landscape of mammalian sinoatrial node revealed by single-
1332 cell RNA sequencing. *Nat. Commun.* **12**, 287 (2021).
1333 47. Goodyer, W. R. *et al.* Transcriptomic Profiling of the Developing Cardiac Conduction System at
1334 Single-Cell Resolution. *Circ. Res.* **125**, 379–397 (2019).
1335 48. van Eif, V. W. W., Stefanovic, S., Mohan, R. A. & Christoffels, V. M. Gradual differentiation and
1336 confinement of the cardiac conduction system as indicated by marker gene expression. *Biochim.*
1337 *Biophys. Acta Mol. Cell Res.* **1867**, 118509 (2020).
1338 49. Arduini, A. *et al.* Transcriptional profile of the rat cardiovascular system at single cell resolution.
1339 *bioRxiv* (2023) doi:10.1101/2023.11.14.567085.
1340 50. Bhattacharyya, S. *et al.* Using Gjd3-CreEGFP mice to examine atrioventricular node morphology
1341 and composition. *Sci. Rep.* **9**, 2106 (2019).
1342 51. Kanemaru, K. *et al.* Spatially resolved multiomics of human cardiac niches. *Nature* **619**, 801–810
1343 (2023).
1344 52. Sylvén, C. *et al.* High cardiomyocyte diversity in human early prenatal heart development. *iScience*
1345 **26**, 105857 (2023).
1346 53. Grant, A. O. Cardiac ion channels. *Circ. Arrhythm. Electrophysiol.* **2**, 185–194 (2009).
1347 54. Furushima, H. *et al.* Fetal atrioventricular block and postpartum augmentative QT prolongation in a
1348 patient with long-QT syndrome with KCNQ1 mutation. *J. Cardiovasc. Electrophysiol.* **21**, 1170–
1349 1173 (2010).
1350 55. Yang, Y. *et al.* Human KCNQ1 S140G mutation is associated with atrioventricular blocks. *Heart*
1351 *Rhythm* **4**, 611–618 (2007).

1352 56. Mohan, R. A. *et al.* Embryonic Tbx3+ cardiomyocytes form the mature cardiac conduction system
1353 by progressive fate restriction. *Development* **145**, (2018).
1354 57. Horsthuis, T. *et al.* Gene expression profiling of the forming atrioventricular node using a novel
1355 tbx3-based node-specific transgenic reporter. *Circ. Res.* **105**, 61–69 (2009).
1356 58. Hayter, E. A. *et al.* Distinct circadian mechanisms govern cardiac rhythms and susceptibility to
1357 arrhythmia. *Nat. Commun.* **12**, 2472 (2021).
1358 59. D'Souza, A. *et al.* A circadian clock in the sinus node mediates day-night rhythms in Hcn4 and
1359 heart rate. *Heart Rhythm* **18**, 801–810 (2021).
1360 60. Végh, A. M. D. *et al.* Part and Parcel of the Cardiac Autonomic Nerve System: Unravelling Its
1361 Cellular Building Blocks during Development. *J Cardiovasc Dev Dis* **3**, (2016).
1362 61. Takahashi, H. *et al.* Postsynaptic TrkC and presynaptic PTPσ function as a bidirectional excitatory
1363 synaptic organizing complex. *Neuron* **69**, 287–303 (2011).
1364 62. Vysokov, N. V. *et al.* Proteolytically released Lasso/teneurin-2 induces axonal attraction by
1365 interacting with latrophilin-1 on axonal growth cones. *Elife* **7**, (2018).
1366 63. Timón-Gómez, A. *et al.* Tissue-specific mitochondrial HIGD1C promotes oxygen sensitivity in
1367 carotid body chemoreceptors. *Elife* **11**, (2022).
1368 64. Faluk, M., Anastasopoulou, C. & Wadhwa, R. *Cardiac Chromaffin Cell Pheochromocytoma*.
1369 (StatPearls Publishing, 2023).
1370 65. Queen, R. *et al.* Spatial transcriptomics reveals novel genes during the remodelling of the
1371 embryonic human arterial valves. *PLoS Genet.* **19**, e1010777 (2023).
1372 66. Deepe, R. *et al.* The Mesenchymal Cap of the Atrial Septum and Atrial and Atrioventricular
1373 Septation. *J Cardiovasc Dev Dis* **7**, (2020).
1374 67. Dufour, W. *et al.* Monoallelic and biallelic variants in LEF1 are associated with a new syndrome

1375 combining ectodermal dysplasia and limb malformations caused by altered WNT signaling. *Genet.*
1376 *Med.* **24**, 1708–1721 (2022).
1377 68. Chen, Y.-H., Ishii, M., Sucov, H. M. & Maxson, R. E., Jr. Msx1 and Msx2 are required for
1378 endothelial-mesenchymal transformation of the atrioventricular cushions and patterning of the
1379 atrioventricular myocardium. *BMC Dev. Biol.* **8**, 75 (2008).
1380 69. Cordell, H. J. *et al.* Genome-wide association study of multiple congenital heart disease phenotypes
1381 identifies a susceptibility locus for atrial septal defect at chromosome 4p16. *Nat. Genet.* **45**, 822–
1382 824 (2013).
1383 70. Lahm, H. *et al.* Congenital heart disease risk loci identified by genome-wide association study in
1384 European patients. *J. Clin. Invest.* **131**, (2021).
1385 71. Ho, Y.-C. *et al.* PROX1 Inhibits PDGF-B Expression to Prevent Myxomatous Degeneration of
1386 Heart Valves. *Circ. Res.* **133**, 463–480 (2023).
1387 72. Goddard, L. M. *et al.* Hemodynamic Forces Sculpt Developing Heart Valves through a KLF2-
1388 WNT9B Paracrine Signaling Axis. *Dev. Cell* **43**, 274–289.e5 (2017).
1389 73. Ruter, D. L. *et al.* SMAD6 transduces endothelial cell flow responses required for blood vessel
1390 homeostasis. *Angiogenesis* **24**, 387–398 (2021).
1391 74. Tallquist, M. D. Developmental Pathways of Cardiac Fibroblasts. *Cold Spring Harb. Perspect.*
1392 *Biol.* **12**, (2020).
1393 75. Chen, Q. *et al.* Endothelial cells are progenitors of cardiac pericytes and vascular smooth muscle
1394 cells. *Nat. Commun.* **7**, 12422 (2016).
1395 76. Wei, S., Zhang, M., Zheng, Y. & Yan, P. ZBTB16 Overexpression Enhances White Adipogenesis
1396 and Induces Brown-Like Adipocyte Formation of Bovine White Intramuscular Preadipocytes. *Cell.*
1397 *Physiol. Biochem.* **48**, 2528–2538 (2018).

1398 77. Beak, J. Y., Kang, H. S., Kim, Y.-S. & Jetten, A. M. Krüppel-like zinc finger protein Glis3
1399 promotes osteoblast differentiation by regulating FGF18 expression. *J. Bone Miner. Res.* **22**, 1234–
1400 1244 (2007).
1401 78. Banerjee, S. S. *et al.* The Krüppel-like factor KLF2 inhibits peroxisome proliferator-activated
1402 receptor-gamma expression and adipogenesis. *J. Biol. Chem.* **278**, 2581–2584 (2003).
1403 79. Lombardi, R. *et al.* Cardiac Fibro-Adipocyte Progenitors Express Desmosome Proteins and
1404 Preferentially Differentiate to Adipocytes Upon Deletion of the Desmoplakin Gene. *Circ. Res.* **119**,
1405 41–54 (2016).
1406 80. Xu, T. *et al.* Compound and digenic heterozygosity contributes to arrhythmogenic right ventricular
1407 cardiomyopathy. *J. Am. Coll. Cardiol.* **55**, 587–597 (2010).
1408 81. Cahill, T. J. *et al.* Tissue-resident macrophages regulate lymphatic vessel growth and patterning in
1409 the developing heart. *Development* **148**, (2021).
1410 82. Single-cell RNA sequencing reveals the diversity and biology of valve cells in cardiac valve
1411 disease. *J. Cardiol.* **81**, 49–56 (2023).
1412 83. O'Donnell, A. & Yutzey, K. E. Mechanisms of heart valve development and disease. *Development*
1413 **147**, (2020).
1414 84. Huang, J. *et al.* KLF2 Mediates the Suppressive Effect of Laminar Flow on Vascular Calcification
1415 by Inhibiting Endothelial BMP/SMAD1/5 Signaling. *Circ. Res.* **129**, e87–e100 (2021).
1416 85. Albanese, I. *et al.* Role of Noncanonical Wnt Signaling Pathway in Human Aortic Valve
1417 Calcification. *Arterioscler. Thromb. Vasc. Biol.* **37**, 543–552 (2017).
1418 86. Dupuis, L. E. *et al.* Development of myotendinous-like junctions that anchor cardiac valves
1419 requires fibromodulin and lumican. *Dev. Dyn.* **245**, 1029–1042 (2016).
1420 87. Guauque-Olarte, S. *et al.* RNA expression profile of calcified bicuspid, tricuspid, and normal

1421 human aortic valves by RNA sequencing. *Physiol. Genomics* **48**, 749–761 (2016).
1422 88. Delwarde, C. *et al.* Genetics and pathophysiology of mitral valve prolapse. *Front Cardiovasc Med*
1423 **10**, 1077788 (2023).
1424 89. Gehlen, J. *et al.* Elucidation of the genetic causes of bicuspid aortic valve disease. *Cardiovasc. Res.*
1425 **119**, 857–866 (2023).
1426 90. Bravo-Jaimes, K. & Prakash, S. K. Genetics in bicuspid aortic valve disease: Where are we? *Prog.*
1427 *Cardiovasc. Dis.* **63**, 398–406 (2020).
1428 91. Miranda, A. M. A. *et al.* Single-cell transcriptomics for the assessment of cardiac disease. *Nat. Rev.*
1429 *Cardiol.* **20**, 289–308 (2023).
1430 92. Litviňuková, M. *et al.* Cells of the adult human heart. *Nature* **588**, 466–472 (2020).
1431 93. Genomics, 10x. *Visium Spatial Gene Expression Reagent Kits - User Guide*. (2022).
1432 94. Core Team, R. R. No title. https://apps.dtic.mil/sti/citations/AD1039033.
1433 95. Bergenstråhle, J., Larsson, L. & Lundeberg, J. Seamless integration of image and molecular
1434 analysis for spatial transcriptomics workflows. *BMC Genomics* **21**, 482 (2020).
1435 96. Hao, Y. *et al.* Integrated analysis of multimodal single-cell data. *Cell* **184**, 3573–3587.e29 (2021).
1436 97. Korsunsky, I. *et al.* Fast, sensitive and accurate integration of single-cell data with Harmony. *Nat.*
1437 *Methods* **16**, 1289–1296 (2019).
1438 98. DeBruine, Z. J., Andrew Pospisilik, J. & Triche, T. J. Fast and interpretable non-negative matrix
1439 factorization for atlas-scale single cell data. *bioRxiv* 2021.09.01.458620 (2024)
1440 doi:10.1101/2021.09.01.458620.
1441 99. Lee, H. *et al.* Open-source, high-throughput targeted in-situ transcriptomics for developmental
1442 biologists. *bioRxiv* 2023.10.10.561689 (2023) doi:10.1101/2023.10.10.561689.
1443 100. Pielawski, N. *et al.* TissUUmaps 3: Improvements in interactive visualization, exploration, and

1444 quality assessment of large-scale spatial omics data. *Heliyon* **9**, e15306 (2023).
1445 101. Bankhead, P. *et al.* QuPath: Open source software for digital pathology image analysis. *Sci. Rep.* **7**,
1446 16878 (2017).
1447 102. Braun, E. *et al.* Comprehensive cell atlas of the first-trimester developing human brain. *Science*
1448 **382**, eadf1226 (2023).
1449 103. McGinnis, C. S., Murrow, L. M. & Gartner, Z. J. DoubletFinder: Doublet Detection in Single-Cell
1450 RNA Sequencing Data Using Artificial Nearest Neighbors. *Cell Syst* **8**, 329–337.e4 (2019).
1451 104. Andersson, A. *et al.* Single-cell and spatial transcriptomics enables probabilistic inference of cell
1452 type topography. *Commun Biol* **3**, 565 (2020).
1453 105. Larsson, L., Franzén, L., Ståhl, P. L. & Lundeberg, J. Semla: a versatile toolkit for spatially
1454 resolved transcriptomics analysis and visualization. *Bioinformatics* **39**, (2023).
1455 106. Wickham, H. *ggplot2: Elegant Graphics for Data Analysis*. (Springer International Publishing,
1456 2016).
1457 107. Csardi, G. & Nepusz, T. The igraph software package for complex network research. *InterJournal*
1458 vol. Complex Systems 1695 Preprint at https://igraph.org (2006).
1459 108. Ward, J. M. colorjam: Jam Color manipulation functions. Preprint at
1460 http://github.com/jmw86069/colorjam (2023).
1461 109. Efremova, M., Vento-Tormo, M., Teichmann, S. A. & Vento-Tormo, R. CellPhoneDB: inferring
1462 cell-cell communication from combined expression of multi-subunit ligand-receptor complexes.
1463 *Nat. Protoc.* **15**, 1484–1506 (2020).
1464 110. Dimitrov, D. *et al.* Comparison of methods and resources for cell-cell communication inference
1465 from single-cell RNA-Seq data. *Nat. Commun.* **13**, 3224 (2022).
1466 111. Bergen, V., Lange, M., Peidli, S., Wolf, F. A. & Theis, F. J. Generalizing RNA velocity to transient

1467 cell states through dynamical modeling. *Nat. Biotechnol.* **38**, 1408–1414 (2020).

1468 112. Wolf, F. A., Angerer, P. & Theis, F. J. SCANPY: large-scale single-cell gene expression data

1469 analysis. *Genome Biol.* **19**, 15 (2018).

1470 113. Faure, L., Soldatov, R., Kharchenko, P. V. & Adameyko, I. scFates: a scalable python package for

1471 advanced pseudotime and bifurcation analysis from single-cell data. *Bioinformatics* **39**, (2023).

1472 114. Aibar, S. *et al.* SCENIC: single-cell regulatory network inference and clustering. *Nat. Methods* **14**,

1473 1083–1086 (2017).

1474 115. Huynh-Thu, V. A., Irrthum, A., Wehenkel, L. & Geurts, P. Inferring regulatory networks from

1475 expression data using tree-based methods. *PLoS One* **5**, (2010).

# Supplemental Data Information

## Supplemental Figure 1-7.

Supplemental Figure 1. Transcriptomic Profiles and Temporal Transitions of Cardiac Spatial Clusters
Supplemental Figure 2. Molecular Characteristics and Temporal Transitions of Major Cardiac Cell Populations
Supplemental Figure 3. Molecular and Spatial Features of Fine-Grained Cardiomyocyte States
Supplemental Figure 4. Transcriptomic and Spatial Characteristics of Fine-Grained Innervation-Related Cell States
Supplemental Figure 5. Molecular and Spatial Profiles of Fine-Grained Endothelial Cell States.
Supplemental Figure 6. Transcriptomic and Spatial Features of Fine-Grained Fibroblast and Mesenchymal Cell States
Supplemental Figure 7. Temporal Transitions and Analysis of Selected Developmental Cardiac Niches

## Supplemental Table 1-7.

Supplemental Table 1. List of Differentially Expressed Genes across Spatial Clusters
Supplemental Table 2. List of Differentially Expressed Genes across Coarse-Grained Single Cell Clusters
Supplemental Table 3. List of Differentially Expressed Genes across Fine-Grained Cardiomyocyte Clusters
Supplemental Table 4. List of Differentially Expressed Genes across Innervation-Related Cell Clusters
Supplemental Table 5. List of Differentially Expressed Genes across Fine-Grained Endothelial Cell Clusters
Supplemental Table 6. List of Differentially Expressed Genes across Fine-Grained Mesenchymal Cell-Fibroblast Clusters
Supplemental Table 7. Pearson Correlation-Based Co-Detection Scores for Fine-Grained Cell States

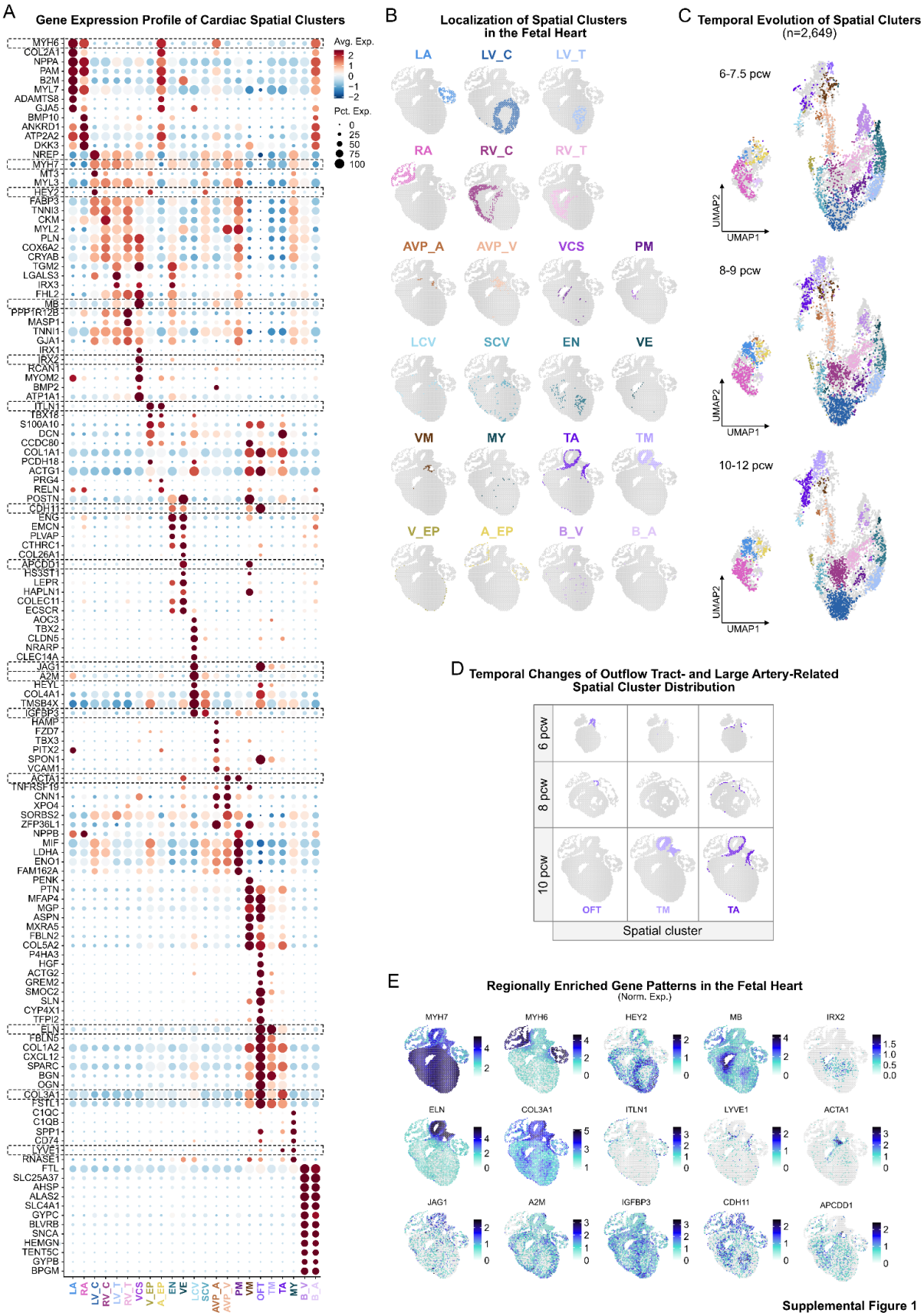


Supplemental Figure 1

**Suppl. Fig. 1. Transcriptomic Profiles and Temporal Transitions of Cardiac Spatial Clusters. A.** *Gene Expression Profile of Cardiac Spatial Clusters.* Dot plot depicts the top 5 DEGs (log2FC > 0, p_val < 0.05) in the 23 spatial clusters. Genes highlighted by dashed rectangles were selected for spatial expression plots included in Suppl. Fig. 1e. **B.** *Localization of Spatial Clusters in the Fetal Heart.* The spatial cluster corresponding to the early outflow tract (OFT) is absent in the 10 pcw heart section. **C.** *Temporal Evolution of Spatial Clusters.* UMAPs illustrate the distribution of barcoded tissue spots (n=2,649) between spatial clusters across three developmental age groups (6-7.5, 8-9, 10-12 pcw). **D.** *Temporal Evolution of Outflow Tract- and Large Artery-Related Spatial Clusters.* The spatial cluster corresponding to the early outflow tract (OFT) gradually disappears, while the one representing the tunica media of large arteries (TM) expands by 10 pcw. **E.** *Regionally Enriched Gene Patterns in the Fetal Heart.* Spatial feature plots of selected DEGs (log2FC > 0, p_val < 0.05) of spatial clusters are presented in a 10 pcw heart section.

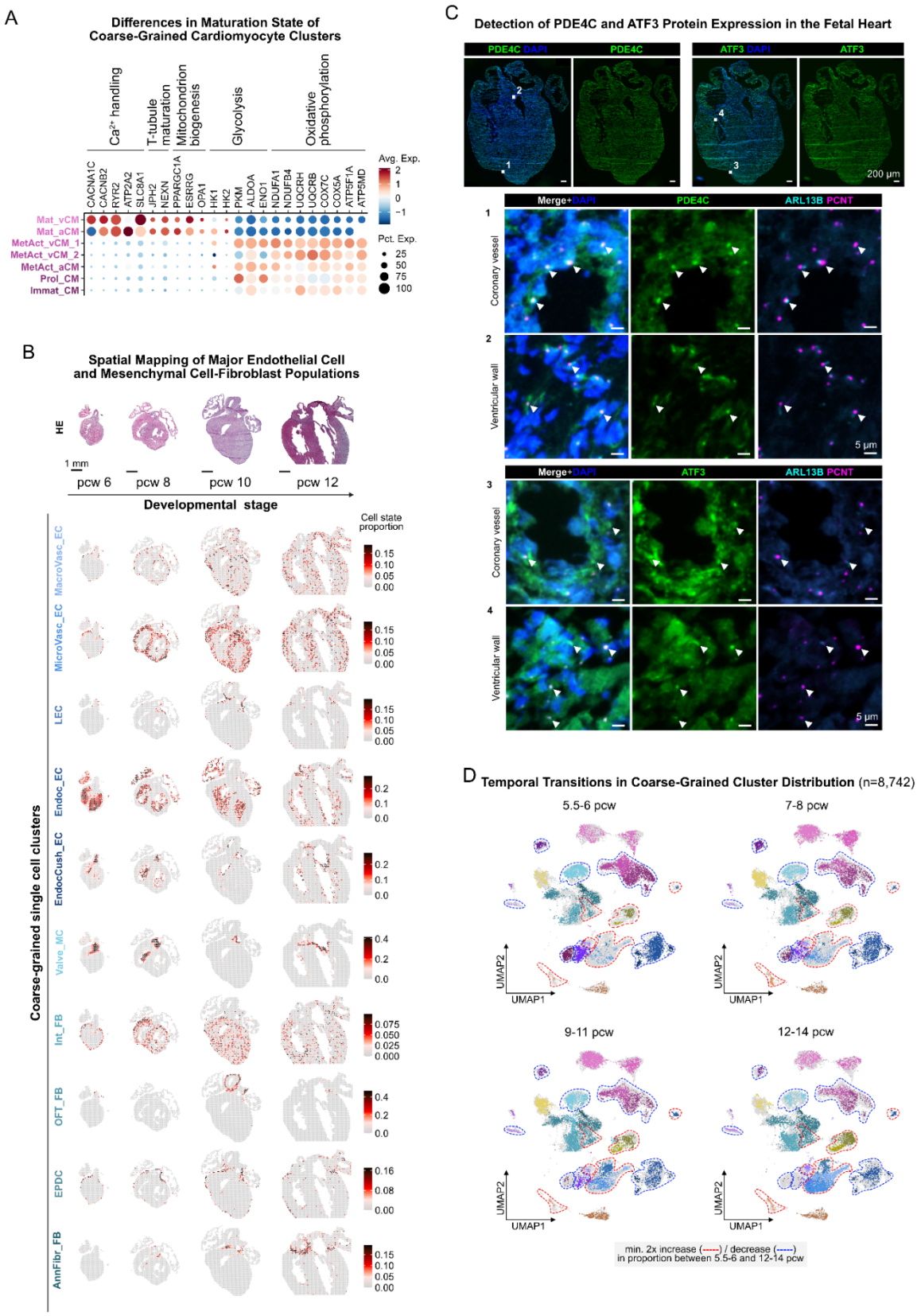


Supplemental Figure 2

**Suppl. Fig. 2. Molecular Characteristics and Temporal Transitions of Major Cardiac Cell Populations. A.** *Differences in Maturation State of Coarse-Grained Cardiomyocyte Clusters.* Dot plot shows relative expression of genes involved in electromechanical activation and bioenergetics of cardiomyocytes in coarse-grained cardiomyocyte clusters. **B.** *Spatial Mapping of Major Endothelial Cell and Mesenchymal Cell-Fibroblast Populations.* The upper panel shows hematoxylin-eosin (HE) micrographs of 6, 8, 10 and 12 pcw heart sections, while the lower panels depict predicted cell state proportions of selected coarse-grained clusters in the corresponding Visium tissue spots. Scale bar represents 1 mm. **C.** *Detection of PDE4C and ATF3 Protein Expression in the Fetal Heart.* Immunofluorescence demonstrates widespread expression of PDE4C (upper left, green) and ATF3 (upper right, green) proteins in a 9 pcw heart section, along with DAPI nuclear staining (blue). Scale bar represents 200 µm. The middle and bottom panels feature ROIs including a coronary artery (1, 3) and part of the ventricular myocardium (2, 4), highlighting subcellular enrichment of PDE4C (middle, green) and ATF3 (bottom, green) proteins in basal bodies, along with PCNT (basal bodies, purple), ARL13B (primary cilia, cyan), and DAPI (nuclei, blue) staining. Scale bar represents 5 µm. Arrowheads indicate PDE4C/ATF3$^{+}$-PCNT$^{+}$ basal body structures with connected ARL13B$^{+}$ primary cilia. **D.** *Temporal Transitions of Coarse-Grained Cluster Distribution.* UMAPs illustrate size changes of coarse-grained clusters across four developmental age groups (5.5-6, 7-8, 9-11, and 12-14 pcw, n=8,742). Dashed lines mark clusters with min. 2x increase (red) or decrease (blue) in proportion compared to the total number of cells between the 5.5-6 and 12-14 pcw age groups.

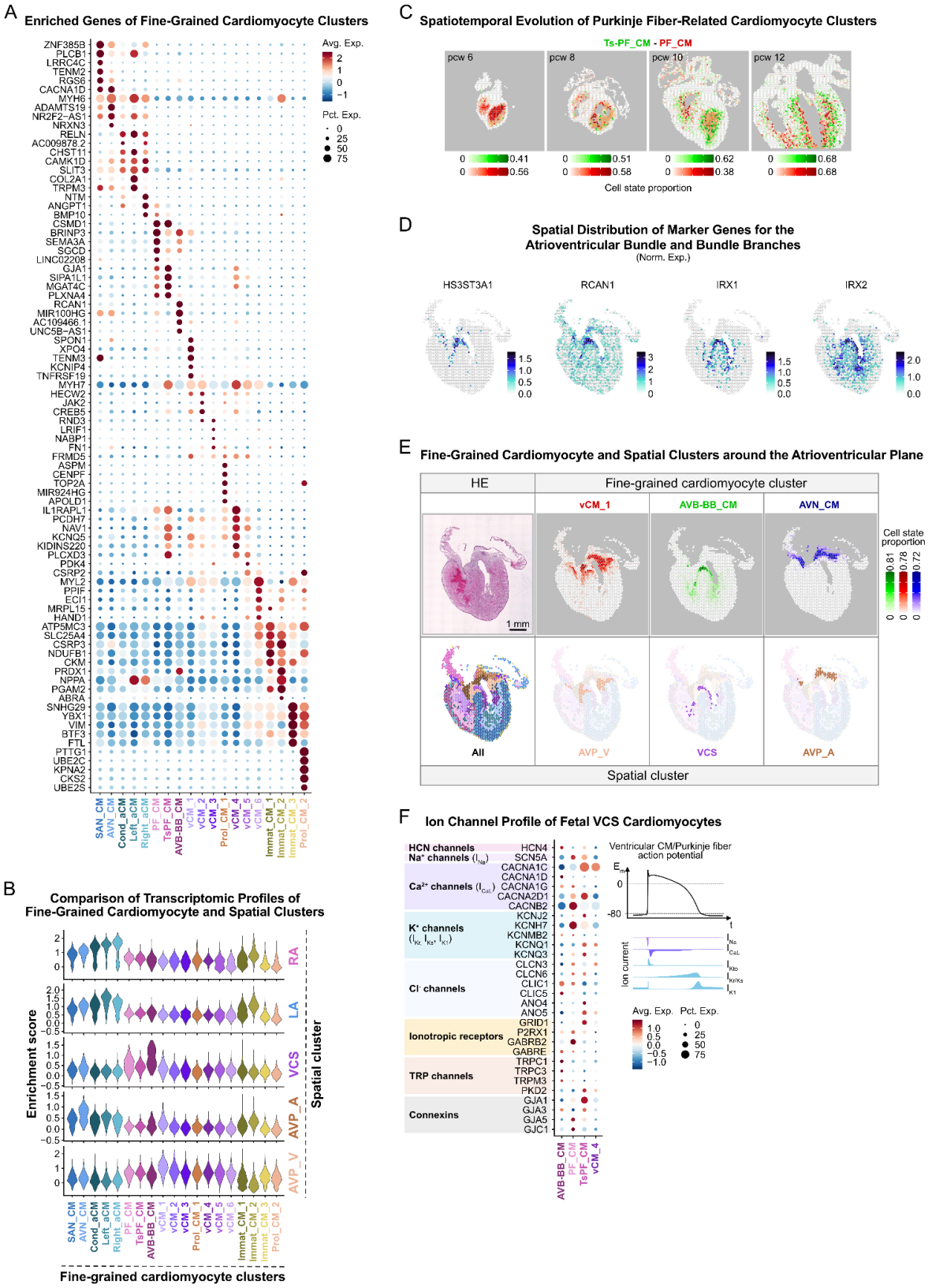




Supplemental Figure 3

**Suppl. Fig. 3. Molecular and Spatial Features of Fine-Grained Cardiomyocyte States. A.** *Enriched Genes of Fine-Grained Cardiomyocyte Clusters.* Dot plot depicts the top 5 DEGs (log2FC > 0, p_val < 0.05) between the 19 clusters. **B.** *Comparison of Transcriptomic Profiles of Fine-Grained Cardiomyocyte and Spatial Clusters.* Violin plots show gene signature enrichment of selected spatial clusters in fine-grained cardiomyocyte cell states. Spatial clusters: LA–left atrial myocardium; RA–right atrial myocardium; VCS–ventricular conduction system; AVP_A–atrioventricular plane, atrial side; AVP_V–atrioventricular plane, ventricular side. **C.** *Spatiotemporal Evolution of Purkinje Fiber-Related Cardiomyocyte Clusters*. Predicted spatial distribution of Ts-PF_CMs (green) and PF_CMs (red) in 6, 8, 10 and 12 pcw heart sections supports their gradual separation. **D.** *Spatial Distribution of Marker Genes for the Atrioventricular Bundle and Bundle Branches.* Spatial feature plots display selected DEGs (log2FC > 0, p_val < 0.05) of AVB-BB_CMs in a 10 pcw heart section. **E.** *Fine-Grained Cardiomyocyte and Spatial Clusters around the Atrioventricular Plane.* The upper panels display the hematoxylin-eosin (HE) micrograph of a 10 pcw heart section, along with the predicted spatial distribution of vCM_1 (red), AVB-BB_CM (green) and AVN_CM (blue) cells, while the lower panels illustrate the highly similar localization of the AVP_V, VCS and AVP_A spatial clusters, respectively. Scale bar represents 1 mm. **f.** *Ion Channel Profiles of Cardiomyocytes in the Fetal Ventricular Conduction System.* Dot plot displays the relative expression of selected ion channel genes across the AVB-BB_CM, PF_CM, Ts-PF_CM, and the contractile vCM_4 cell states. Major ion currents of the ventricular cardiomyocyte/Purkinje fiber action potential are illustrated in colors consistent with the ion channel plot.

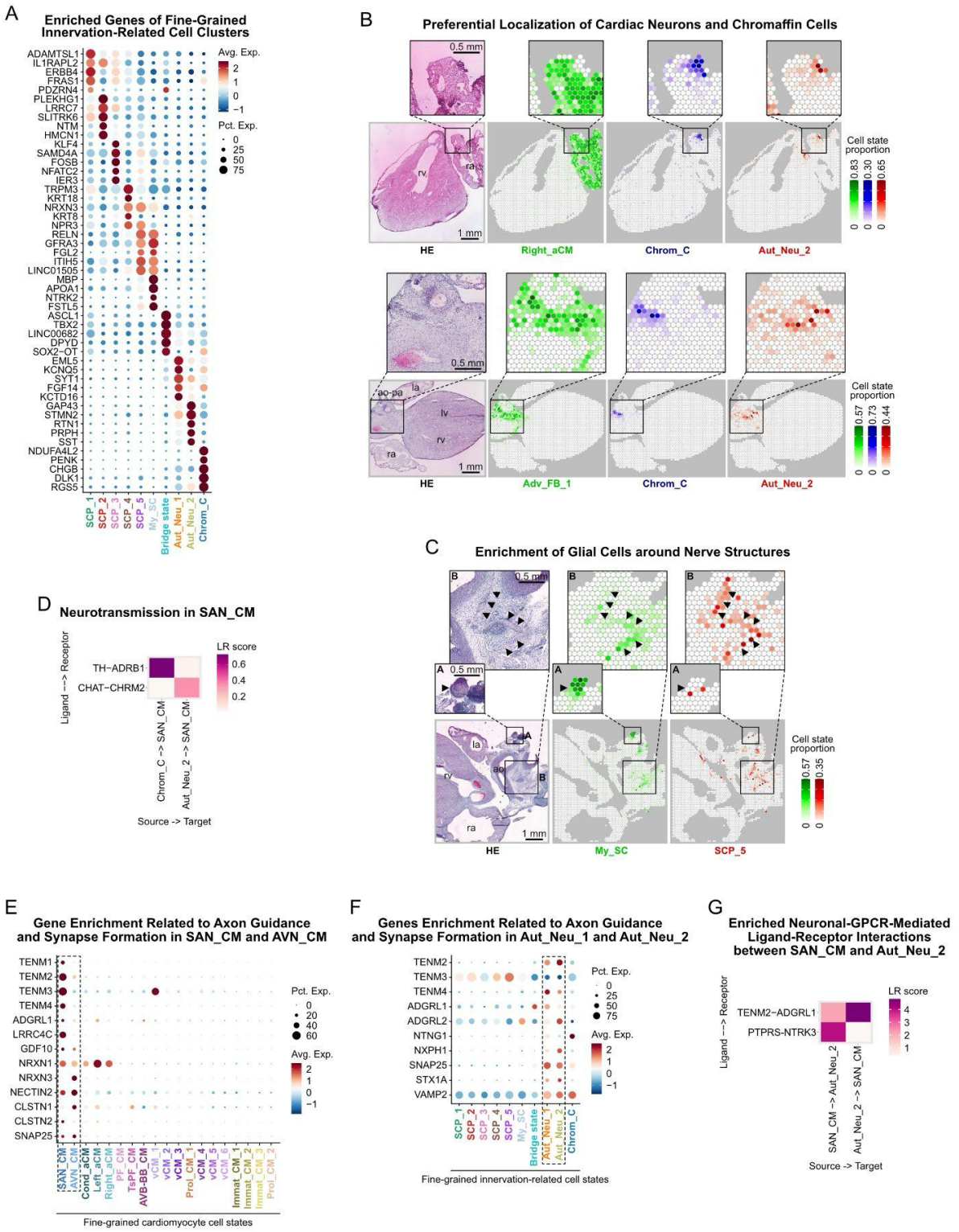




Supplemental Figure 4

**Suppl. Fig. 4. Transcriptomic and Spatial Characteristics of Fine-Grained Innervation-Related Cell States. A.** *Enriched Genes of Fine-Grained Innervation-Related Cell Clusters.* Dot plot depicts the top 5 DEGs (log2FC > 0, p_val < 0.05) between the 10 clusters. **B.** *Preferential Localization of Neurons and Chromaffin Cells.* Chrom_C (blue) and Aut_Neu_2 cells (red) are closely associated with the atrial wall (outlined by Right_aCMs, green) and adventitia of the great arteries (outlined by Adv_FB_1 cells, green), presented in a 10.5 pcw (upper) and a 11 pcw (lower) heart section, along with their hematoxylin-eosin (HE) micrographs. ROIs highlight areas enriched in innervation-related cell states. **C.** *Enrichment of Glial Cells around Nerve Structures.* My_SCs (green) and SCP_5 cells (red) spatially associate with nerves (arrowheads) in the adventitia of the great arteries, highlighted in ROI A and B in the HE micrograph of a 11 pcw heart section. **D.** *Gene Expression Related to Axon Guidance and Synapse Formation across Fine-Grained Cardiomyocyte States.* Dot plot displays selective enrichment of relevant genes in SAN_CM and AVN_CM state. **E.** *Gene Expression Related to Axon Guidance and Synapse Formation across Fine-Grained Innervation-Related Cell States.* Dot plot displays selective enrichment of relevant genes in Aut_Neu_1 and Aut_Neu_2 cells. **F.** *Enriched Neural/GPCR-Mediated Ligand-Receptor Interactions between SAN_CM and Aut_Neu_2.* In panel D-E: la–left atrium, lv–left ventricle, ra–right atrium, rv–right ventricle, ao–aorta, pa–pulmonary artery; scale bars represent 1 mm in the main, and 0.5 mm in the zoom-in panels.

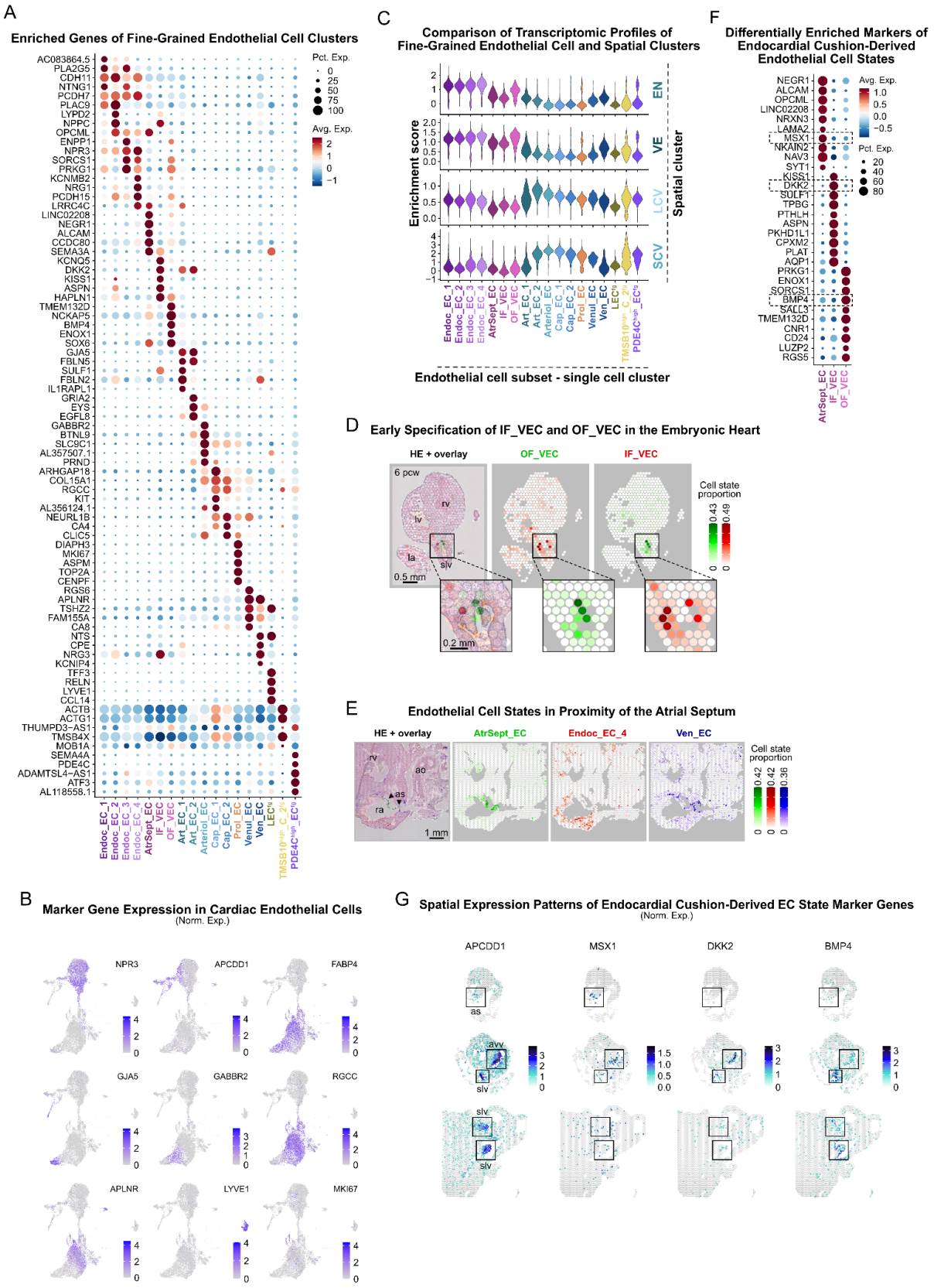


Supplemental Figure 5

**Suppl. Fig. 5. Molecular and Spatial Profiles of Fine-Grained Endothelial Cell States. A.** *Enriched Genes of Fine-Grained Endothelial Cell Clusters.* Dot plot depicts the top 5 DEGs (log2FC > 0, p_val < 0.05) between the 18 clusters. **B.** *Marker Gene Expression in Cardiac Endothelial Cells.* Feature plots of selected DEGs (log2FC > 0, p_val < 0.05) outline endothelial cell populations of the endocardium (*NPR3*), endocardium-derived endothelial structures (*APCDD1*), great arteries and coronary vasculature (*FABP4*, *GJA5*, *GABBR2*, *RGCC*, *APLNR*), and lymphatic vessels (*LYVE1*), as well as proliferating cells (*MKI67*). **C.** *Comparison of Transcriptomic Profiles of Fine-Grained Endothelial Cell and Spatial Clusters.* Violin plots show gene signature enrichment of selected spatial clusters in fine-grained endothelial cell states. Spatial clusters: EN–endocardium and subendocardium; VE–valve endothelium; LCV–large coronary vessels; SCV–small coronary vessels. **D.** *Early Specification of IF_VEC and OF_VEC Cell States in the Embryonic Heart*. Spatial mapping traces IN_VECs (red) and OF_VECs (green) to opposite sides of the developing semilunar valves, identified in the hematoxylin-eosin (HE) micrograph of a 6 pcw heart section. Scale bars represent 0.5 mm in the main, and 0.2 mm in the zoom-in panels. **E.** *Endothelial Cell States in Proximity of the Atrial Septum.* Endoc_EC_4 cells (red) show spatial enrichment in the smooth-walled atrium, while Ven_ECs (blue) map to areas of venous character in the direct vicinity of the atrial septum outlined by AtrSept_ECs (green), visualized in a 11 pcw heart section. Scale bar on the HE micrograph represents 1 mm. **F.** *Differentially Enriched Markers of Endocardial Cushion-Derived Endothelial Cell States.* Dot plot displays the top 10 DEGs (log2FC > 0, p_val < 0.05) between AtrSept_EC, IF_VEC and OF_VEC clusters. Genes highlighted by dashed rectangles were selected for spatial expression plots included in Suppl. Fig. 5g. **G.** *Spatial Expression Patterns of Endocardial Cushion-Derived Endothelial Cell State Marker Genes.* Spatial feature plots visualize the expression of selected AtrSept_EC (*MSX1*), IF_VEC (*DKK2*) and OF_VEC (*BMP4*) marker genes in the atrial septum, atrioventricular and semilunar valves (marked by rectangles) in 8 (top, middle) and 12 pcw (bottom) heart sections. In panels D, E, and G: slv–semilunar valve, avv–atrioventricular valve, as–atrial septum, rv–right ventricle, lv–left ventricle, ra–right atrium, la–left atrium, ao–aorta.

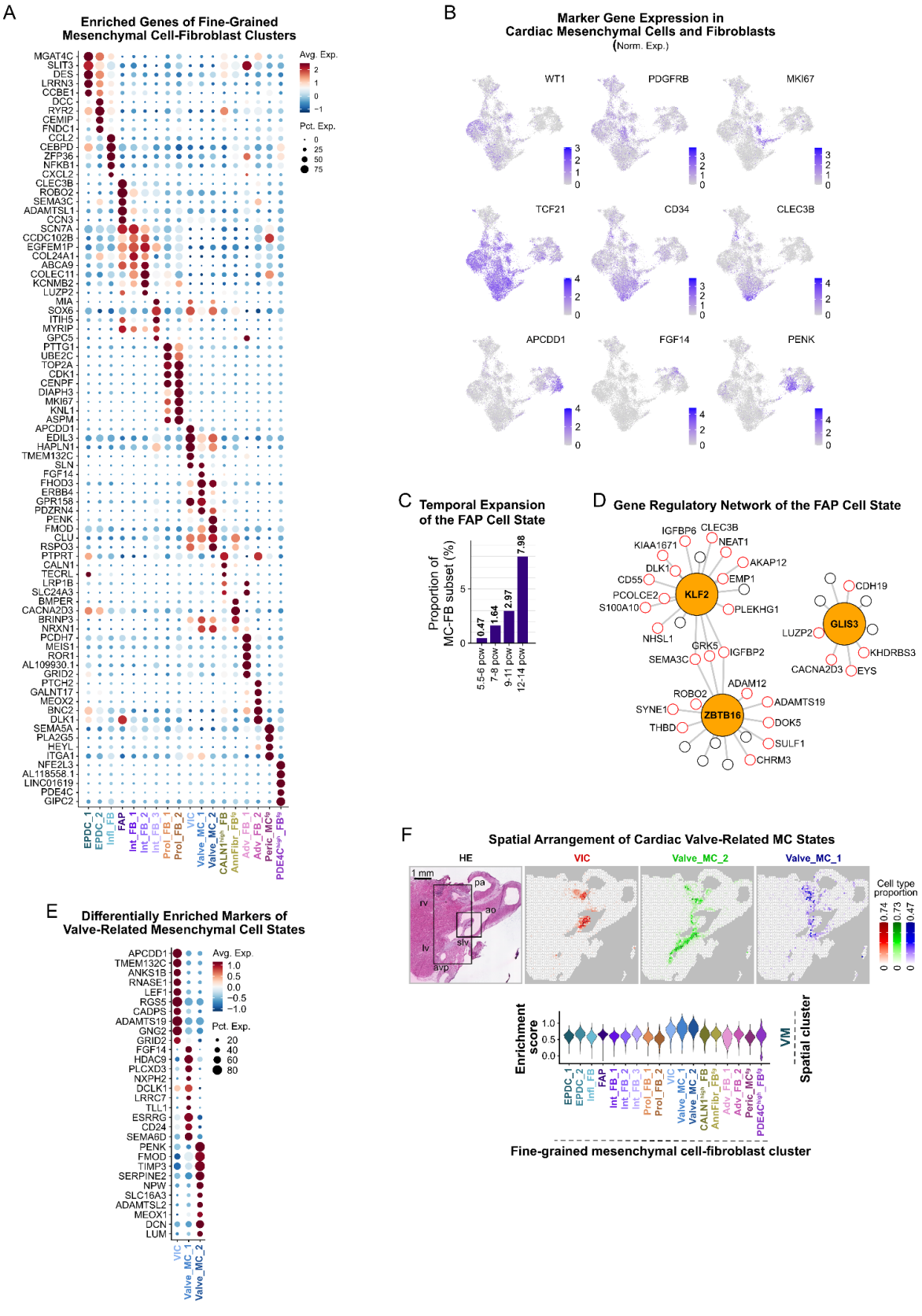


Supplemental Figure 6

**Suppl. Fig. 6. Transcriptomic and Spatial Features of Fine-Grained Fibroblast and Mesenchymal Cell States. A.** *Enriched Genes of Fine-Grained Fibroblast and Mesenchymal Cell States.* Dot plot depicts the top 5 DEGs (log2FC > 0, p_val < 0.05) between the 18 clusters. **B.** *Marker Gene Expression in Cardiac Mesenchymal Cells and Fibroblasts.* Feature plots of selected DEGs (log2FC > 0, p_val < 0.05) outline cell populations with high expression of consensus epicardial (*WT1*), pericyte (*PDGFRB*), fibro-adipogenic progenitor (*CLEC3B*), putative cardiac fibroblast (*TCF21*, *CD34*), and proliferation (*MKI67*) markers, and genes enriched in distinct cardiac valve-related mesenchymal cell states (*APCDD1*, *FGF14*, *PENK*). **C.** *Temporal Expansion of the FAP Cell State.* Bar plot illustrates changes of the proportion of FAPs in the mesenchymal cell-fibroblast subset across four developmental age groups (5.5-6 pcw, 7-8 pcw, 9-11 pcw, 12-14 pcw). **D.** *Gene Regulatory Network of the FAP Cell State.* Differentially expressed transcription factors, presented with their associated target genes, in the FAPs. Orange-filled circles represent transcription factors, and red-rimmed circles represent DEGs (log2FC > 0, p_val < 0.05) compared to other fine-grained mesenchymal cell-fibroblast clusters. **E.** *Differentially Enriched Markers of Valve-Related Mesenchymal Cell States.* Dot plot displays the top10 DEGs (log2FC > 0, p_val < 0.05) between VIC, Valve_MC_1 and Valve_MC_2 clusters. **F.** *Spatial Arrangement of Cardiac Valve-Related Mesenchymal Cell States.* VICs (red) show spatial enrichment in the free segments of the sampled semilunar valves, while Valve_MC_1 (blue) and Valve_MC_2 cells (green) localize to the roots of the cusps. Valve_MC_2 also spreads out to larger segments of the intervalvular fibrous tissue towards the atrioventricular valves, while Valve_MC_1 is enriched around the semilunar valves (marked by rectangles) (upper). Scale bar on the hematoxylin-eosin (HE) micrograph represents 1 mm. Rv–right ventricle, lv–left ventricle, ao–aorta, pa–pulmonary artery, slv–semilunar valve, avp–atrioventricular plane. Violin plot shows enrichment of the valve mesenchyme (VM) spatial cluster gene signature in all three fine-grained mesenchymal cell clusters related to the cardiac valves (lower).

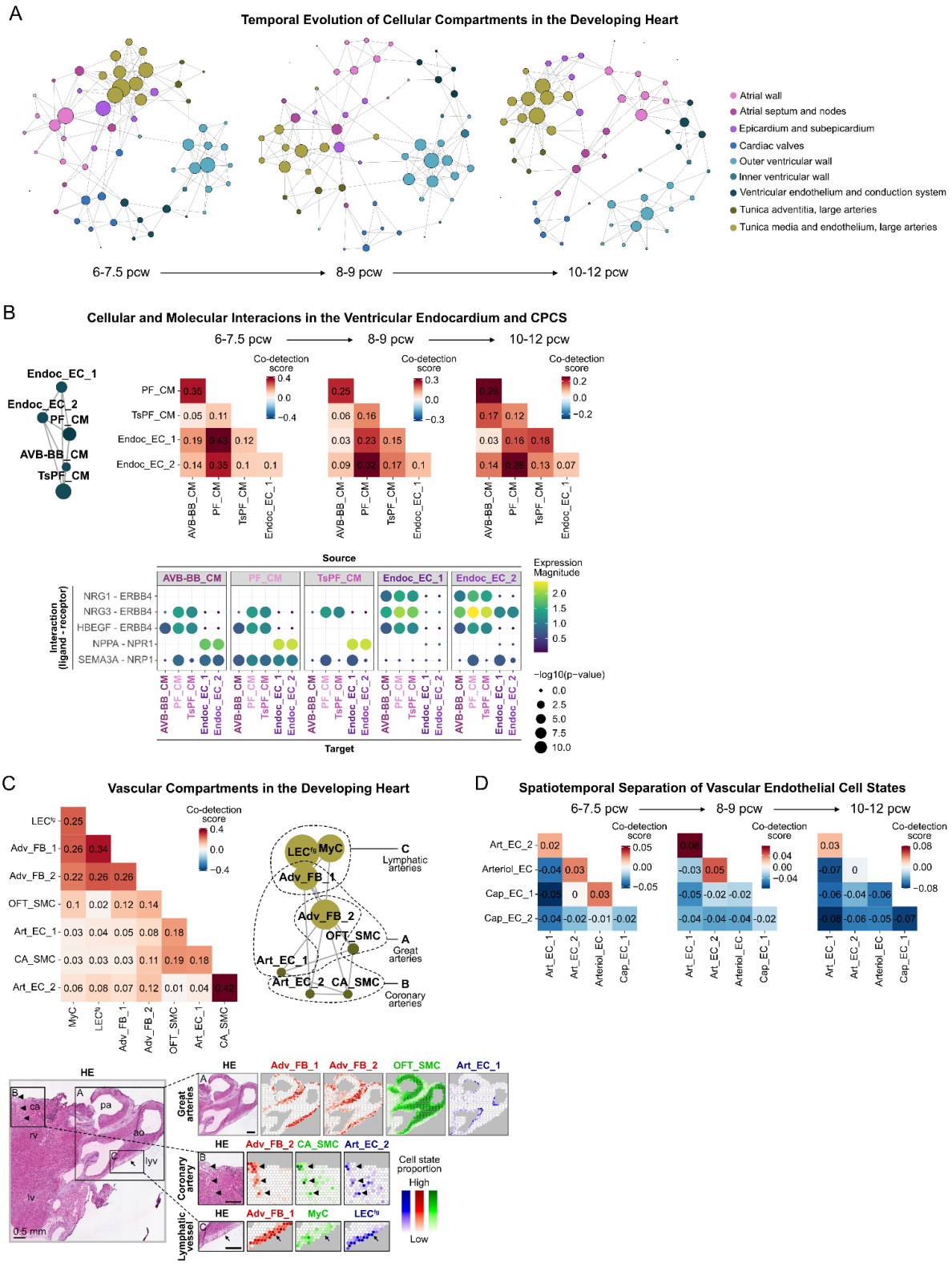




Supplemental Figure 7

**Suppl. Fig. 7. Temporal Transitions and Analysis of Selected Developmental Cardiac Niches. A.** *Temporal Evolution of Cellular Compartments in the Developing Heart.* Niche network graphs calculated from cell state co-detection scores are displayed across three developmental age groups (6-7.5, 8-9, 10-12 pcw). Circles represent fine-grained cell states, and grey lines indicate their spatial association. Circle size reflects the number of closely associated cell states, and different colors indicate distinct cardiac structural compartments, consistently with Fig. 7A. **B.** *Cellular and Molecular Interactions in the Ventricular Endocardium and CPCS.* Niche network graph represents cellular components of the ventricular endocardium and conduction system (CPCS) (upper left), along with corresponding co-detection scores across three developmental age groups (6-7.5, 8-9, 10-12 pcw) (upper right). Selected ligand-receptor interactions, implicated in trabecular myocardium formation and Purkinje fiber specification, indicate functional differences between EndocEC_1 and Endoc_EC_2, and PF_CM and TsPF_CM, respectively (lower). **C.** *Vascular Compartments in the Developing Heart.* Niche network graph illustrates relations between cellular components of distinct cardiac vessel structures, outlined by dashed lines (upper right), with corresponding co-detection scores (upper left). Spatial mapping displays enrichment of Adv_FB_1 (red), Adv_FB_2 (red), OFT_SMC (green) and Art_EC_1 cells (blue) in the great arteries (ROI A), Adv_FB_2 (red), CA_SMC (green) and Art_EC_2 cells (blue) in coronary vessels (ROI B, marked by arrowheads), and Adv_FB_1 (red), MyC (green) and $LEG^{fg}$ cells (blue) around lymphatic vessels (ROI C, marked by arrows). Scale bars represent 0.5 mm in both the main and zoom-in panels of hematoxylin-eosin (HE) micrographs. Rv–right ventricule, lv–left ventricule, ao–aorta, pa–pulmonary artery, ca–coronary artery, lyv–lymphatic vessel. **D.** *Spatiotemporal Separation of Vascular Endothelial Cell States.* Temporal changes of co-detection scores between vascular endothelial cell states are presented across three developmental age groups (6-7.5, 8-9, 10-12 pcw).